UNIVERSITY OF LEEDS

# The Radio Emission from Young Massive Stars

**Solomon Kwaku Appekey**

School of Physics and Astronomy

University of Leeds

Submitted in accordance with

the requirements for the degree of

*Master of Science by Research*

**January 2023**

# Intellectual Property

The candidate confirms that the work submitted is his own and that appropriate credit has been given where reference has been made to the work of others.

This copy has been supplied on the understanding that it is copyright material and that no quotation from the thesis may be published without proper acknowledgement.



Signed 

# Acknowledgements

I would like to express profound gratitude to my supervisor, Dr. Stuart Lumsden, for his exceptional support and guidance during this work. A special thank you to Professor Melvin Hoare for facilitating the completion of this project. Also, thank you to Dr. Catherine Walsh and Prof. Derek Ward-Thompson for all the comments, suggestions and corrections to my thesis.

A huge thanks to the Development in Africa through Radio Astronomy (D.A.R.A) Project - Newton fund, for sponsoring this masters.

A big thank you to my friend, Callum Brennan-Rich for the help with my plots. Also, to Mubela for helping with my imaging. Additionally, I am grateful to my colleagues and friends Bilal, Kingsley, Isaac, Yara and Madinah for their suggestions throughout this work.

I am thankful to my entire family, especially my mother for her endless prayers, encouragement and support.

Finally, I am happy to have had a father who gave me the freedom to dream and do what I love. This is for you dad! I wish you saw this adventure.

# Abstract

Studying young massive stars or young stellar objects (YSOs) at radio wavelengths together with complementary millimetre wavelength data is very important for understanding the complete process of the formation and evolution (especially the mechanism behind the production of jets and outflows) of these objects. In this study, we investigate a sample of 20 YSOs which form the IRAM Northern Extended Millimeter Array (NOEMA) CORE large program sample. These targets are luminous ($L > 10^4 L_\odot$), close by ($d < 6$ kpc) and well-studied young massive stars in the northern hemisphere.

We have studied 8 of these targets that did not have any previous Karl G. Jansky Very Large Array (JVLA) data prior to this work. This study was performed in JVLA's A-configuration at 6 GHz and at a resolution of 0.33 arcseconds. For our targets, we detected radio continuum emission from 7 of these objects including the detection of 2 jets. Additionally, we found evidence of variability among 2 of our targets.

For the entire sample, we performed a comprehensive radio and millimetre study where we found and associated observed millimetre cores with radio detections (including jets, jet lobes and HII regions) using results from this work and literature.

One of the goals of this study is to investigate the orientation of jets to their respective millimetre emission and or discs (if present). We found evidence of a perpendicular orientation of the detected jet to the millimetre emission for the target NGC 7538S. Also, 2 of our targets show a perpendicular disc-jet orientation (using information from literature). Our sample also show divergence from low-mass stars and HII regions in radio luminosity and bolometric luminosity parameter space which indicates that young massive stars are likely to be formed through a scaled up version of their low-mass counterparts. We also find a strong correlation between sample and core masses which may suggest that larger global or sample masses tend to lead to

larger core masses.

# Contents

# List of Figures

# List of Tables

# Abbreviations

- **2MASS** Two Micron All-Sky Survey
- **AU** Astronomical unit
- **CASA** Common Astronomy Software Application
- **CORNISH** Co-Ordinated Radio 'N' Infrared Survey
- **DEC** Declination
- **EM** Electromagnetic Spectrum
- **HMC** Hot Molecular Core
- **HST** Hubble Space Telescope
- **IMF** Initial Mass Function
- **IR** Infrared
- **IRAM** Institut de Radioastronomie Millimetrique
- **IRDC** Infrared Dark Clouds
- **JVLA** Karl G. Jansky Very Large Array
- **LMC** Large Magellanic Cloud
- **LTE** Local Thermodynamic Equilibrium
- **MC** Magneto-centrifugal
- **MDC** Massive dense cores
- **MHD** Magneto-hydrodynamic

- **NOEMA** IRAM Northern Extended Millimeter Array
- **NRAO** National Radio Astronomy Observatory
- **NVSS** NRAO VLA Sky Survey
- **PA** Position Angle
- **RA** Right Ascension
- **RMS** Red MSX Source
- **SCUBA** Submillimetre Common-User Bolometer Array
- **SED** Spectral Energy Distribution
- **SMBH** Supermassive Black Holes
- **SNR** Signal-to-Noise Ratio
- **SPW** Spectral window
- **UCHII** Ultra-Compact HII region
- **UKIDSS** UKIRT Infrared Deep Sky Survey
- **UV** Ultra-Violet
- **VLA** Very Large Array
- **VLT** Very Large Telescope
- **YSO** Young Stellar Object
- **e-MERLIN** enhanced Multi-Element Remote-Linked Interferometer Network
- **rms** root-mean-square

# Chapter 1

# Introduction

## 1.1 Massive star formation

There is not a complete picture of massive star formation thus in terms of both the theoretical and observational treatment. There are several reasons for this: early stage massive stars (young massive stars or high-mass protostars) are difficult to study in detail due to corresponding large distances (more than 800 parsecs), congestion and effects of their environment (McKee and Ostriker 2007a and Ridge and Moore 2001). Also, to compare massive stars to their low-mass stars counterparts, massive or high-mass stars form less often (Cohen and Kuhi 1979, Wilking 1989, Andre et al. 2000, Walter et al. 2000, Kurtz et al. 2000, Stahler et al. 2000, Kroupa 2002, Beuther et al. 2007a and Girart et al. 2009) hence the difficulty in understanding their formation. From a theoretical standpoint, the key difference between low-mass and high-mass star formation is that low-mass stars form in a time $t_{*f}$ that is short compared to the Kelvin-Helmholtz time scale that is $t_{KH} \leq t_{*f}$ (Kahn 1974). Hence low-mass stars undergo substantial pre-main-sequence evolution after accretion has ended, while high-mass stars can accrete a large amount of mass while on the main sequence (Beuther et al. 2007a). In general, the prevalent view remains that massive star formation is a scaled-up version of low-mass star formation (Beuther et al. 2007a) with high accretion rates which has been supported by several observational and computational studies such as Wolfire and Cassinelli (1987), Osorio et al. (1999), McKee and Tan (2002), Yorke and Sonnhalter (2002) and McKee and Tan (2003).

The process of massive star formation directly affects the evolution of structures in the universe, especially galaxies (Kennicutt et al. 1994, Sridharan et al. 2002 and Zinnecker and Yorke 2007).

In general, massive stars release huge amounts of energy, including ultra-violet (UV) radiation in the form of HII regions as well as winds, outflows (including massive molecular outflows, Shepherd and Churchwell 1996, Richer et al. 2000, Beuther et al. 2002, Shepherd 2005 and Arce et al. 2007), jets, supernovae explosions and shocks into their environment (Sridharan et al. 2002). In terms of disks and jets, Johnston et al. (2015), Ilee et al. (2016), Lee et al. (2017), Moscadelli et al. (2019) and others have shown through observations that most early stage massive stars (masses of at least 20 solar masses) host these disks (rotating) and jets.

Massive stars are formed in clusters (Lada 1987, Lada and Lada 2003 and McKee and Ostriker 2007a, Figure 1.1 shows such a stellar cluster: a very dense young high mass stellar cluster taken with the Hubble Space Telescope) and are usually dense with sizes of about 1 parsec and a mass range of between hundreds to thousands of solar masses and also characterized by densities between $10^4$ to $10^5$ cm$^{-3}$ (Lada 1987 and Lada and Lada 2003). Massive stars form on relatively short timescales of about $10^5$ years (McKee and Ostriker 2007a). Egan et al. (1998) have suggested that the earliest stages of massive star formation may occur in the infrared dark clouds (IRDCs) (Egan et al. 1998, Bacmann et al. 2000 and Carey et al. 2000). Also, Van der Tak (2004) has hinted to the fact that early-stage massive stars are sometimes linked with hot molecular cores (HMCs). These HMCs are huge masses of dense and warm gases with high abundances of diverse organic molecules (Osorio et al. 1999 and Zinnecker and Yorke 2007) and are indicated by methanol maser emission (Walsh et al. 1999 and Minier et al. 2005) with a diverse chemistry. Most massive stars may be associated with HII, ultracompact HII and even the so called hypercompact HII regions. The ultracompact HII regions are usually associated with the final stage of these massive stars (McKee and Ostriker 2007b). Figure 1.2 shows the evolutionary sequence of the formation of massive stars (showing the molecular cloud complex, massive dense core (MDC), protostellar MDC, high-mass protostellar and the IR-bright high-mass protostar phases by Motte et al. 2018). Figure 1.2 also highlights the key points mentioned above including the categorization of high-mass protostars into IR-quiet and -bright phases. Equation 1.1 below defines the dividing line between IR-bright and IR-quiet objects. In Equation 1.1, $S_{21\mu m}$ is flux at 21 μm, D is the distance measured in kpc units and L is the bolometric luminosity in $L_\odot$ units.

$$S_{21\mu m} < 10Jy \left(\frac{1.7kpc}{D}\right)^2 \left(\frac{L}{1000L_\odot}\right) \tag{1.1}$$


Figure 1.1 | **Dense high-mass stellar cluster.** An infra-red and optical image of a very dense young high-mass stellar cluster by the Hubble Space Telescope. Brandl et al. (1999) shows tens of O type high-mass stars packed within a 2 parsecs radius. (a) Is a Very Large Telescope image of NGC 3603 and (b) is also a Very Large Telescope image of the Trapezium Cluster in the constellation of Orion (McCaughrean 2001). Both images show how these two huge clusters in the galaxy would appear at a distance of R136 (The background image: within the Large Magellanic Cloud (50 kpc)). Image is taken from McCaughrean (2001).

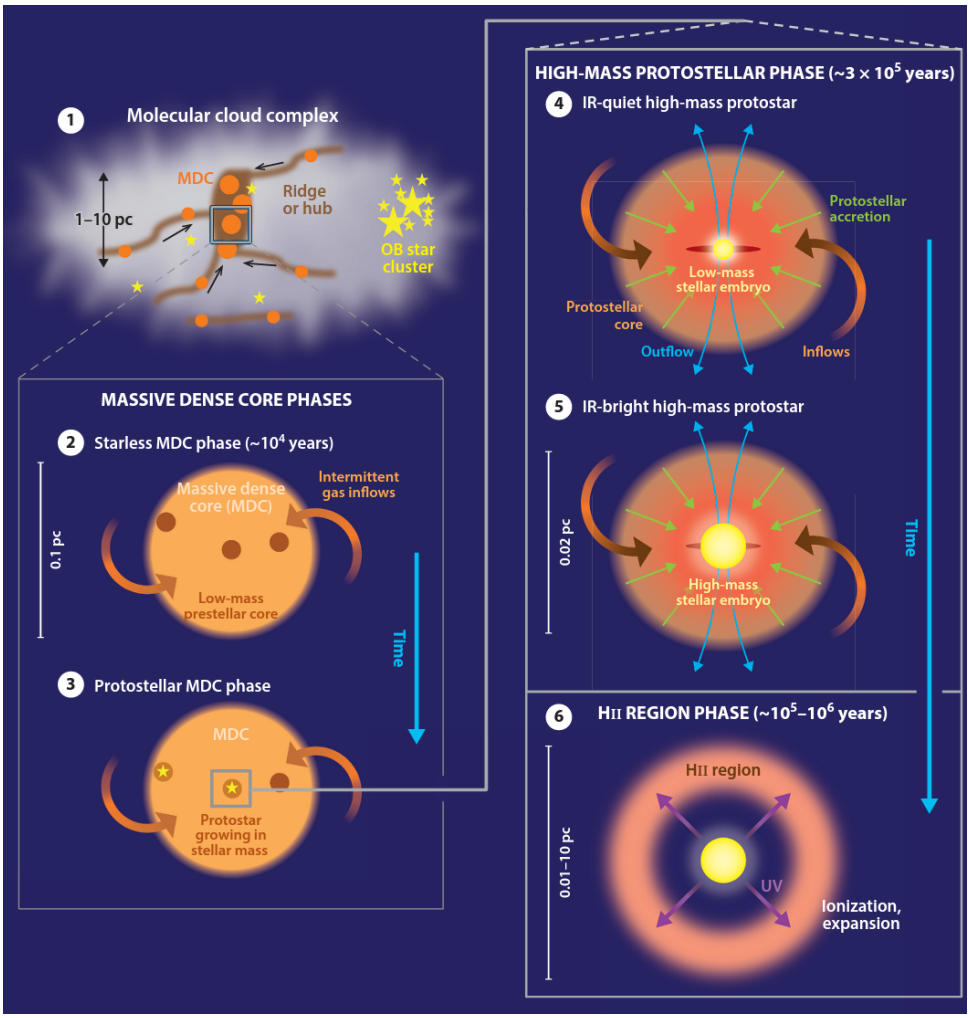


Figure 1.2 | **Evolutionary sequence of massive star formation.** A schematic showing the evolutionary sequence of the formation of massive stars by Motte et al. (2018). Panel: (1) illustrates the molecular cloud complex composed of huge filaments and circular clumps referred as 'ridges and hubs', also hosting massive dense cores (MDC). (2) shows the massive dense core phases. Here, the starless phase is evident with the MDCs bearing only the low-mass prestellar cores. (3) the protostellar MDC phase. IR-quiet (defined by Equation 1.1) MDCs turn into protostellar, with an associated low-mass stellar nucleus. (4) High-mass protostellar phase. The protostellar wrapping feed from incursions driven gravitationally, preceding the formation of high-mass protostars. The high-mass protostar, will be IR-quiet as long as their associated nucleus remain low-mass (5) IR-bright high-mass protostar. The high-mass protostars become IR-bright for stellar nucleus with large masses ($> 8 M\odot$). (6) HII region phase. The key accretion phase ceases once the stellar ultraviolet region ionizes the protostellar wrapping or cover and an HII region forms.

The focal point of this research is the detection of the radio emission (either thermal or non-thermal, though it is important to note that we do not discuss this in great detail. See Obonyo 2020 and Purser et al. 2021 for more details on this topic) from massive stars which harbour outflows and or jets. We also investigate whether jet radio luminosity scales with bolometric luminosity: if true, will indicate that jets associated with massive stars may be produced through

'scaled-up' processes of their low-mass counterparts (Purser et al. 2016 and Purser et al. 2021). Radio data on massive stars is crucial to understanding the embedded phases of these stars as it reveals the cores of these stars and their dynamic outflows and jets which are still not completely understood. It is known that the production of outflows and jets is a key aspect of star formation (Beuther et al. 2002). In general these outflows provide a historical record of the mass loss rates and hence the mass-accretion record of these forming stars. Also, outflows symmetries provide insight into the variations in the stellar environment for instance a Z-shaped outflow symmetry shows evidence of precession thus the outflow axis has changed over a period of time. Additionally, outflows affect the their parent clouds, determine the initial mass function and the final stellar mass (Bally et al. 2007).

In this chapter, we discuss the basic concepts of radio astronomy, thus the production of radio emission (and the various types). We also discuss briefly, the formation of stars that is, both low and high-mass stars (highlighting the theoretical treatment of the formation of stars), star forming regions, characteristics of young massive stars and why it is important to study them. Furthermore, we explore some of the current competing theories of massive star formation and end the chapter with an introduction to the focus of this study: radio emission from young massive stars, a description of the CORE program and provide some background information on the observation of our target fields including a review of the targets with published data prior to this work.

## 1.2 Why do we study massive stars?

Massive stars are the main source of heavy elements in the universe (Zinnecker and Yorke 2007). These heavy elements form the basic building blocks of life in the universe. Examples of these heavy elements are carbon, oxygen and nitrogen. They are formed when massive stars are at the end of their lifetimes and begin to fuse elements rather than hydrogen or helium (Cowan and Sneden 2006). Also, we study these stars because they are very dynamic and affect the structure, morphology, and evolution of galaxies at a vast range of scales (through the emission from their outflows, jets, shocks, explosions and reionization of the universe). The high luminosities of massive stars contribute to the regulation of the interstellar medium and the formation of star clusters and stars (also planets found around these stars in such environments) (Tan et al. 2014). In terms of massive stars influencing the formation of planets and their environments, Lozovsky

et al. (2021) have suggested that massive stars tend to host larger and more massive planets. Another reason why massive stars are important to our understanding of star formation and building a complete stellar model is that, they evolve very quickly (approximately millions of years) and hence we are unable to study their complete nature in great detail (Kennicutt 1998).

## 1.3 Radio astronomy and radio emission

The radio window is broad and hence almost all types of astronomical sources, thermal and non-thermal radiation mechanisms, and propagation phenomena can be observed at radio wavelengths. With this, radio astronomy has enabled us to make a lot of discoveries about our universe, some of which include non-thermal radiation from our Galaxy and many other astronomical sources, the 'violent universe' of powerful radio galaxies and quasars (quasi-stellar radio sources) driven by supermassive black holes (SMBHs), thermal spectral-line emission from interstellar gas (cold) atoms, molecules and ions, cosmic microwave background radiation from the hot big bang, coherent continuum emission from pulsars and stars among others.

### 1.3.1 What are radio emission and how are they produced?

Radio waves occupy the low-energy or long-wavelength end of the electromagnetic spectrum, spanning from frequencies between 60 GHz to 10 kHz. Some radio waves emerge from charged particles - often electrons characterized by high energies. In astronomy, all stars that are hot emit radio radiation due to thermal free-free emission by the ionized material in their stellar environment (specifically, wind). Some of these may also reveal non-thermal radio emission that often subjugate the thermal constituent. The non-thermal emission is believed to be caused by electrons that are 'Fermi-accelerated around shocks' (Bell 1978), thus when these electrons travel at relativistic speeds and spiral around in a magnetic field, they emit synchrotron radiation, which is detected as non-thermal radio emission (Bieging et al. 1989). This type of radio emission (synchrontron radiation) is also responsible for the enhanced radio emission from other objects found in space, for example quasars. With synchrotron radiation, we can induce radiation which stretches into and above X-ray (usually related to short-wavelength, high-frequency phenomena, which makes it possible to study some of the very energetic processes and objects in the universe).

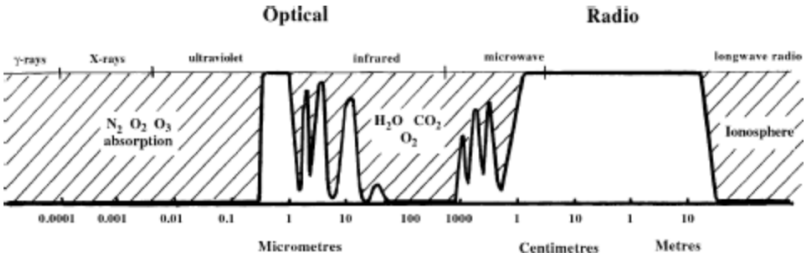


Figure 1.3 | **The electromagnetic spectrum.** Illustrated here is the EM spectrum, showing the wavelength ranges or 'windows'. The radio range is restricted by the earth's ionsphere at wavelengths > about 1-3 meters. Atmospheric absorption becomes important at sub-millimetre range (Burke and Graham-Smith 2009).

## 1.4 Thermal and non-thermal emission, how are they formed?

From Larmor's formula (see Equation 1.2 below), we know that the electromagnetic radiation with power (P) is generated by accelerating or decelerating (bremsstrahlung radiation) an electrical charge (q). Free particles (charged particles) can be accelerated by magnetic or electrostatic forces (with acceleration due to gravitational forces negligible compared to magnetic or electrostatic forces). Simply put, Larmor's equation says that any charged particle gives off radiation when accelerated (the overall radiated power is proportional to the square of the acceleration). In astronomy, this is useful in arriving at an expression for the radiation for free–free (thermal) and synchrotron (non-thermal) emission.

$$\mathrm{P} = \frac{2\mathrm{q}^2\dot{\mathrm{v}}^2}{3\mathrm{c}^3} \tag{1.2}$$

Where q is the charge, $\dot{\mathrm{v}}$ is the acceleration vector and c is the speed of light.

Thermal emission are formed by a source with particles emitting in local thermodynamic equilibrium (LTE) with the particles or radiating electrons being characterised by a Maxwellian velocity distribution. For astronomical sources (for example jets and outflows from massive stars) related with non-thermal emission, electrons travel at relativistic speeds and spiral around in magnetic fields and hence produce a magneto-bremsstrahlung radiation usually called synchrotron emission.

Emission in the form of thermal or non-thermal continuum emission occurs during almost all phases of massive star evolution (Blomme 2011). Detecting and understanding them are key

to unlocking the mysteries of the process of massive star formation since they pierce through the dusty shells of protostars hence revealing information about kinematics among others. For example, radio emission indicate the position of protostars and show the active regions of massive star formation. Also, protostellar jets in both low and high-mass stars can radiate non-thermal radio emission (Velusamy et al. 2007, Carrasco-González et al. 2013 and Obonyo 2020) indicative of the presence of relativistic charged particles and magnetic fields which is key in building accurate star formation models.

## 1.5 How do stars form?

One of the complex processes in the universe is the formation of stars. From the collapse of a molecular cloud core (that is, for a cloud supported by pressure (magnetic and thermal), there will be a collapse if its mass exceeds a critical mass) to the beginning of a thermonuclear fusion at the core. In general, star formation can begin with a critical mass range of $M \geq 0.08$ to $M \approx 315 \pm 50 M_{\odot}$ (Hayashi and Nakano 1963 and Crowther et al. 2016), this gives rise to a diverse range of masses. In the analysis of the formation of stars, a crucial question arises, what causes the observed diverse range of stellar masses? To answer this Shu et al. (1987), have suggested that the range in mass can be due to fragmentation of clumps into cores of different masses (this has been shown in studies such as Palau et al. 2013 and Beuther et al. 2018), or due to the halting of the process of mass accumulation by the core (of a protostellar object). Another critical parameter that is often discussed during star formation and stellar masses is the initial mass function (IMF). IMF is the distribution of stellar masses. At large scales, the IMF directs and decides the evolution and outcome of galaxies and star clusters (Kroupa 2002).

## 1.6 Jeans mass

To summarize the theoretical treatment for the formation of stars, we start off with a cloud at hydrostatic equilibrium (a cloud that is supported internally by thermal pressure). This leads up naturally to the Virial equation (thus assuming virial equilibrium). With the cloud at Virial equilibrium, we can come up with a set of criteria for the collapse of molecular clouds. These collapse criterion, enable us to derive the Jeans' mass (which describes the critical mass above which we expect clouds to become gravitationally unstable and hence form stars). The Jeans'

mass ($M_J$) (Larson 1981) is described by Equation 1.3 below:

$$M_J \approx 10^5 \frac{T^{\frac{3}{2}}}{\mu^2 n^{\frac{1}{2}}} M_\odot \tag{1.3}$$

Where T is the temperature of a dense core measured in Kelvin (K), n is the number density in $m^{-3}$ units, $\mu$ is a constant (related to the mean mass density of the core) and $M_\odot$ is mass of the Sun.

Figure 1.4 | **The Orion molecular cloud.** An image of the Orion molecular cloud, found in the northern part of the sky (Muench et al. 2008). Image by Robert Gendler.

## 1.7 Where to locate star forming regions

Theoretically, it is clear that stars form inside of dense cores in huge but lower density structures (Ridge et al. 2006) which comprise of molecular clouds. These molecular clouds are made up of dust and gases and are mostly very dense with masses between $10^5$ to $3 \times 10^6 M_\odot$ (Solomon et al. 1979). Particularly, molecular clouds which lead to the formation of stars are huge with diameters of between 1 to 10 parsecs. An example of such molecular clouds are shown in Figures 1.4 and 1.5. Some of these star forming regions may be associated with more evolved HII regions (protostellar regions which are formed by the ionization of hydrogen atoms by high energy photons) and lead to further star forming processes as seen in the Orion molecular cloud even today (Ridge et al. 2006).

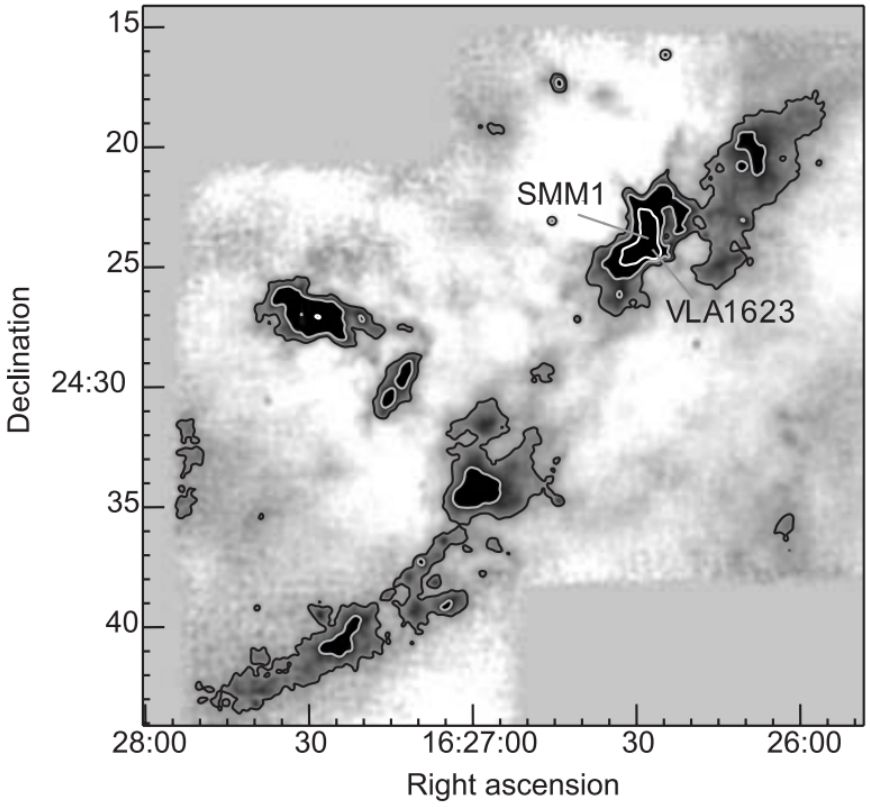


Figure 1.5 | **The Oph molecular cloud.** An image of the Oph molecular cloud region by SCUBA, showing the prestellar (labelled as SMM1 in image) and protostellar (as VLA1623 in image) phases and the formation of clusters at the core of Oph. (Andre et al. 1993, Johnstone et al. 2000 and Ward-Thompson et al. 2006).

## 1.8 How do low and high-mass stars form?

### 1.8.1 Low-mass star formation

Low-mass stars have a mass range of about 0.01 to 3 $M_{\odot}$ (Shu et al. 1987 and Klein et al. 2007). Low-mass stars have an evolution timescale of billions of years (100 Myr for low-mass protostars) and have relatively low luminosities (Burrows et al. 1997, Stahler and Palla 2004 and Luhman 2012). Low-mass stars have been studied in detail, for example by Lada (1987), Kroupa et al. (1993) and Luhman (2012). The formation of low-mass stars occurs in distinct stages, firstly the collapse of a molecular cloud (usually, this collapse is also accompanied by the formation of a disk around this protostar). This collapsing cloud turns into a core, with an interior and an outer structure. In the end, the newly built dust cloud is cleared by the process of outflows and radiation pressure from this new star (protostar). The outflow may be driven into the protostar's environment and the interstellar medium. After several million years or so, a protostar and a left-over disk (residual circumstellar disk) is formed. There are several models that describe the formation of low-mass stars in greater detail, an example is Larson's model (Larson 1969) which describes the formation of a low-mass star by the collapse of an optically thin cloud (spherical) via an isothermal process. Shu et al. (1987) describes the formation of low-mass star from a slowly rotating cloud of gas which is almost isothermal (neglecting the effects of magnetic fields). As the gas evolves with these conditions, it produces a density distribution given that gravitational and thermal pressure are approximately equal. This leads to the formation of a core at the heart of this molecular cloud. In the end, there is an 'inside-out collapse' (Figure 1.6 shows the formation of a star from a molecular cloud as described by Shu et al. 1987) thus, the interior regions of the cloud collapses first, then followed by the outer region of the cloud. Currently, models such as the one by Tomisaka (2002) describes a model of the formation of low-mass stars which considers the effect of magnetic fields and rotation for a cloud under collapse. Tomisaka (2002)'s model, reproduces a dense central core with an accretion disk and outflows.

At the moment, there are two mainstream models that explain what determines the mass of stars. The first is the theory of direct gravitational collapse. This theory suggests that star forming turbulent clouds fragment into cores that will eventually collapse to form single stars or small multiple systems (Shu et al. 1987, Padoan and Nordlund 2002 and Padoan and Nordlund 2004). The other is the competitive accretion theory. This propose that at birth all stars have a

mass smaller than the classical stellar mass and that the ultimate stellar mass is decided by the eventual accretion of unconfined gas from its associated gas clump (Bonnell et al. 1998, Bonnell et al. 2001 and Bate and Bonnell 2005).

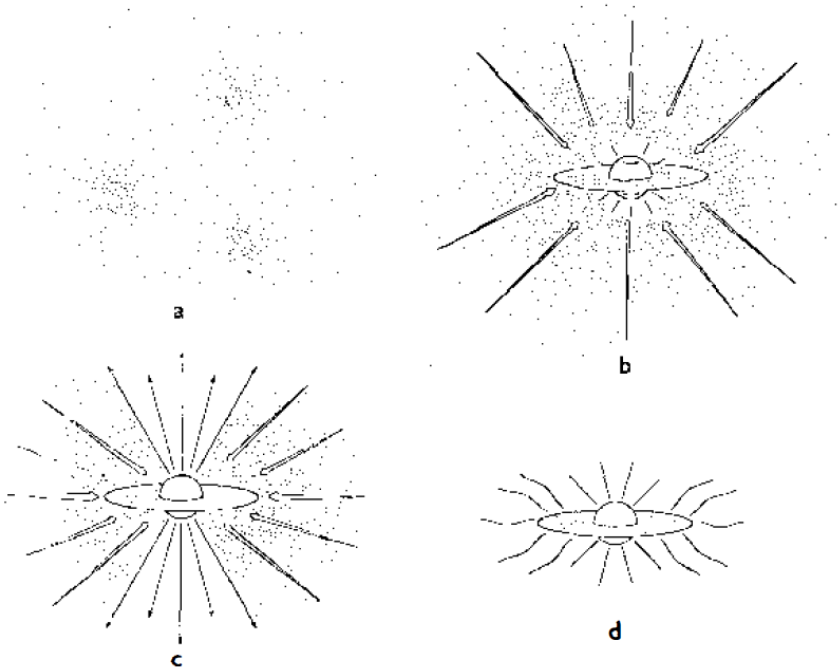


Figure 1.6 | **Star formation process.** A four stage star formation process: (a) Cores are evident here within molecular clouds (b) A disk forms around the cloud core with an 'inside-out' collapse (c) Here, we see a bipolar outflow with an associated stellar wind (d) Infall of material ceases, showing a new star with a disk (Shu et al. 1987).

### 1.8.2 High-mass star formation

As seen in Cepheus and Orion through millimetre observations, massive stars (stars with masses greater than $10M_{\odot}$) are related to warm clouds (ranging $30-50$K) and linked with huge (densities between $10^5-10^6 cm^{-3}$) fragmented molecular clouds (Stahler and Palla 2004, Fontani et al. 2002 and Ahmadi et al. 2018). Also, massive stars have high luminosities (greater than $10^4L_{\odot}$) (Sridharan et al. 2002). They form from clumps with masses of about $10^2-10^4M_{\odot}$ at large parsec scales (Fontani et al. 2002) with $H_2$ column densities between $10^{23}$ and $10^{24}cm^{-2}$ (Zinnecker and Yorke 2007). These molecular clouds collapse and fragment, resulting into cores with high densities. Some studies indicate that massive stars form very often in clusters, for example in the core of Pleiades (Lada and Lada 2003 and Stahler and Palla 2004). Low-mass stars may be similar to high-mass stars in terms of their initial phase, however there are no confirmed relationships between the two with respect to how they evolve. Massive stars usually form in environments rich with molecular clouds compared with their low-mass counterparts.

Proceeding from their initial stage, high-mass stars build up energy from the process of accretion (Krumholz and McKee 2008). This energy is released into the protostar's environment through jets, accretion disks and outflows (Keto and Wood 2006), which leads up to the formation of an HII region and the ionization of the interstellar medium. Figure 1.2 shows an evolutionary sequence of the formation of high-mass stars (Motte et al. 2018).

Young massive stars are usually obscured in their environments making them difficult to study in detail. Fortunately, though obscured at this stage, they are able to emit at IR wavelengths (mid-infrared) hence they can be observed and studied. They are believed to grow rapidly and hence have short evolutionary phases of about $10^5$ years and usually influence (via the release of radiation through outflows, disc-winds and jets) their environment soon after the formation of their stellar cores (Garay and Lizano 1999).

Figure 1.7 | **AFGL 2591 outflow.** This image is a composite image of AFGL 2591 showing a huge outflow in the near-infrared (taken by the Gemini North telescope). A collimated flow, including a long narrow-like structure originating from the west of this young massive star (with a mass of 20 $M_\odot$). To the east, there is no similar structure visible. Only a faint visible shock can be seen, though almost completely hidden (Trinidad et al. 2003 suggest this is due to a very dense circumstellar disk) (Zinnecker and Yorke 2007). AFGL 2591 is one of the targets of this study.

### 1.8.3 Young massive stars, outflows and jets

Just as in their low-mass counter-parts, disks were believed to play an important role in young massive stars with several studies such as Hamann and Persson (1989), Chandler et al. (1993), Kraus et al. (2010) and Johnston et al. (2015) detecting them. Young massive stars are also associated with outflows (an example of this outflow is shown in Figure 1.7) and jets (Zhang et al. 2001, Frank et al. 2014, Eisner et al. 2015, Moscadelli et al. 2016, Obonyo 2020 and Purser et al. 2021). Also, they are associated with accretion processes as studied by Caratti o Garatti et al. (2017). Most now believe that these observed outflows, disks and jets are very important in the process of accretion (Purser et al. 2016 and Ahmadi et al. 2018) in young massive stars.

In the past, some young massive stars have been studied into detail. Some popular examples are G31.41 +0.31mm (Cesaroni et al. 1994) and IRAS 23385+6053 (Molinari et al. 1998a). Apart from outflows, disks and jets (including radio and ionized jets) are also very relevant to the formation and evolution of massive stars (Purser et al. 2016 and Feeney-Johansson et al. 2019), thus theoretically, the interaction between disks and jets protect stellar embryo from strong stellar radiation (Krumholz et al. 2009 and Kuiper et al. 2011). Additionally, jets drive mass and angular momentum away from these young massive stars (Frank et al. 2014).

Outflows and jets may be associated with disk winds (Frank et al. 2014) which sometimes can alter the structure, development and evolution of the surrounding accretion disk (Ahmadi et al. 2018). These outflows from young massive stars also contribute to the feedback mechanism for moving mass and energy back into the surrounding medium of the birth place of the young star.

Our recent knowledge of the formation and propagation of jet and outflows have been from observations of low mass stars, that is, knowledge of dynamical parameters such as the outflow density, temperature and velocity (as seen in Hartigan and Morse 2007). Also, from Blandford and Payne (1982) and Pudritz et al. (2007), it is now established that the basic framework describing the process of outflows or jets from protostars with low mass is the one consisting of a disk-wind with magnetic and centrifugal (magneto-centrifugal) forces at play. In terms of massive stars, Beuther et al. (2002) and Zhang et al. (2005) have suggested that, though outflows are frequently observed in low-mass stars, they are also present in massive stars. This observation justifies the need for direct study of these outflow processes in massive stars. With respect to this work, the jets related to the cores of young massive stars release thermal emission that can be detected as radio continuum at centimetre wavelengths as shown by Purser et al.

(2016) and Moscadelli et al. (2019). One of the goals of this work is to detect such emission in our target fields.

## 1.9 Theories and models behind the formation of massive stars

A major fundamental problem in massive star formation is the the radiation pressure problem (Kahn 1974, Yorke and Sonnhalter 2002 and Krumholz and McKee 2005). That is, during the lifetime of massive stars, they exert a radiation pressure onto their surroundings which is greater than their gravitational attraction. For years, astronomers were puzzled by how these massive stars sustain accretion. In essence, this radiation pressure could be sufficiently strong to cease further accretion. This would mean that adaptations had to be made to the standard theory of low-mass star formation in order to account for the formation of massive stars. Several theories have suggested to solve this problem, some of which include increasing accretion rates in turbulent cloud cores (McKee and Tan 2003), accretion through disks (Yorke and Sonnhalter 2002), escape of radiation through windblown cavities (Krumholz and McKee 2005) among others. To understand how massive stars form, we consider two key models, the core accretion and competitive accretion.

### 1.9.1 Core accretion/monolithic collapse

The core accretion (monolithic collapse) or the gravo-turbulent method involves the fragmentation of clouds (also described as turbulent Jeans' fragmentation, Pillai et al. 2011) under the effect of magnetic field, gravity and turbulence to form massive stars (McKee and Tan 2002 and Ballesteros-Paredes et al. 2007). Massive stars formed out of this process usually form in isolated regions (isolated from their parent environments) (Shu et al. 1987) and do not undergo further extensive breakdown. For example, Yorke and Sonnhalter (2002) have shown through hydrodynamics simulations the collapse of these isolated, nonmagnetic and rotating huge molecular cores with masses 30, 60 and 120 $M_{\odot}$. Additionally, these clouds at the collapse stage are associated with a massive change in angular momentum. This momentum is lost through outflows and the accretion disks which helps in conserving angular momentum (Sicilia-Aguilar et al. 2013). Observational studies of the fragmentation of cores into massive clumps via Jeans fragmentation have been shown to be consistent with the concept of monolithic collapse (Pillai et al. 2011). Also, the observational evidence of accretion disks, for example the study of the

disk in Cepheus A HW2 (Patel et al. 2005) and the evidence of a circumstellar disk around the massive protostar (IRAS 18162-2048) by Carrasco-González et al. (2012) is consistent with this theory.

### 1.9.2 Competitive accretion

Earlier on in high-mass stars research, one of the problems that astronomers were trying to find a solution to was why massive stars have masses greater than the Jeans' masses of their associated molecular clouds. This question has been solved by the competitive accretion model (here, most of the stellar mass is accreted through competitive accretion in a clustered environment, Bonnell et al. 2004). In the competitive accretion model (Figure 1.8 shows a simulation of the concept of competitive accretion by Bonnell and Bate 2006), the gravitational collapse of a dense (massive) cloud produces a protocluster (that is embedded in its gas cloud). This protocluster triggers the accretion of material or matter from its embedded gas environment via its gravitational potential energy. This process goes on until the protocluster accretes most of the gas into its close vicinity. This then begins a fight for material by the protostars in this protocluster. In the end, this leads to the formation of massive cores at the centres of the protocluster's potential well, and hence initial masses higher than the Jeans' mass. Recently, through observations such as the RMS survey (Urquhart et al. 2007 and Lumsden et al. 2013) one of the key ideas of the competitive accretion model (increase in the accretion rate with a growth in mass of the protostar) have been shown to be consistent with observations. That is, simulations of young massive stars were matched with observations and their results were best explained by an accretion rates which increase with increase in mass of a protostar as it grows, as predicted by the competitive accretion model (Davies et al. 2011).

## 1.10 The CORE program

The IRAM Northern Extended Millimeter Array (NOEMA) CORE large program (Beuther et al. 2018) from a statistical standpoint seeks to provide answers to questions like, with respect to the formation of massive stars, what are the fragmentation characteristics of gas clumps? And how does fragmentation affect the stellar environment? What mechanisms lead to the formation of accretion disks? (Beuther et al. 2018). Answers to these questions are vital to understanding massive star formation as they help reveal the process of star formation at small scales (for

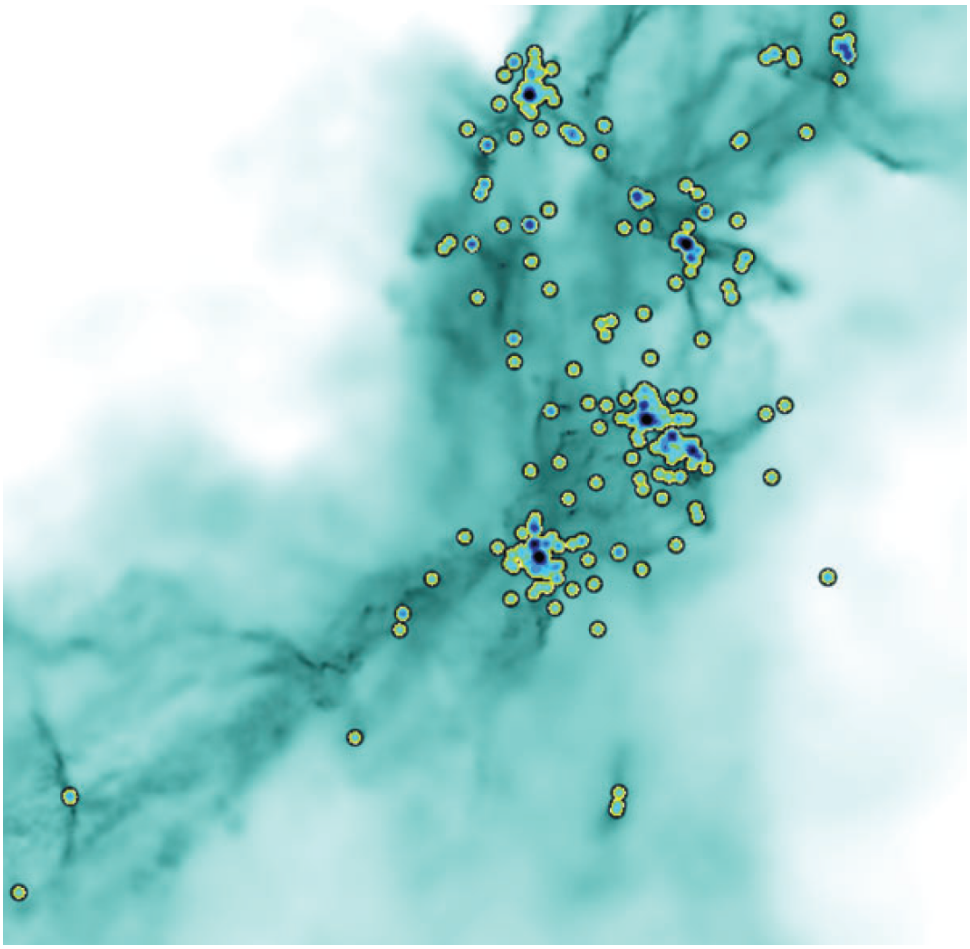

Figure 1.8 | **Competitive accretion simulation.** Here in the image (a simulation showing the concept of competitive accretion), we see massive stars as dark blue circles just in the middle of single subclusters of stars with low masses (shown as light circles). The subclusters are low mass stars due to less activity of competitive accretion and grow mainly by the collision or merging with other diminutive clusters present. Reference: Zinnecker and Yorke (2007).

example at Jeans length). NOEMA's configuration provides the spatial resolution required to address these questions and probe the northern-hemisphere sample of massive star forming regions. From the fragmentation of gas blocks, disk fragmentation and formation, phenomenon related to the infall of ionized and molecular gases to exploring the chemical evolution of outflow or jet characteristics, the CORE large program seeks to provide insight into all these processes.

CORE observed a sample of 20 sources in the millimeter range (1.37 mm) in 3 different array configurations using NOEMA/IRAM with total observation of more than 320 hours. The data-sets for these observations were supplemented with the IRAM 30m single dish telescope at short-spacing, with all the combined data-set covering a spatial scale of resolution limit of about 0.33 arcseconds to most of the sample's extended sources. In the 1.37 mm band at an angular resolution of approximately $0.3''$ to $0.4''$ covering frequencies between 217.15 to 220.79

GHz. The data was collected at a spectral resolution of 1.95 MHz, which corresponds to a velocity resolution of approximately 2.7 km/s at the given frequencies. CORE also covered a sub-sample observed in the 850 micrometres band at about 356 GHz with NOEMA at a spatial resolution of about $0.2''$ in the extended A-array (baseline of 368m in the N-S direction). Of these 20 sources, 14 (data from 2 of these sources have not been published) have previously been observed with JVLA at C (5.8 GHz) band at a resolution of $0.33''$. Observations of the other 6 were made with JVLA also at C band (5.8 GHz) in A configuration under project ID 18A-104.

## 1.11 A review of the 12 CORE sources

In this section, we present a review mainly using radio and millimetre data on the 12 CORE sources whose data have been published prior to this work. Later in this thesis, we use this information to provide a quantitative analysis of the entire CORE sample.

### 1.11.1 G133.9476+01.0648 (W3($H_2O$))

W3($H_2O$) or TW Object (discovered through an 88.6 GHz observation by Turner and Welch 1984) is a young stellar object and found in the W3 high-mass star-forming region and is associated with water masers (Dreher and Welch 1981). There is a suggestion of the presence of an outflow towards the east-west direction (Hachisuka et al. 2006).

In terms of radio wavelength studies, W3($H_2O$) has been studied with VLA at 8 and 15 GHz (Reid et al. 1995) and 8.44 GHz (Wilner et al. 1999) all in A configuration. These studies have shown the presence of a jet (there is a suggestion that this jet is precessing) in the field. Similarly, emission have been detected (Reid et al. 1995 and Wilner et al. 1999) and associated to W3($H_2O$) with an indication of the presence of a circumstellar disc (Shchekinov and Sobolev 2004). Wyrowski et al. (1999) has also studied this target (source A) at 220 GHz and detected sources A, B and C (one at the location of a water maser outflow, synchrotron jet and radio continuum source, see Wyrowski et al. 1999 for more details) and reports peak fluxes of 185, 145 and 150 mJy beam$^{-1}$ respectively. To confirm outflow activity in this field, Zapata et al. (2011) detected a bipolar outflow.

In a recent millimetre study by Beuther et al. (2018), they found up to 7 cores associated with W3($H_2O$). These 7 cores have masses between 13 and 1 $M_\odot$. Our source position, matches with

the 10 $M_\odot$ core in their millimetre image (see Beuther et al. 2018 for more details). In terms of outflows in W3($H_2O$), previous observations (for example Wilner et al. 1999 and Wyrowski et al. 1999) showed the presence of a double-sided jet which has been confirmed by a high angular resolution study by Zapata et al. (2011).

### 1.11.2 G138.2957+01.555 (AFGL 402d)

G138.2957+01.555 or AFGL 402d is known as a luminous Herbig Be star (Ray et al. 1990), similar to Herbig-Haro (HH) objects. HH-like jets (described as optical jets by Buehrke et al. 1988) have been reported to emanate from G138.2957+01.555 (Ray et al. 1990).

Studies by Kurtz et al. (1994), Carral et al. (1999) (both at 8.3 GHz), Obonyo (2020) (at 1.5 GHz) and Purser et al. (2021) (at 5 GHz), all observed G138.2957+01.555 with VLA and reported integrated fluxes of 2.1, 0.12, 0.13 and 0.42 mJy respectively. Recently, Navarete et al. (2015) have detected and mapped a bipolar outflow in the field. Additionally, Obonyo (2020) classifies G138.2957+01.555 as a lobe (non-thermal in nature) and is associated with another source C (see Obonyo 2020 for details).

At millimetre wavelength, Beuther et al. (2018) have detected 3 cores in this field. The YSO position coincides with the millimetre core 1 which has a mass of 11.6 $M_\odot$. The morphology of the region suggests the presence of an outflow activity, specifically, the orientation of core 3 with respect to the YSO.

### 1.11.3 G139.9091+00.197 (AFGL 437S)

Purser et al. (2021) have detected 5 sources in this field (at 5.8 GHz) labelled A, Ab, Ac, B and HII. See Purser et al. (2021) for more details. A is our target source. They measured an integrated flux of 0.60 $\pm$0.02 and 0.54 $\pm$0.01 mJy for A. The YSO is associated with sources Ab and Ac. In particular, Ac seems to be an extension of A.

At millimetre wavelengths, we see 2 detected cores, 1 and 2 which are at a distance of 32468 AU apart with masses of 2.4 and 0.8 $M_\odot$ respectively. The YSO position matches with source 1. See Beuther et al. (2018) for details.

### 1.11.4 S87 IRS1 (G060.8842-00.1286)

S87 IRS1 is known to have a cometry radio and mid-IR morphology (Kalcheva 2018) and classified as an ultra-compact HII region (CORNISH survey, Hoare et al. 2012). At 5 GHz (using information from CORNISH survey), S87 IRS1 has an integrated and peak flux of 18.67 $\pm$1.96 mJy and 18.67 $\pm$1.76 mJy beam$^{-1}$ respectively. Recently, Kalcheva (2018) reported a flux of 4.89 $\pm$0.64 mJy at 22 GHz for this object.

From Beuther et al. (2018), we notice S87 IRS1 is a busy field with up to 11 cores in the field. Core 2 which has a mass of 0.3 $M_{\odot}$ corresponds with our YSO position. To the north is core 7, which seems to be associated with the YSO. Core 3, which is to the south-east of the YSO, looks like it fragmented from the YSO and core 7.

### 1.11.5 S106 (G076.3829-00.6210)

S106 or S106R (Hoare et al. 1994) is classified as an HII region and was observed at 9 GHz by Kurtz et al. (1994) with integrated and peak fluxes of 14.9 mJy and 10.2 mJy beam$^{-1}$ respectively. Combining VLA and e-MERLIN observations at 5 GHz, Hoare et al. (1994) resolved S106 (see Hoare et al. 1994 for details). Hoare et al. (1994) reported an integrated flux of 8.9 $\pm$0.9 mJy with a deconvolved size of $0.224'' \times 0.060''$. Hoare and Muxlow (1996) studied S106 at 23 GHz and reported the presence of two radio peaks (integrated flux of 12.1 $\pm$2.00 mJy) in the field. More recently, S106 has been observed by Sanna et al. (2018) using VLA's A configuration at 13 GHz and 6 GHz band and configuration B at 22 GHz. Sanna et al. (2018) recorded SED integrated fluxes of less than 0.048, 0.068 and 0.057 mJy respectively. Comparing the old VLA flux values, there seem to be a decrease in flux, hence pointing to a possible variability of the source.

Beuther et al. (2018) detects 2 cores in this field. Core 1 is our YSO and has an estimated mass of 1.0 $M_{\odot}$. It is not clear if the second core is associated with our YSO, however the orientation and distance between the two cores may suggest that core 2 is as a result of emission from the YSO (since we know this YSO is classified as an HII region via the RMS survey, Lumsden et al. 2013).

### 1.11.6 G084.9505-00.691

G084.9505-00.691 is associated with 2 sources A and B, a jet candidate (Purser et al. 2021) and our target source respectively. Sources, A and B, have positions RA: 21:55:31.73 DEC: 44:05:11:32 and RA: 20:55:32.51 DEC: 44:06:10.26 respectively (where RA and DEC denote the right ascension and declination respectively). Purser et al. (2021) reports integrated and peak flux values (at 5.8 GHz using VLA) of 0.16 ±0.01 mJy and 0.13 ±0.01 mJy beam$^{-1}$ for A respectively. B was not detected at 5.8 GHz. Analogously, Purser et al. (2021) also observed both sources at 44 GHz, however only source B was detected with integrated and peak fluxes of 0.28 ±0.05 mJy and 0.25 ±0.03 mJy beam$^{-1}$ respectively.

For this object, 8 cores were detected at millimetre wavelength (Beuther et al. 2018). Our YSO position coincides with core 1 with a mass of 9.0 $M_{\odot}$. Clearly, these cores seem to belong to one large non-uniform structure. The morphology suggest the movement of material (with extended structures visible in the field), probably emission from the YSO (core 1) towards the other cores (this is likely to be the scenario since we know core 1 is a jet from radio analysis). It is also possible that core 2 may be also emitting some emission, perhaps an emerging young stellar object. Alternatively, core 1 could have influenced the formation of the other cores or these cores are all undergoing fragmentation.

### 1.11.7 G094.6028-01.797

G094.6028-01.797 consists of a thermal radio core (source A) and is a variable protostar (Cohen 1977). G094.6028-01.797 has been studied by Di Francesco et al. (1997), Clarke et al. (2006) among others. They have all suggested that this source is variable. Clarke et al. (2006) have measured a flux of 0.55 ±0.18 mJy (at 8.3 GHz) for this YSO. More recently, Obonyo (2020) recorded a flux of 0.32 ±0.03 mJy (5.8 GHz). Obonyo (2020) reports that the YSO possesses a disk (circumstellar), accretes material and drives a bipolar outflow. Aside the YSO, an associated non-thermal radio source, has been detected in the field (Obonyo 2020). The presence of the non-thermal radio source points to the fact that there could be gas collision processes present or associated with this YSO.

The millimetre image of G094.6028-01.797 divulge 2 main regions, one region harboring 3 cores (1, 2 and 4) and the other with one core 3 (see Beuther et al. 2018 for details). Our YSO's position correlate with core 1 and has a mass of 36.9 $M_{\odot}$. The presence of core 3 is likely to be

due to an outflow phenomenon in the field, particularly from the YSO (we know that this YSO is likely to be a jet from the radio image in the study by Purser et al. 2021). Cores 2 and 4 may have been formed due to the release of emission from the YSO via jets into its immediate vicinity.

### 1.11.8 G100.3779-03.578

G100.3779-03.578 is associated with 2 sources, A (our target source) and B, as see Purser et al. (2021) for more details. A is classified as a Jet and B an HII region (Purser et al. 2021). A study at 5.8 GHz by Purser et al. (2021) estimates an integrated and peak flux value of 0.09 $\pm$0.01 mJy and 0.08 $\pm$0.01 mJy beam$^{-1}$ respectively for A and 0.09 $\pm$0.01 mJy and 0.05 $\pm$0.01 mJy beam$^{-1}$ for B. At 22 GHz, A has an integrated and peak flux value of 0.45 $\pm$0.07 mJy and 0.39 $\pm$0.04 mJy beam$^{-1}$ respectively. Similarly, source B has a flux of about 0.12 mJy at 22 GHz (Purser et al. 2021).

Similar to IRAS 21078, G100.3779-03.578 is a very complex field with 20 detected cores at 1.37 mm (Beuther et al. 2018). Our YSO corresponds with the position of core 1 with a mass of 2.2 $M_\odot$. The mean, minimum and maximum separation between cores in G100.3779-03.578 are 3027, 1573 and 7247 AU respectively (Beuther et al. 2018). There is a presence of high density extended structures with an associated field temperature of 58 K with emission being directed away from the parental core (the YSO) towards the north-west and south directions.

### 1.11.9 G108.7575-00.986

G108.7575-00.986 is associated with 5 sources, A (jet candidate), B, C, D, and E. All these sources have been detected and studied by Purser et al. (2021) at 5.8 GHz (C-band) and 44 GHz (Q band). Source A is our target field. At 5.8 GHz, Purser et al. (2021) measured integrated fluxes of 0.12 $\pm$0.01, 0.02 $\pm$0.01, 0.08 $\pm$0.01, 0.03 $\pm$0.01 and 0.06 $\pm$0.02 mJy for sources A, B, C, D, and E respectively. Also at 44 GHz, sources A, B, C, D and E have integrated fluxes between 0.13 and 0.31 mJy (Purser et al. 2021).

A 1.37 mm study of G108.7575-00.986 by Beuther et al. (2018) have detected 3 cores (labelled 1, 2 and 3, see Beuther et al. (2018) for details) which have masses of 10.8, 4.8 and 3.8 $M_\odot$ respectively. The morphology of the field both suggests the occurrence of fragmentation and probably a jet activity. The position of our YSO (which is a jet candidate) correlate with that

of core 1 which may explain the morphology seen (emission from the YSO in the north-east direction and the presence of cores towards the eastern part of the field). It is not clear if cores 2 and 3 have any association with the YSO, nevertheless we suspect that these cores may be as a result of emission from the YSO.

### 1.11.10 IRAS 23033+5951 (G110.0931-00.0641)

IRAS 23033+5951 is a complex field, containing a massive star. A radio study by Obonyo (2020) has shown that this field harbours 4 sources: A, B, C and D. Purser et al. (2021) have also studied this field and detected sources labelled A1, A2, B, C and D. Our target source is B. Obonyo (2020) reports integrated fluxes of 0.59 ±0.08 mJy (at 1.5 GHz), 0.95 ±0.13 mJy (at 5.8 GHz) and 1.03 ±0.20 mJy (at 44 GHz) for all 3 sources (A+B+C). Additionally, source D have fluxes of 0.19 ±0.03 mJy (at 1.5 GHz) and 0.17 ±0.02 mJy (at 5.8 GHz) (Obonyo 2020). Surprisingly, a previous radio study by Purser (2017) of this target did not detect source D which may be due to sensitivity limit of the observation. Obonyo (2020) suggests that sources A and C are likely to be jet lobes which are associated with the YSO.

A study by Beuther et al. (2018) at millimetre wavelength has detected 4 cores in this field. One of those cores position matches with that of our YSO. This core (core 1) has the highest mass of 30.5 $M_{\odot}$. There are 3 other cores (cores 2, 3 and 4) with masses 11.4, 19.1 and 1.2 $M_{\odot}$ respectively. Furthermore, a recent study by Bosco et al. (2019) has also detected these 4 cores in this field. Their study also suggests that source B (where B is MMS1a in their study) is the most evolved core among the other cores detected. They believe that MSS1a together with the other cores fragmented from the same parental cloud. There is clear evidence of fragmentation in this field as is observed by the positions and structures around the cores. Uniquely, unlike most of the other CORE targets discussed already, this field is dominated by more than one high-mass core. Furthermore, the millimetre studies (Beuther et al. 2018 and Bosco et al. 2019) suggest that cores B and A are possibly driving outflows. Which may be manifestation of structures to the north-west of core 1.

### 1.11.11 NGC 7538IRS9 (G111.5671+00.7517)

First discovered by Werner et al. (1980), NGC 7538IRS9 is a massive protostar (compact luminous infrared source) found in the NGC 7538 region (Mitchell and Hasegawa 1991). In NGC 75381RS9, high-velocity gas has been detected and associated with a bipolar outflow (Kameya

et al. 1989). Mitchell and Hasegawa (1991) measured velocities of 110 $kms^{-1}$ for this outflow.

Earlier studies at 4.86 GHz, 8.46 GHz and 15 GHz by Rengarajan and Ho (1996) and Sandell et al. (2005) respectively have detected a single source for NGC 7538IRS9 (labelled 'A' in a recent image by Obonyo 2020) and measured fluxes of 0.51, 1.00 and 0.76 mJy respectively. Also, a study by Sánchez-Monge et al. (2008) at 8.3 and 23 GHz (using VLA) showed a double and single source respectively. Also, Obonyo (2020) has detected 3 sources A, B and C in this field. More recently, Purser et al. (2021) detected these 3 sources and an additional source D. Source B seem to breakdown into 2 sources or lobes B1 and B2 (Purser et al. 2021).

Beuther et al. (2018) have studied NGC 7538IRS9 and detected 9 associated cores. Our YSO position correlates with core 1 which has a mass of 2.79 $M_{\odot}$. The morphology (presence of high density structures around core 1 and destruction of the parental core environment) suggests an outflow or jet activity in the field which supports the observed radio morphology or structure and classification of NGC 7538IRS9 as a jet with lobes (Beuther et al. 2018).

### 1.11.12 IRAS 23151+5912 (G111.2348-01.2385)

IRAS 23151+5912 has been studied at 22 GHz by Wouterloot and Walmsley (1986), Zuckerman and Lo (1987) and Scalise et al. (1989). They have suggested that this source is associated with an object (pre-main sequence) and deduced its luminosity to be between $10^4$ and $10^5$ $L_{\odot}$. IRAS 23151+5912 is associated with source A (a jet candidate). Purser et al. (2021) reports an integrated and peak flux of 0.16 ±0.01 mJy and 0.15 ±0.01 mJy $beam^{-1}$ at 5.8 GHz respectively. Also, fluxes of 1.46 ±0.09 mJy and 1.04 ±0.04 mJy $beam^{-1}$ at 22 GHz respectively (Purser et al. 2021).

At 1.37 mm, 5 cores have been detected (Beuther et al. 2018). Our YSO position coincides with core 1 which seem to be ejecting material toward the north and south directions (as seen by the disruption of material around core 1). Beuther et al. (2018) measured a mass of 3.32 $M_{\odot}$ for this core. The observed jet-like morphology (presence of high density structures) at millimetre wavelength is important as it provides further evidence to support outflow activity in this field since this is not so obvious in the radio images by Purser et al. (2021).

## 1.12 VLA observations

Located at an elevation of 2100 meters on the Plains of San Agustin in southwestern New Mexico, JVLA or VLA is a 27-element interferometric array, arranged along the arms of an upside-down Y (with respect to the observing position), which produces images of the radio sky at a wide range of frequencies and resolutions. The basic data produced by VLA are the visibilities (formed by correlation of signals from the array's elements). VLA has four basic antenna arrangements or configurations, the D, C, B, and A with maximum baseline of 1.03, 3.4, 11.1 and 36.4 km respectively. Data used in this project was collected in VLA's A array configuration. All VLA antennas come with eight receivers which provide a continuous frequency coverage from 1 to 50 GHz, with the 4-8 GHz range covering the C-band (as used in the project).

## 1.13 Thesis motivation and outline

As highlighted earlier, it is important to study our sample of massive stars especially at 0.33 arcseconds resolutions since this matches with what we are obtaining with NOEMA at millimetre wavelength. This allows us to examine in detail the morphology of these massive stars (for example, the relationship between the dust disc and the ionized jet if present). Studying massive stars at radio wavelengths, helps us to detect and understand (since they are optically thin to the envelope surrounding these massive stars) some of the complex processes (for instance, outflows, discs and jets) related to these structures. In this research, we study the high resolution continuum maps of the radio jets of objects selected from the on-going CORE program. Specifically, this work studies 8 of remaining targets or sources (2 have been observed by Purser et al. (2021) using VLA under project code 12B-14 in the field NGC 7538IRS9 and the other 6 we have now observed also with VLA under project code 18A-104) from the 20 CORE sources as well as investigate the properties of all 20 sources.

With this study, we hope to understand the varying nature of these targets (in terms of their radio jets, since this study is being conducted at a high resolution). Again, with this research, we hope to explore trends, phases and properties of the jets and discs. Furthermore, we hope to answer the questions: Are outflows or jets always accurately perpendicular to their disc or millimetre emission? What are other underlying mechanisms for the existence of outflows and jets in young massive stars? Are jets associated with young massive stars produced through

scaled-up processes of their low-mass counterparts? In the end, these data-sets are going to help us explore the phenomenon of massive star formation processes in much more detail. Also, another target of this research is to investigate the disc-jet mechanism and orientation observed in massive star formation (Krumholz et al. 2009 and Kuiper et al. 2011). At the moment, there is not enough high spatial resolution observations (at radio and millimetre wavelengths) to investigate some of the questions outlined above.

In the current Chapter ( 1), we have covered some important background information about the study of massive stars and explored the 12 CORE targets with published data. In Chapter 2, we provide information on the observation and data reduction of our 6 targets plus 2 targets found in the Purser et al. (2021) data-set which have not been published prior to this work. In Chapter 3, we present our results for the 8 targets. Additionally, we use our results and millimetre information available on 8 targets to discuss and analyse the overall properties of our 8 targets (including an attempt to answer some of the questions about the properties of jets from young massive stars). Also, we characterize the overall properties of the 20 CORE targets and provide a summary of the research and point out our conclusions in Chapter 4.

# Chapter 2

# Data reduction

## 2.1 Sample

The 6 objects listed in Table 2.1 are part of the remaining CORE sample sources which do not have any JVLA data prior to this work. Most of the other sources have been observed as part of the Leeds based programme (12B-140, Purser et al. 2021) or have similarly deep observations available in the archive or published for example in Purcell et al. (2013). The CORE project (Beuther et al. 2018) has $0.3''$ resolution at roughly 1.37 mm on a sample of 20 luminous (L $>10^4$ solar luminosities, showing that a star with at least 8 $M_\odot$ is forming in the region), nearby (d <6 kpc to provide a high spatial resolution) and are at a high declination. Also, these targets all have extensive complimentary high resolution observations or data at other wavelengths thus ensuring that their overall properties can be characterized (Beuther et al. 2018). In other words, the CORE sample comprise of well-studied massive young stellar objects in the northern sky. Table 2.1 shows the distances and luminosities of our targets (18A-104) and the those that belong to the Purser et al. (2021) data-set.

## 2.2 Interferometry

With respect to astronomy research, this is the process of combining signals from two or more telescopes or antennas in a unique way that these signals are correlated to form a sharp image. Long baselines hold information about the small scale structure of the source but are insensitive to large scale structure while short baselines hold information about large scale structure of the source but are insensitive to small scale structure (due resolution restriction or limit) (Herring

| Sample name | RA(J2000) | Dec(J2000) | Distance(kpc) | Luminosity ($10^4 L_\odot$) |
|---|---|---|---|---|
| G133.6945+01.2 | 02:25:30.10 | +62:06:20.90 | 2.00 | 4.50 |
| G075.7822+00.3 | 20:21:44.10 | +37:26:39.60 | 3.80 | 11.0 |
| G078.8867+00.7 | 20:29:24.86 | +40:11:19.40 | 3.30 | 20.0 |
| IRAS21078+5211 | 21:09:25.21 | +52:23:43.70 | 1.50 | 1.30 |
| G109.8715+02.1 | 22:56:17.98 | +62:01:49.70 | 0.70 | 1.50 |
| IRAS23385+6053 | 23:40:54.49 | +61:10:27.90 | 4.90 | 1.60 |
| Purser et al. 2021 targets | | | | |
| NGC 7538S | 23:13:45.14 | +61.26.49.18 | 2.70 | 1.50 |
| NGC 7538IRS1 | 23:13:45.36 | +61.28.10.16 | 2.70 | 21.0 |

Table 2.1 | **18A-104 and Purser et al. 2021 target fields .** All our target fields with their coordinates, distances and luminosities: values taken from Beuther et al. (2018).

et al. 1986).

In practice astronomers use many antennas (for example the VLA has 27 antennas) to make observations of stellar objects (sources), say a massive star. The signals from the massive star are amplified and digitized. This is then sent to central location to perform cross-correlation using a correlator which takes advantage of earth rotation to fill in details about the "aperture". An inverse Fourier Transform of the source is obtained (since the visibility or data of an interferometer gives information about the Fourier Transform of the sky brightness distribution) to get an image. Any antenna or observation related errors (for instance calibration errors) are corrected and then the final image is made through data reduction (for example, VLA data reduction is performed in CASA) (Thompson et al. 2017).

## 2.3 Observations

The 6 objects were observed on the 6th, 7th and 17th of May 2018, using JVLA in the A configuration array (maximum and minimum baseline length of 36.4 and 0.68 km respectively and a largest angular scale of 8.9 arcsecs) under project code 18A-104. Three of the target sources were observed on two separate days (6th and 7th May 2018, 18A-104...44.ms and 18A-104...85.ms) and the others on the last day of observation (17th May 2018, 18A-104...98.ms), all these corresponding to a time on source and on calibrator of about 7 minutes (totalling 14 minutes per source) and between 4 to 2 minutes per scan respectively. There were 19 scans in all, with an average integration time of the individual scans for the calibrators and sources being 2 minutes. Our observational study of these 6 young massive stars with JVLA is associated with a noise level of roughly 6 μJy.

All the observations were done using the JVLA's 27 antennae at a resolution of approximately $0.33''$. Continuum data were observed in 48 spectral windows (SPWs) and one unique polarization setup, with a total bandwidth of 3 GHz. The spectral windows are subdivided into 64 channels, with a 2 MHz (at a velocity of approximately 90 $\mathrm{kms}^{-1}$) width each. The sources were observed at C-band with corresponding frequencies between 4.5 and 7.9 GHz. A 6.7 GHz methanol maser line was observed, which could be used as a calibrator if required.

Aside from our own observations, we imaged 2 targets from the Purser et al. (2021) data-set. These targets were observed under the project code 12B-140 by M.G. Hoare (P.I) using VLA's A configuration. Data were observed in 16 spectral windows of 2 MHz channel width and a frequency range of 4.8 to 6.7 GHz (centred on 5.8 GHz). There were 115 scans in all. The observations are associated with a synthesized beam width of about 0.3 arcsec and a primary beam size at FWHM of approximately 430 arcsec. On-source times for the science targets were between 24 and 26 minutes corresponding to an rms noise of 6 $\mu\mathrm{Jybeam}^{-1}$ (Purser et al. 2021).

## 2.4 Flagging

After obtaining data from the NRAO archive, editing and flagging was performed using CASA version 6.4.0.16 (McMullin et al. 2007). After inspecting the data, manual flagging was performed as follows: the beginning and end of scans were clipped or flagged (at a 10 seconds interval), for our observations, spectral windows 0 to 15 which were observed from scan 1 to 3, were flagged as they were performed as part of system configurations. The 6.7 GHz methanol maser line observed was also flagged as it was not required for calibration (the methanol maser was in the SPW 33).

For the data-set 18A-104...98.ms antennas 11 (ea13) and 20 (ea22) were flagged as they lost or had corrupted data (known from information provided in the observer log) respectively. Apart from SPW 33 (maser channel) which was flagged, some channels in SPWs 35, 40, 43 and 47 were flagged as they had some noisy data (heavily impacted with Radio Frequency Interference).

In addition, for the 18A-104...85.ms data-set, antenna 13 (ea15) was flagged as it lost its data. Similar to 18A-104...98.ms, SPW 33 (maser channel) was flagged. Also, some channels in SPWs 35, 42, 43, 44 and 47 were flagged as they had some noisy data (heavily impacted with Radio Frequency Interference).

Finally, from the observer log, there were no problems with the antennas for the 18A-104...44.ms data-set though SPW 33 (maser channel) and some channels in SPWs for example, 35, 42, 43, 44 and 47 were flagged as they had some noisy data (heavily impacted with Radio Frequency Interference). For this, interactive flagging was adopted for a more accurate flagging.

## 2.5 Calibration and imaging

Before calibration, the data-set was examined using information from the observer log thus checking observing conditions during the observing run and identifying any known problems with the data and flagged as outlined in Section 2.4 above. Calibration and imaging were performed using CASA version 6.4.0.16. Following a manual calibration procedure, a priori antenna position corrections, flux density scaling, phase, delay, bandpass and gain calibrations were performed respectively (using the CASA Karl G. Jansky VLA continuum tutorial calibration and imaging guidelines available at VLA Continuum Tutorial using the downloaded ms data-set obtained from the NRAO archive website) firstly for the calibrators. Once the calibrators were calibrated, the calibrations or solutions were applied to the respective targets (Table 2.4 shows the calibrators, their coordinates, fluxes and which targets they were used to calibrate). Afterwards, the calibrated data-sets were then split into their respective fields and imaged. After splitting and initial imaging, the initial models of the imaged fields were verified by comparing varying solution intervals (3, 6, 15, 60 and 90 seconds) and the desired minimum SNR condition of 3 applied and the targets all re-imaged.

For the 18A-104...98.ms data-set, separate calibrations was performed for SPWs between 16 - 31 and then for 32 - 47 (this was done because when calibration was done for SPWs 16 - 47 this failed which we believe was due to the fact that SPWs 16 - 31 and 32 - 47 were observed separately). The results of these two calibrations were then compared and were found to be similar (had the same rms sensitivity). Additionally, for data-set 18A-104...85.ms, calibration was done for all SPWs as normal.

Lastly, for the 18A-104...44.ms data-set, calibration was done for all SPWs as normal, however the calibrated data-sets 18A-104...44.ms and 18A-104...85.ms were combined and imaged, as they were observations of the same targets on different days (06-May-2018 and 07-May-2018). This was done to achieve better signal to noise.

### 2.5.1 Imaging

Target and calibrator imaging were done using the CASA task tCLEAN in the multi-frequency synthesis (mfs) mode. The various CLEAN components of the fields were identified from user defined regions and a script. To image our targets, a SNR greater than 10 (Brogan et al. 2018) was imposed and a phase-only self-calibration (Pearson and Readhead 1984) performed on some of our targets with solution intervals of 3, 6, 15, 30, 60 and 90 seconds and a range of 1 to 4 iterations performed until minimal scatter (phase scatter, as evidence in the phase vs time plot) for the respective target fields. The fields were imaged initially using a script before applying an interactive CLEANing (by imposing a user-defined region where only strong emission/peaks were specified and then weaker emission used in further CLEAN iterations). While performing CLEAN on data, the visibilities (UV) were weighted using Briggs weighting with a robustness parameter (R) of zero (Briggs 1995). The R = 0, provides a good balance between resolution and sensitivity. The hogbom clean (Hogbom and Brouw 1974), was used for both creation of initial images and CLEANing of subsequent images (prior to and after self-calibration). All targets and calibrators were imaged using a cell size of $0.07''$. In Table 2.3, we show all the various imaging parameters alongside the measured fluxes for our targets.

NGC 7538IRS1 (G111.5423+00.7776) and NGC 7538S (G111.5320+00.7593) are found in the Purser et al. (2021) field NGC 7538IRS9. To image them, the calibrated data-sets were split into the target fields and imaged using our phasecenters (shown in Table 2.2) and the same imaging parameters as the ones used for imaging our data-sets. Self-calibration was attempted for these targets, however there were not sufficient phase solutions for those self-cal runs to produce better images so we proceed with analysing the calibrated data only in this work.

## 2.6 Imaging the calibrators

Figure 2.1 shows all the calibrators after initial imaging. The calibrators are labelled in each image and the synthesized beam shown at the bottom-left corner of each image. The calibrators were imaged to show that they were point-like which helps to determine the system response to a source of known flux density. It also allows the data to be properly scaled with the amplitude gains and improves the quality of the overall calibration and imaging.

Table 2.2 shows objects and phase centers used for imaging them (including phasecenters for

a) J2230 - Phase/bandpass calibrator

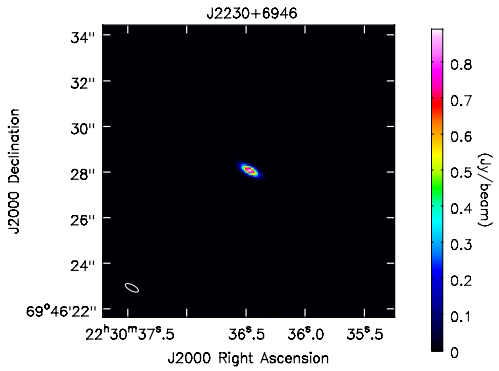


b) J0228 - Phase/bandpass calibrator

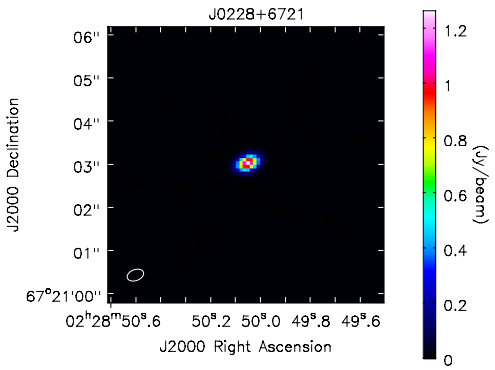


c) J2023 - Phase/bandpass calibrator

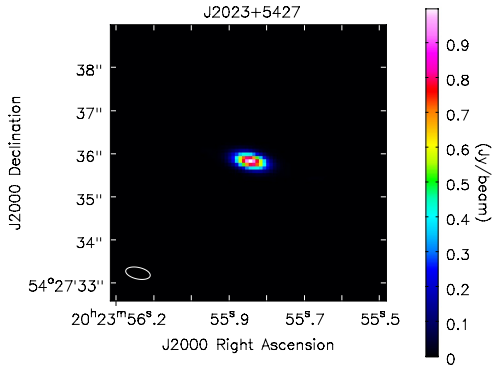


d) J2007 - Phase/bandpass calibrator

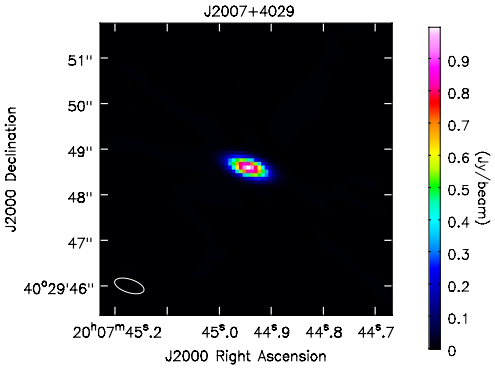


e) 3C48 - Flux calibrator

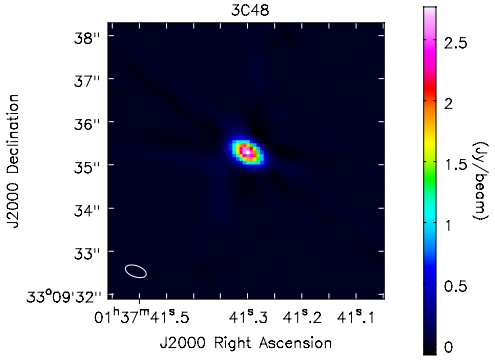


Figure 2.1 | **Calibrators.** Figure 2.1 shows our calibrators after initial imaging with their names. NB: The synthesized beam for each calibrator is indicated in the bottom-left corner of each image.

imaged targets from the Purser et al. (2021) data-set, those targets are indicated with an asterisk '*' as shown in the Table below).

| 18A Sample name | RA(J2000) | Dec(J2000) |
|---|---|---|
| G133.6945+01.2 | 02h25m31 | +62d06m21 |
| G075.7822+00.3 | 20h21m44 | +37d26m39 |
| G078.8867+00.7 | 20h29m24 | +40d11m19 |
| IRAS21078+5211 | 21h09m21 | +52d22m37 |
| G109.8715+02.1 | 22h56m18 | +62d01m47 |
| NGC 7538S* | 23h13m44 | +61d26m48 |
| NGC 7538IRS1* | 23h13m45 | +61d28m10 |
| IRAS23385+6053 | 23h40m54 | +61d10m28 |

Table 2.2 | **18A-104 phase centers.** Here, we present the phase centers used for imaging our targets. Targets taken from the Purser et al. (2021) data-set are indicated with an asterisk '*'.

Table 2.3 shows our target fields and their corresponding measured RMS and fluxes before self-calibration. For G133.6945+01.2, we do not detect the YSO but instead detect an HII region whose corresponding measured RMS and fluxes before self-calibration are presented in the table.

## 2.7 Comparing initial and self-calibrated images

We compared the measured RMS and fluxes before and after self-calibration to evaluate the effect of self-calibration on the data. Analysing the images and RMS values for the imaged targets after self-calibration revealed that there were several general changes to the structures in some of the targets fields which indicates that self-calibration did not improve the data. Failure of self-calibration could be due to insufficient solutions during the phase-only calibration leading to self-calibration and or due to over CLEANing during self-calibration. Notably, there was an increase in peak and integrated flux values for some of the sources after self-calibration. It is important to note that we proceed with analysing the calibrated data-set only in the rest of this work.

| Target name | RMS (mJy/beam) | Beam ($''$ (PA)) | $S_P$(mJy/beam) | $S_I$(mJy) |
|---|---|---|---|---|
| G133.6945+01.2 | 0.37 | $0.43'' \times 0.27''$ (-72$^o$) | 4.60 ±0.16 | 0.87 ±0.30 |
| G075.7822+00.3 | 0.04 | $0.65'' \times 0.29''$ (72$^o$) | 2.84 ±0.19 | 17.2 ±1.30 |
| G075.7822+00.3$_s$ | 0.04 | $0.65'' \times 0.29''$ (72$^o$) | 1.61 ±0.03 | 1.75 ±0.07 |
| G075$_{YSO}$ | 0.24 | $0.65'' \times 0.29''$ (72$^o$) | 0.62 ±0.02 | 0.77 ±0.05 |
| G078.8867+00.7 | 0.50 | $0.63'' \times 0.29''$ (74$^o$) | 1.68 ±0.04 | 47.4 ±1.10 |
| G078$_{YSO}$ | 0.10 | $0.63'' \times 0.29''$ (74$^o$) | 0.29 ±0.03 | 0.34 ±0.06 |
| IRAS 21078+5211$_{G1}$ | 0.01 | $0.49'' \times 0.27''$ (87$^o$) | 0.23 ±0.01 | 0.26 ±0.02 |
| IRAS 21078+5211$_{G2}$ | 0.01 | $0.49'' \times 0.27''$ (87$^o$) | 0.10 ±0.01 | 0.10 ±0.01 |
| IRAS 21078+5211$_H$ | 0.01 | $0.49'' \times 0.27''$ (87$^o$) | 0.10 ±0.01 | 0.10 ±0.01 |
| G109.8715+02.1 | I:0.08 | I: $0.76'' \times 0.27''$ (60$^o$) | I:1.75 ±0.06 | I:1.63 ±0.12 |
| | II:0.08 | II :0.76"×$0.27''$ (60$^o$) | II:3.02 ±0.35 | II:9.10 ±1.40 |
| | III:0.08 | III :0.76"×$0.27''$ (60$^o$) | III:0.67 ±0.01 | III:1.90 ±0.24 |
| | IV:0.08 | IV :0.76"×$0.27''$ (60$^o$) | IV:0.87 ±0.01 | IV:4.18 ±0.36 |
| | V:0.08 | V :0.76"×$0.27''$ (60$^o$) | V:2.83 ±0.18 | V:3.80 ±0.43 |
| NGC 7538S$_A$ | 0.19 | $0.31'' \times 0.30''$ (33$^o$) | 0.20 ±0.01 | 0.39 ±0.03 |
| NGC 7538S$_B$ | 0.34 | $0.31'' \times 0.30''$ (33$^o$) | 0.81 ±0.01 | 2.49 ±0.20 |
| NGC 7538S$_C$ | 0.21 | $0.31'' \times 0.30''$ (33$^o$) | 0.23 ±0.02 | 1.98 ±0.16 |
| NGC 7538IRS1$_M$ | 2.99 | $0.31'' \times 0.30''$ (33$^o$) | 14.12 ±0.80 | 56.0 ±3.90 |
| NGC 7538IRS1$_N$ | 1.93 | $0.31'' \times 0.30''$ (33$^o$) | 2.08 ±0.13 | 15.3 ±1.00 |
| IRAS 23385+6053$_Q$ | 0.02 | $0.66'' \times 0.27''$ (68$^o$) | 0.47 ±0.01 | 0.51 ±0.03 |
| IRAS 23385+6053$_R$ | 0.02 | $0.66'' \times 0.27''$ (68$^o$) | 0.18 ±0.01 | 0.19 ±0.02 |

Table 2.3 | **Measured target parameters.** All our target fields with their measured RMS, beam size and PA, peak and integrated flux values after initial imaging (pre-selfcalibration) determined from the Gaussian fit method in CASA viewer. **Notes**: The associated cell size (for imaging), synthesized beam size and image size are 0.07 $''$, 0.33 $''$ and 640 × 640 pixels respectively. Primary-beam correction was applied to the final images. Where RMS, $S_P$ and $S_I$ are the RMS, peak and integrated flux before self-calibration respectively. Initial imaging of G109.8715+02.1 revealed five different sources (labelled I to V, the highest flux source is II). For IRAS 23385+6053 and NGC 7538IRS1 imaging revealed two sources. Additionally, for fields G075.7822+00.3, G078.8867+00.7, IRAS 21078+5211 and NGC 7538S we detect three associated sources. G133.6945+01.2 had an HII region in the field. Positions of all detected sources for each field are outlined in Section 3.1 under the discussion of the individual targets.

| Calibrator | Type | RA(J2000) | Dec(J2000) | Flux (Jy) | Calibrated Object |
|---|---|---|---|---|---|
| 0137+331=3C48 | Flux | 01:37:41.30 | +33.09.35.13 | 4.588 | All sources |
| J2230+6946 | Phase/Bandpass | 22:30:36.47 | +69.46.28.08 | 0.897 | G109.8715+02.1, IRAS23385+6053 |
| J0228+6721 | Phase/Bandpass | 02:28:50.05 | +67.21.03.03 | 1.250 | G133.6945+01.2 |
| J2007+4029 | Phase/Bandpass | 20:07:44.94 | +40.29.48.60 | 0.999 | G075.7822+00.3, G078.8867+00 |
| J2023+5427 | Phase/Bandpass | 20:23:55.84 | +54.27.35.83 | 0.999 | IRAS21078+5211 |

Table 2.4 | **Calibrators for targets.** Calibrators, their fluxes at C-band and the corresponding objects that they were used to calibrate.

# Chapter 3

# Results and discussion

## 3.1 Radio continuum results: 18A-104 targets

### 3.1.1 G133.6945+01.2 (W3 IRS 4)

G133.6945+01.2 is found in W3, a well-known region of radio continuum emission with a 5 arcminute diameter core of multiple compact and ultracompact HII regions and infrared sources. In terms of radio emission, W3 has been studied extensively by Wynn-Williams et al. (1972), Harris and Wynn-Williams (1976), Colley (1980), Ladd et al. (1993) and Tieftrunk et al. (1997). W3 contains several regions labelled A to H, J, K and M, see Colley (1980) for details. Claussen et al. (1994) have studied W3 at 15 and 22 GHz and states that W3 (C) (an ultracompact HII region) is associated with W3 IRS 4 (our target source).

Colley (1980) first resolved W3 (C) into clumpy and ring-like radio sources at 2.7 and 15.4 GHz and measured the luminosity and diameter of W3 (C) as $4.2 \times 10^4 L_\odot$ and $7''$ respectively. Ladd et al. (1993) have suggested that W3 IRS 4 has 3 individual luminosity sources. The southern part of W3 comprises of the two separated regions W3 J and K. W3 J is superimposed on the large ring-like (with a low brightness) HII region also known as G133.7+1.1 extending to the southern regions of W3 (Roelfsema et al. 1987).

G133.6945+01.2 after imaging vividly shows an HII region (see Figure 3.1). We do not detect the YSO (at RA: 02:25:31.22 DEC: 62:06:21.00). A non-detection of the YSO is obviously due to the vast amount of emission from the HII region and perhaps the YSO is still very young and embedded in its parental envelope.

a) Detected HII region b) Radio contour map

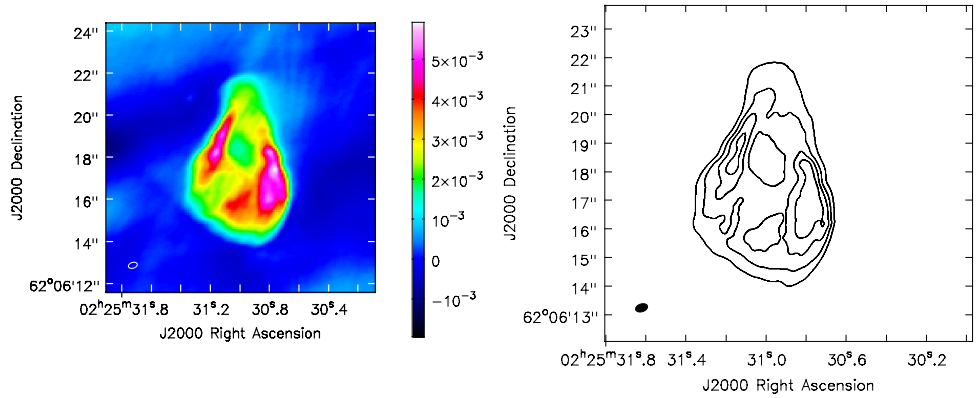


Figure 3.1 | **G133.6950+01.2151 radio image.** a) is an image of the detected HII region (VLA G133.6950+01.2151). b) is a radio contour image of the detected HII region. Contour levels are 0.2, 0.4, 0.6 and 0.8 percent of the maximum flux of 5.94 mJy. NB: The synthesized beam is indicated in the bottom-left corner of each image.

| Region | RA | Dec | Int. flux (mJy) | Peak flux (mJy/beam) |
|---|---|---|---|---|
| 1 | 02:25:30.96 ±0.01 | 62.06.17.29 ±0.09 | 0.87 ±0.03 | 4.60 ±0.16 |

Table 3.1 | **Measured parameters: detected HII region.** Here, the measured coordinates and flux of the detect HII region (region 1) is shown. The integrated and peak fluxes were obtained by fitting a Gaussian to the detected source.

### 3.1.2 G075.7822+00.3 (G75.78+0.34)

The image of G075.7822+00.3 revealed 3 sources labelled E, F and $G075_{YSO}$ (see Figure 3.2). The flux values and positions are presented in Table 3.2. E appears to be a hot molecular core (the presence of this core has been predicted by Beuther et al. 2018) and associated with the YSO. It is not clear if source F has any association with the YSO.

| Region | RA | Dec | Int. flux (mJy) | Peak flux (mJy/beam) |
|---|---|---|---|---|
| E | 20:21:44.09 ±0.01 | 37.26.39.46 ±0.03 | 17.2 ±1.30 | 2.84 ±0.19 |
| F | 20:21:44.49 ±0.01 | 37.26.37.74 ±0.01 | 1.75 ±0.07 | 1.61±0.03 |
| $G075_{YSO}$ | 20:21:44.02 ±0.01 | 37.26.37.57 ±0.01 | 0.77 ±0.05 | 0.62±0.02 |

Table 3.2 | **G075.7822+00.3 measured parameters.** Here, the measured coordinates and fluxes of regions E, F and $G075_{YSO}$ (our YSO) are presented.

a) Detected sources b) G075.7822+00.3 zoomed-in

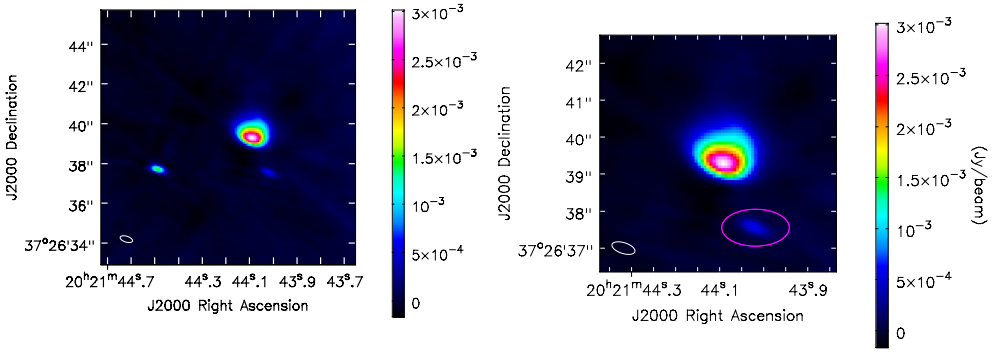


Figure 3.2 | **G075.7822+00.3 radio image.** a) Image showing G075.7822+00.3 with all the detected sources in the field. b) G075.7822+00.3 zoomed-in to show YSO (magenta ellipse in image). NB: The color bar indicates the peak flux scale. The synthesized beam is indicated in the bottom-left corner of each image.

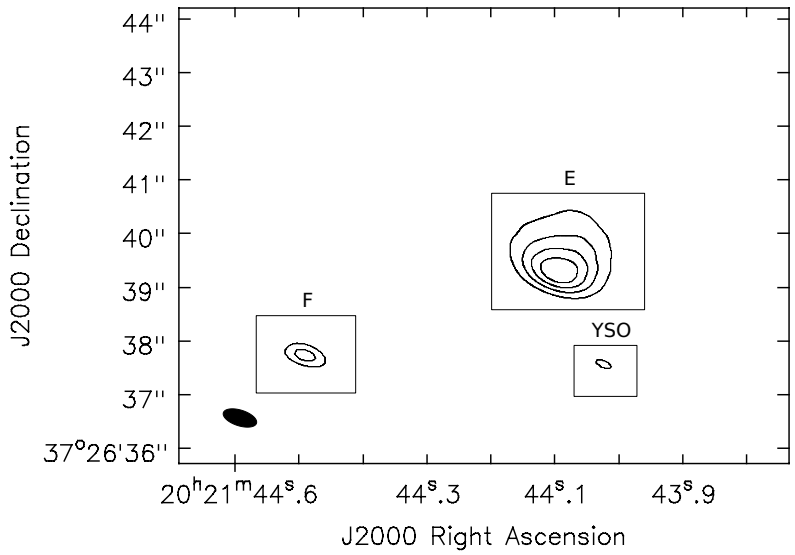


Figure 3.3 | **Radio contour: G075.7822+00.3.** A radio contour map of G075.7822+00.3 showing all detected sources E, F and the YSO. Contour levels are 0.2, 0.4, 0.6 and 0.8 percent of the maximum flux of 3.02 mJy. NB: The synthesized beam is indicated in the bottom-left corner of image.

### 3.1.3 G078.8867+00.7 (AFGL2591)

G078.8867+00.7087 is a jet, which has one side. For this target, we look for radio jet emission westward of an outflow present in the field. When seen in optical and near-IR, there is evidence of a shock phenomenon as shown by Hasegawa and Mitchell (1995).

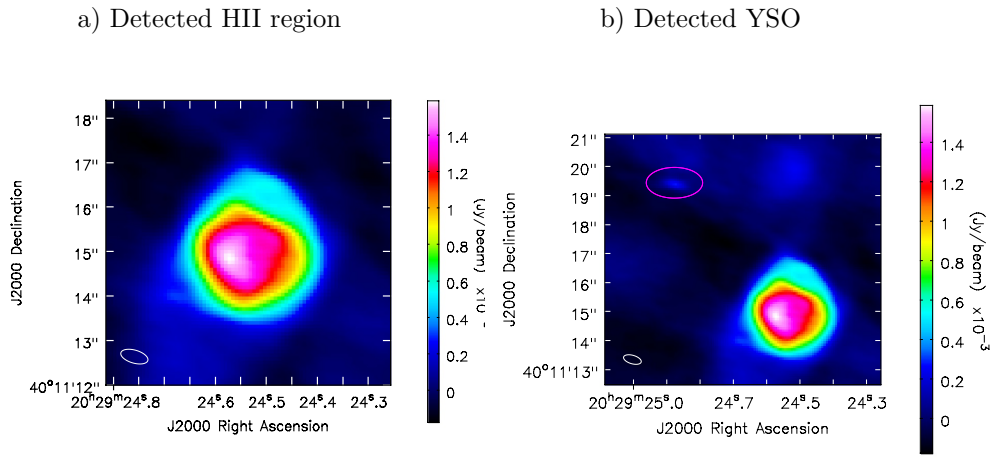


Figure 3.4 | **G078.8867+00.7 radio image.** a) Image showing the detected HII region in G078.8867+00.7. b) Image showing the YSO ($G078_{YSO}$) in field (magenta ellipse in image). NB: The color bar indicates the peak flux scale. The synthesized beam is indicated in the bottom-left corner of each image.

| Region | RA | Dec | Int. flux (mJy) | Peak flux (mJy/beam) |
|---|---|---|---|---|
| 1 | 20:29:24.54 ±0.00 | 40.11.14.91 ±0.02 | 47.4 ±1.10 | 1.68 ±0.04 |
| 2 | 20:29:24.52 ±0.02 | 40.11.19.89 ±0.02 | 4.79 ±0.14 | 0.27 ±0.01 |
| $G078_{YSO}$ | 20:29:24.87 ±0.00 | 40.11.19.42 ±0.01 | 0.40 ±0.01 | 0.30 ±0.01 |

Table 3.3 | **G078.8867+00.7 measured parameters.** The measured coordinates and fluxes of the detected sources in G078.8867+00.7 are shown here.

The HII region in G078.8867+00.7 is fully resolved and has an integrated flux of 47.40 ±1.10 mJy, further details are shown in Table 3.3. Here, we see an indication of a hot molecular core (this has been suggested by Beuther et al. 2018). The YSO ($G078_{YSO}$) in this field is detected as shown with a magenta ellipse in Figure 3.4 b. $G078_{YSO}$ (G078.8867+00.7) is known to be a jet with a lobe (Purser et al. 2021).

A previous study on G078.8867+00.7 at 5 GHz by Urquhart et al. (2009) reports an integrated and peak flux values of 4.40 mJy and 2.10 mJy beam$^{-1}$ respectively. Comparing the measured flux values reveals a decrease, this suggests that this source may be exhibiting variability.

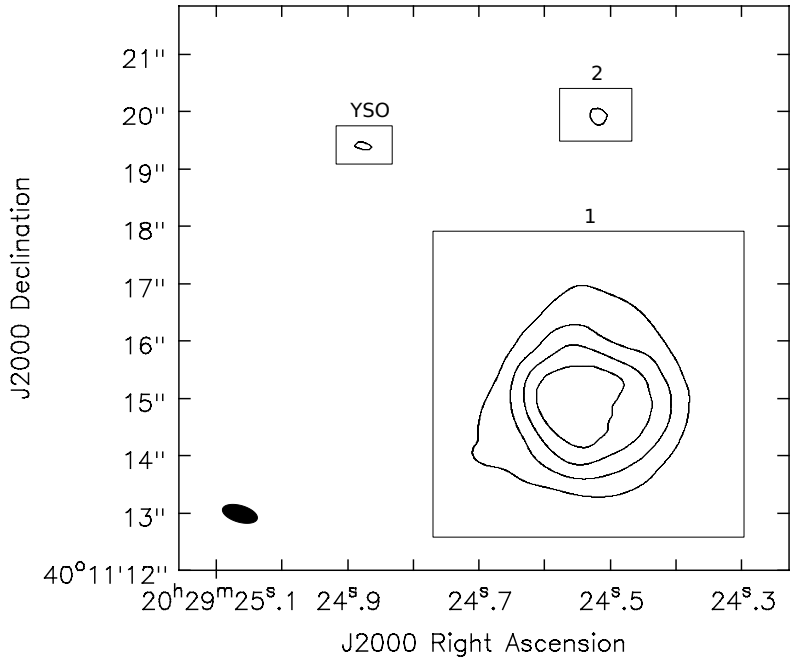


Figure 3.5 | **Radio contour: G078.8867+00.7.** A radio contour map of G078.8867+00.7 showing all detected sources. Contour levels are 0.2, 0.4, 0.6 and 0.8 percent of the maximum flux of 1.59 mJy. The synthesized beam is indicated in the bottom-left corner of image.

### 3.1.4 IRAS 21078+5211 (G092.69+3.08)

a) IRAS 21078+5211 b) IRAS 21078+5211 close-up

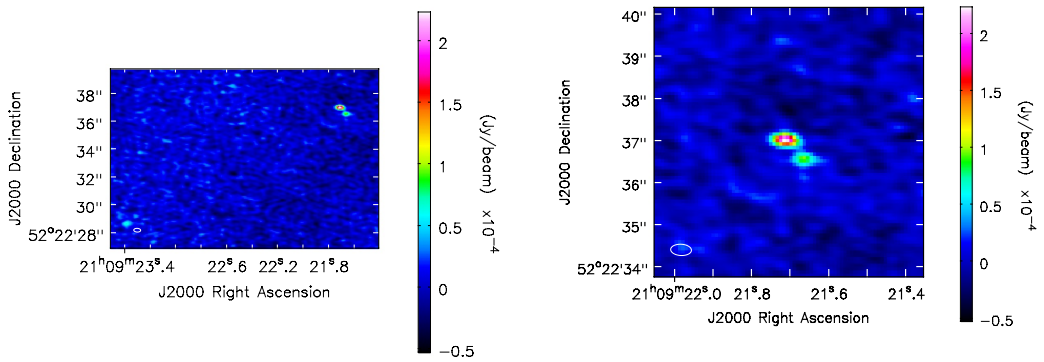


Figure 3.6 | **IRAS 21078+5211 radio image.** a) A wide-field image of IRAS 21078+5211 showing all sources present. b) A zoomed-in view of IRAS 21078+5211 showing the strong source in field. NB: Shown on the right-side of both images is a color bar indicating the peak flux scale. The synthesized beam is indicated in the bottom-left corner of each image.

For IRAS 21078+5211, we detect 3 sources G (G1 and G2) and H as shown in Figure 3.6. The

a) Radio contour: IRAS 21078+5211 b) Radio contour: close-up

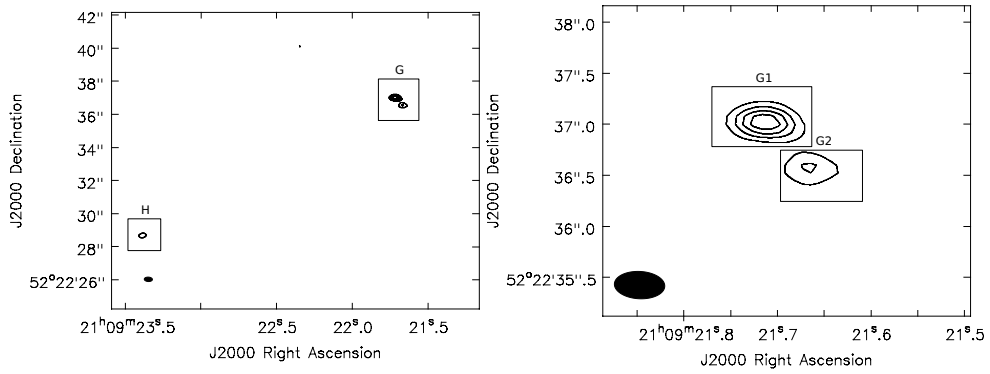


Figure 3.7 | **IRAS 21078+5211 radio contour.** a) A wide-field radio contour map of IRAS 21078+5211 indicating all detected sources (G and H). Contour levels are -0.2, 0.2, 0.4, 0.6 and 0.8 percent of the maximum flux of 0.22 mJy. b) A close-view radio contour image of region G, showing detected sources G1 and G2. Contour levels are -0.2, 0.2, 0.4, 0.6 and 0.8 percent of the maximum flux of 0.22 mJy. NB: The synthesized beam is indicated in the bottom-left corner of each image.

positions and fluxes of all the detected sources are presented in Table 3.4. Clearly, sources G1 and G2 are associated. Detected sources G2 and H all have the same integrated and peak flux values.

We detect the YSO, found in region G as seen in Figure 3.7. Specifically the YSO is labelled as source G1. Similarly, at 6 and 22 GHz (using JVLA), Moscadelli et al. (2016) detects two sources associated with IRAS 21078+5211 named VLA 1 (associated compact source) and VLA 2, which are our detected sources G1 and G2 respectively. Moscadelli et al. (2016) reported integrated and peak flux values of 0.32 $\pm$0.05 and 0.07 $\pm$0.01 mJy beam$^{-1}$ for VLA 2. Aside VLA 1 and VLA 2, Moscadelli et al. (2016) also detected a synchrotron emission in the field, which they associate with VLA 2.

Beuther et al. (2018) discusses IRAS 21078+5211 as a very fragmented cluster (with a size of about 0.1pc) of molecular cores located at the density peak of a 1pc elongated molecular cloud. Looking at the separation (less than 0.2 arcseconds) between our two detected sources G1 and G2, there may be an indication of fragmentation as seen in our radio image (see Figure 3.6).

| Region | RA | Dec | Int. flux (mJy) | Peak flux (mJy/beam) |
|---|---|---|---|---|
| G1 | 21:09:21.71 ±0.01 | 52.22.37.02 ±0.01 | 0.26 ±0.02 | 0.23 ±0.01 |
| G2 | 21:09:21.66 ±0.01 | 52.22.36.56 ±0.01 | 0.10 ±0.01 | 0.10 ±0.01 |
| H | 21:09:23.38 ±0.01 | 52.22.28.68 ±0.02 | 0.10 ±0.01 | 0.10±0.01 |

Table 3.4 | **IRAS 21078+5211 measured parameters.** The measured coordinates and fluxes of all the detected sources in IRAS 21078+5211 are shown here.

### 3.1.5 G109.8715+02.1 (CepA HW2)

G109.8715+0.2.1156 have been studied by Curiel et al. (2006) and Cunningham et al. (2009) and is believed to host a jet and disc. These studies have also suggested the presence of shocked molecular hydrogen structures in the field (Cunningham et al. 2009).

a) G109.8715+02.1 (CepA HW2) b) G109.8715+02.1 radio contour

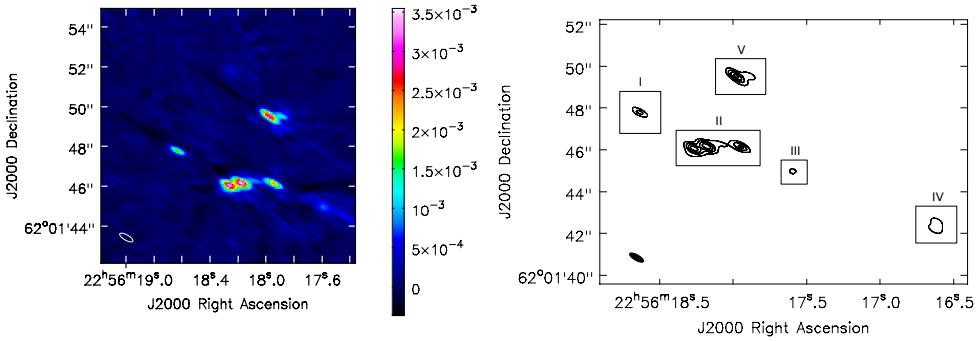


Figure 3.8 | **G109.8715+02.1 radio image.** a) A wide-field image of G109.8715+02.1 showing all detected sources. b) A radio contour map of G109.8715+02.1 showing all 5 detected sources labelled I to V (measured values of these sources are presented in Table 3.5). Contour levels are 0.2, 0.4, 0.6 and 0.8 percent of the maximum flux of 3.55 mJy. NB: The color bar indicates the peak flux scale. The synthesized beam is indicated in the bottom-left corner of each image.

| Region | RA | Dec | Int. flux (mJy) | Peak flux (mJy/beam) |
|---|---|---|---|---|
| I | 22:56:18.63 ±0.01 | 62.01.47.80 ±0.01 | 1.63 ±0.12 | 1.75 ±0.06 |
| II | 22:56:18.21 ±0.01 | 62.01.46.13 ±0.02 | 9.10 ±1.40 | 3.02±0.35 |
| III | 22:56:17.59 ±0.01 | 62.01.45.13 ±0.03 | 1.90 ±0.24 | 0.67±0.01 |
| IV | 22:56:16.61 ±0.01 | 62.01.42.38 ±0.03 | 4.18 ±0.36 | 0.87±0.01 |
| V | 22:56:17.97 ±0.01 | 62.01.49.52 ±0.02 | 3.80 ±0.43 | 2.83±0.18 |

Table 3.5 | **G109.8715+02.1 measured parameters.** The measured coordinates and fluxes of all the detected sources in G109.8715+02.1 are shown here.

Our imaging revealed up to 5 cores. Beuther et al. (2018), discusses G109.8715+02.1 as a

a) Radio contour: detected source YSO b) Radio contour: detected source

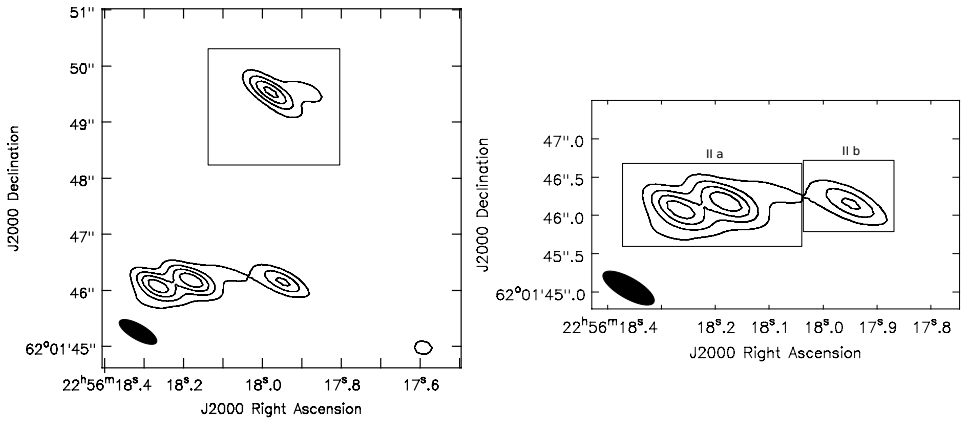


Figure 3.9 | **G109.8715+02.1 radio contour.** a) A radio contour map of G109.8715+02.1 showing the position of the YSO; region V (black rectangle). Contour levels are 0.2, 0.4, 0.6 and 0.8 percent of the maximum flux of 3.55 mJy. b) A radio contour map of G109.8715+02.1 showing source II split into two sources; II a and II b. Contour levels are 0.2, 0.4, 0.6 and 0.8 percent of the maximum flux of 3.55 mJy. NB: The synthesized beam is indicated in the bottom-left corner of each image.

highly fragmented source which is seen in our image (see Figure 3.8). Our images clearly show evidence of hot molecular cores and association with a jet (Beuther et al. 2018 and Purser et al. 2021). The brightest source in the field is source II (integrated flux of 9.10 ±1.40 mJy). Our target source is V (appears extended as seen in Figure 3.9), which has an integrated flux of 3.80 ±0.43 mJy. Further details are shown in Table 3.5. To investigate any possible variability in G109.8715+02.1, we compare previous VLA observations (shown in Table 3.6). Table 3.6 shows an indication of variability in G109.8715+02.1 (source V).

The YSO has also been studied at 23 and 8.3 GHz by Curiel et al. (2006). From this study, they record fluxes of 40.00 and 7.00 mJy respectively at the said frequency for G109.8715+02.1.

| Wavelength λ (cm) | Flux density (mJy) | Date | Type of observation |
|---|---|---|---|
| 3.6 | 0.57 | Jul 1991 | VLA |
| 3.6 | 1.6 | Jul 1999 | VLA |
| 3.6 | 2.76 | Dec 2000 | VLA |
| 3.6 | 2.41 | Feb 2002 | VLA/Pie Town link |
| 1.3 | 3.60 | Jul 1995 | VLA |
| 1.3 | 1.37 | Jul 1999 | VLA |
| 1.3 | 0.68 | Apr 2002 | VLA |
| 1.3 | 3.60 | Oct 2004 | VLA |
| 0.7 | 0.47 | Dec 1996 | VLA |
| 5 | 3.80 | May 2018 | VLA |

Table 3.6 | **History of CepA HW2 observations.** Presented here are the past and present records of CepA HW2 observations showing the observation wavelength, date, measured flux density, type and configuration. All these observations were performed in VLA's configuration A. References: July 1991 and Dec 1996 by Curiel et al. (2003), July 1995 by Torrelles et al. (1996), Jul 1999, Feb and Apr 2002 by Curiel et al. (2006), Oct 2004 by Patel et al. (2005) and May 2018 denote this work.

To compare the integrated fluxes of the various sources detected in G109.8715+02.1, we present Table 3.7 below. Here, we observe that the fluxes of the detected sources are fairly similar with the exception of source II, which has the highest integrated flux.

| Region | Int. flux (mJy) |
|---|---|
| I | 1.63 ±0.12 |
| II | 9.10 ±1.40 |
| III | 1.90 ±0.24 |
| IV | 4.18 ±0.36 |
| V | 3.80 ±0.43 |

Table 3.7 | **Comparing detected sources in G109.8715+02.1.** Shown in this table are the fluxes of the various detected sources (regions I-V) in G109.8715+02.1.

### 3.1.6 NGC 7538S (G111.5320+00.7593)

Our results reveals a jet being driven by a core. Also, lobes are vivid in our radio image (Figure 3.10). This lobe extends a few arcseconds away from the core. We measured integrated and peak fluxes of 0.39 ±0.03 mJy and 0.20 ±0.01 mJy beam$^{-1}$ for this YSO (source A). The left-side and right-side jet-like structures have fluxes of 0.35 and 0.38 mJy. We present the positions and fluxes of other detected sources in the field in Table 3.8.

a) NGC 7538S b) NGC 7538S radio contour

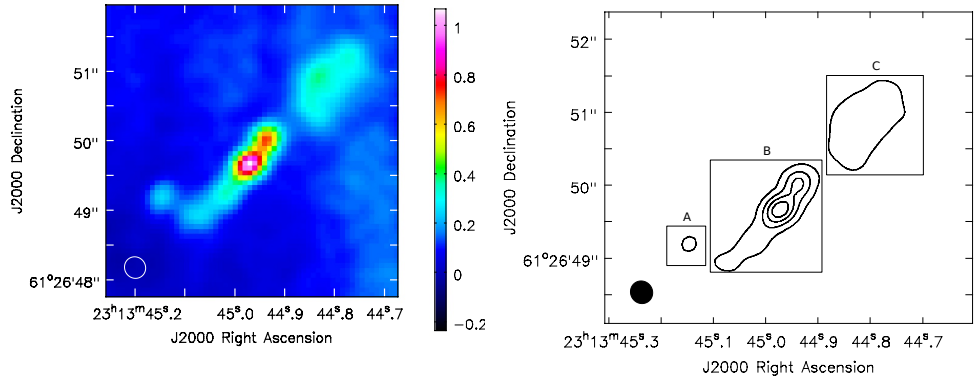


Figure 3.10 | **NGC 7538S radio image.** a) Image of NGC 7538S showing outflow or jet regions: left-side and right-side with fluxes of 0.35 and 0.38 mJy. NB: These fluxes were taken by tracing the outline (in CASA viewer) of the left- and right-side area of the jet and recording the associated maximum flux values. The color bar indicates the peak flux scale. b) A wide-field radio contour map of NGC 7538S showing all detected sources (A, B and C). The measured values of these sources are presented in Table 3.8. Contour levels are -0.2, 0.2, 0.4, 0.6 and 0.8 percent of the maximum flux of 1.07mJy. NB: The synthesized beam is indicated in the bottom-left corner of each image.

| Region | RA | Dec | Int. flux (mJy) | Peak flux (mJy/beam) |
|---|---|---|---|---|
| A | 23:13:45.14 ±0.00 | 61.26.49.18 ±0.01 | 0.39 ±0.03 | 0.20 ±0.01 |
| B | 23:13:44.96 ±0.00 | 61.26.49.74 ±0.02 | 2.49 ±0.20 | 0.81 ±0.01 |
| C | 23:13:44.81 ±0.00 | 61.26.50.87 ±0.03 | 1.98 ±0.16 | 0.23 ±0.02 |

Table 3.8 | **NGC 7538S measured parameters.** A Table showing the measured positions, integrated and peak fluxes corresponding to the detected contour regions in NGC 7538S.

### 3.1.7 NGC 7538IRS1 (G111.5423+00.7776)

In this field, we detect our YSO (region M), alongside another source N (see Figure 3.11). The details of all the detected sources in the field in Table 3.9. The YSO has a characteristic compact and cometry structure as seen in our radio image (see Figure 3.11 b).

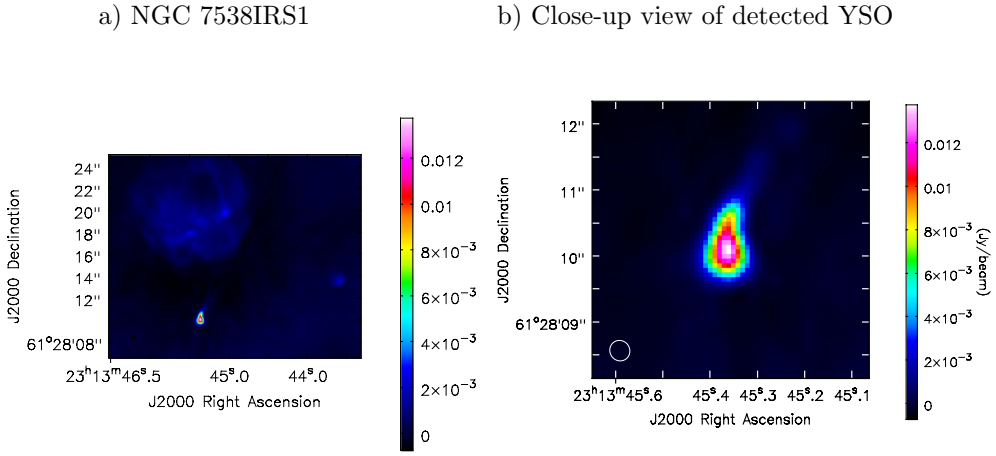


Figure 3.11 | **NGC 7538IRS1 radio image.** a) A wide-field image of NGC 7538IRS1 showing the detected sources. b) A zoomed-in image of the detected strong source (our YSO) in NGC 7538IRS1. NB: The color bar indicates the peak flux scale. The synthesized beam is indicated in the bottom-left corner of each image.

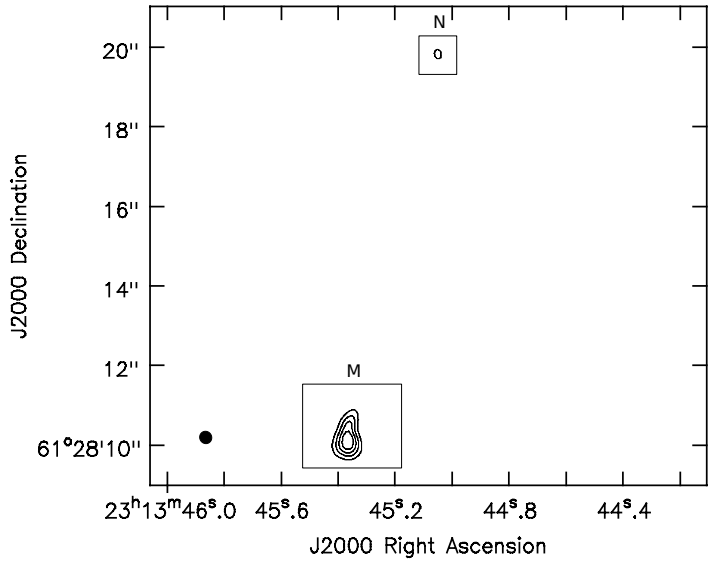


Figure 3.12 | **Radio contour: NGC 7538IRS1.** A wide-field radio contour map of NGC 7538IRS1 indicating the 2 detected sources M and N. The synthesized beam is indicated in the bottom-left corner of the image. The measured values of these sources are presented in Table 3.9. Contour levels are 0.2, 0.4, 0.6 and 0.8 percent of the maximum flux of 13.77 mJy.

| Region | RA | Dec | Int. flux (mJy) | Peak flux (mJy/beam) |
|---|---|---|---|---|
| M | 23:13:45.36 ±0.00 | 61.28.10.16 ±0.02 | 56.0 ±3.90 | 14.12 ±0.80 |
| N | 23:13:45.05 ±0.00 | 61.28.19.84 ±0.02 | 15.3 ±1.00 | 2.08 ±0.13 |

Table 3.9 | **NGC 7538IRS1 measured parameters.** The Table shows the measured coordinates and fluxes of the 2 detected sources M and N.

### 3.1.8 IRAS 23385+6053

Molinari et al. (2002) have studied IRAS 23385+6053 (Mol 160) at 3.6 cm and detected 2 sources VLA (Mol 160) 1 and 2 (all classified as extended sources) and reports an integrated flux of approximately 80 and 20 mJy for the 2 sources respectively, all based on a VLA observation made between 6th and 28th February 1999 in the D and C configuration respectively. Surprisingly, these sources were not detected in their previous VLA study in 1998 at 15 and 5 GHz (Molinari et al. 1998a and Molinari et al. 1998b). This non-detection was attributed to the type of configuration used for the observation (configuration B).

a) IRAS 23385+6053 b) Close-up view of detected YSO

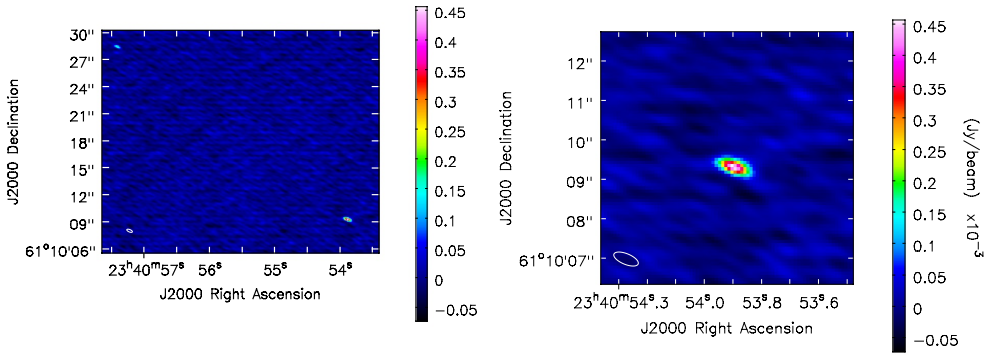


Figure 3.13 | **IRAS 23385+6053 radio image.** a) A wide-field image of IRAS 23385+6053 showing 2 detected sources, with a color bar indicating the peak flux, one in the top-left corner and the other in the bottom-right corner. b) A zoomed-in image of the brightest source in the field. NB: The color bar indicates the peak flux scale. The synthesized beam is indicated in the bottom-left corner of each image.

In this work, we detected 2 sources Q and R (YSO or the radio point source, see Figure 3.13). For our YSO, we measured integrated and peak fluxes of 0.50 mJy and 0.15 mJy beam$^{-1}$ respectively as seen in Table 3.10. Our weak emission from the detected YSO may support the claim by Cesaroni et al. (2019) that this YSO is the youngest amongst the entire CORE sample

a) Radio contour of IRAS 23385+6053 b) Close-up view of detected source

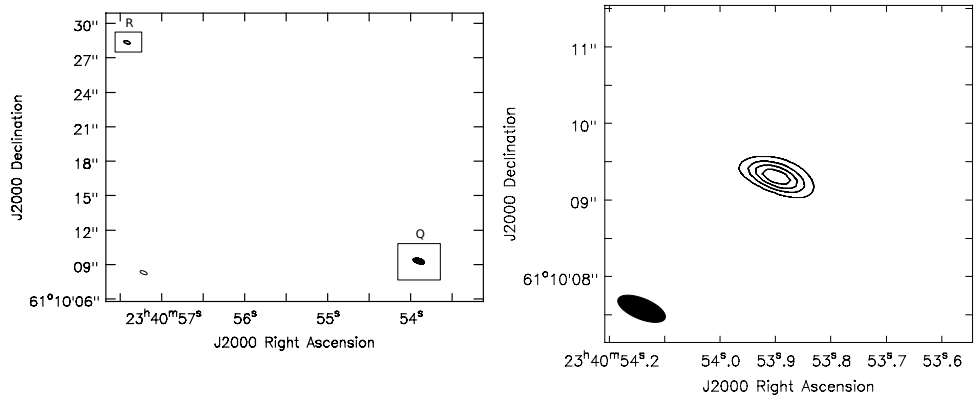


Figure 3.14 | **IRAS 23385+6053 radio contour.** a) A wide-field radio contour map of IRAS 23385+6053 indicating the 2 detected sources Q and R. b) A zoomed-in radio contour map showing detected source Q. NB: The measured values of these sources are presented in Table 3.10. Contour levels are 0.2, 0.4, 0.6 and 0.8 percent of the maximum flux of 0.46 mJy. The synthesized beam is indicated in the bottom-left corner of each image.

and is still forming.

| Region | RA | Dec | Int. flux (mJy) | Peak flux (mJy/beam) |
|---|---|---|---|---|
| Q | 23:40:53.90 ±0.01 | 61.10.09.31 ±0.01 | 0.50 ±0.01 | 0.47 ±0.01 |
| R | 23:40:57.41 ±0.01 | 61.10.28.40 ±0.01 | 0.19 ±0.02 | 0.18 ±0.01 |

Table 3.10 | **IRAS 23385+6053 measured parameters.** The table shows the measured coordinates and fluxes of the 2 detected sources in IRAS 23385+6053.

## 3.2 Summary: 18A-104 observations and YSO detections

Most of the targets are dominated by single, double or triple sources except G109.8715+02.1, which shows a complex field with 5 main sources. Furthermore, most of the imaged targets were resolved. For example G078.8867+00.7 and G075.7822+00.3 both show a compact source, G133.6945+01.2 is an HII region, NGC 7538S is seen as a jet with lobes and NGC 7538IRS1 has a cometry-like structure. Additionally, IRAS 21078+5211 and IRAS 23385+6053 appear as point-like sources. Note that all the detected YSOs are all described as radio point sources (RPSs).

Table 3.11 shows a summary of our observations (at 6 GHz) and YSOs detected together with their right ascension (RA) and declination (DEC). For all the 8 targets, we detected the

associated YSOs or radio point sources in all the fields (targets indicated with a 'Y' under the column named 'Detection' in Table 3.11 below) expect for G133.6945+01.2 (indicated with an 'N' under the column named 'Detection' in Table 3.11).

| 18A Sample name | RA(J2000) | Dec(J2000) | Detection |
|---|---|---|---|
| G133.6945+01.2 | 02:25:31.22 | +62:06:21.00 | N |
| G075.7822+00.3 | 20:21:44.03 | +3726:37.70 | Y |
| G078.8867+00.7 | 20:29:24.86 | +40:11:19.40 | Y |
| IRAS 21078+5211 | 21:09:21.64 | +52:22:37.50 | Y |
| G109.8715+02.1 | 22:56:17.98 | +62:01:49.50 | Y |
| IRAS 23385+6053 | 23:40:54.40 | +61:10:28.20 | Y |
| NGC 7538S | 23:13:44.86 | +61:26:48.10 | Y |
| NGC 7538IRS1 | 23:13:45.36 | +61:28:10.55 | Y |

Table 3.11 | **18A-104 detections summary.** We present a summary of our detections with their associated right ascension (RA) and declination (DEC). **Note**: Y = detected and N = not detected.

## 3.3 Radio luminosities

To analyse our target fields in radio and bolometric luminosity parameter space, we compute the radio luminosity using Equation 3.1 below:

$$S_{6GHzD^2} = S_{6GHz} \times D^2 \tag{3.1}$$

Where $S_{6GHzD^2}$ is the radio distance luminosity (radio luminosity), $S_{6GHz}$ is the measured or estimated integrated fluxes of our targets and D is the distance to targets in kilo parsec (kpc) units.

In the following sections, we investigate the behaviour of our sample in radio luminosity parameter space with respect to parameters such as luminosity (note that in all our discussion, luminosity means bolometric luminosity), sample and core masses and parental core-luminosity-to-mass ratio. Luminosity, sample and core masses values for each plot were obtained from Beuther et al. (2018). We offer further discussion on what we mean by 'sample and core' masses in Section 3.3. Also, Table A.1 in the appendix shows the computed radio luminosities and parental core-luminosity-to-mass ratio values used for the associated plots.

**Radio luminosity against luminosity: high and low-mass fits**

One of the significant results from both studies of Purser et al. (2016) and Purser et al. (2021) on young massive stars or massive young stellar objects (especially those with jets) is the differentiation of HII regions from relatively young stellar objects in terms of radio and bolometric luminosity parameter space.

One problem with trying to compute the radio luminosities for winds and ionized jets related to young massive stars is the inadequacy of theoretical models that characterize the key parameters that affect the radio luminosities of these ionized jets. Fortunately, we can use the observational relation (Equation 3.2 shown below) derived by Anglada (1995) for the radio luminosity against bolometric luminosity for low-mass stars (with peak luminosities of approximately 500 $L_{\odot}$) as a scale to compare with young massive stars especially for those with jets and outflows.

$$S_{v}D^{2} \approx 10^{-2.1}L_{bol}^{0.6} \tag{3.2}$$

Where $S_{v}$ is flux measured in mJy, D is the distance in kpc units and $L_{bol}$ is the bolometric luminosity in $L_{\odot}$ units.

Using this relation (Equation 3.2) for young massive stars (for example the CORE targets) would mean that if we assume that the phenomenon behind the production of jet and ionization for low-mass cases are not the same for these objects, then we would see a divergence towards massive young stellar objects. In other words, massive young stellar objects (especially those with jets) will seclude themselves from the other objects such as HII regions and low-mass stars (this has been shown by Purser et al. 2016, Obonyo 2020 and Purser et al. 2021).

For these CORE targets, we investigate this segregation phenomenon. To investigate the predicted seclusion of young massive stars (especially those with jets) from low-mass stars and HII regions, we over-plot the power law derived for low-mass and high-mass cases by Purser et al. (2021) to our 20 CORE targets except for G133.6945+01.2, which we do not detect and does not have any associated integrated flux at radio wavelengths, hence the corresponding radio luminosities could not be estimated.

Figure 3.15 show that the radio luminosities of our 20 targets (massive young stars) scales with their corresponding bolometric luminosities. Furthermore, Figure 3.15 shows the predicted

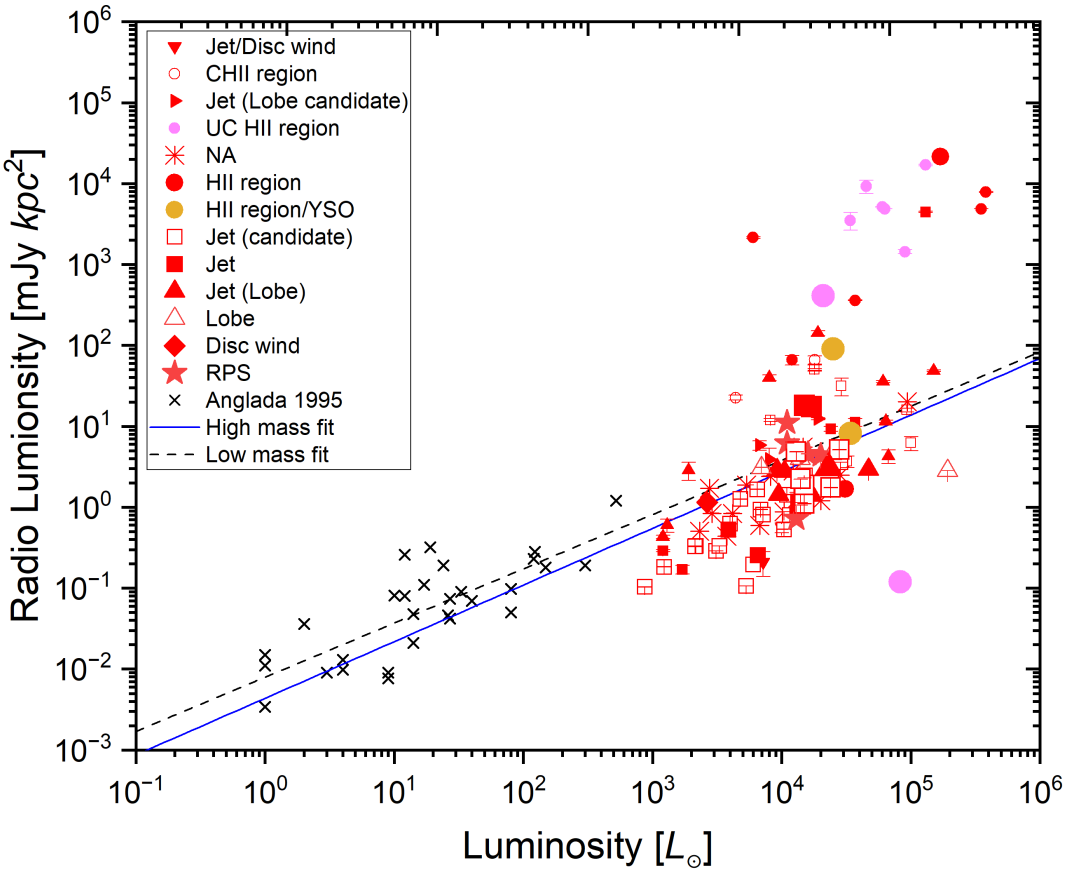


Figure 3.15 | **Radio luminosity against luminosity: high and low-mass fit.** A plot of the radio luminosity against bolometric luminosity for the entire 20 CORE targets over-plotted with the power law derived for low-mass and high-mass cases (Purser et al. 2021) and data points from Anglada (1995), Purser et al. (2016) and Purser et al. (2021). The high and low-mass fits are denoted as blue and black dashed lines on the plot. The different sub-classifications are marked as follows: red triangle inverted for Jet/disc wind, hollow circle for compact HII region, red triangle-left pointing for jet lobe candidate, blue circle for ultra-compact HII region, asterisk for not classified, red circle for HII region, orange circle for HII region/YSO, hollow square for jet candidate, red square for jet, red triangle for jet lobe, hollow triangle for lobe, red diamond for disc wind and red star for radio point source (RPS). Objects from this work (CORE targets) are shown as the largest marker size while the smaller marker size denotes targets from Purser et al. (2016) and Purser et al. (2021). Crosses represent low-mass stars from Anglada (1995). See Table 3.14 for details for all our target classifications. **Notes**: Luminosity values for all our targets are obtained from Beuther et al. (2018). 1 (W3 IRAS 4) out of the 20 CORE targets do not have any previously measured or estimated integrated flux hence its radio luminosity could not be computed. Associated errors are shown with error bars for all data points on the plot except for those that belong to Anglada (1995). Also, points that appear without error bars are smaller than the point size.

seclusion of our sample of massive young stellar objects from the low-mass region of the plot. To compare with results from other studies, thus in terms of the plotted high and low-mass fits deduced by Purser et al. (2021) as seen in Figure 3.15, we observe that our 8 targets (18A-104) and the 12 other CORE targets, follow the predicted divergence of young massive stars (especially those with jets) from low-mass stars which indicate that radio luminosities of the CORE targets (young massive stars) scales with bolometric luminosity as shown by other studies such as Purser et al. (2016), Obonyo (2020) and Purser et al. (2021). This result points to the fact that young massive stars are likely to be formed through a scaled up version of their low-mass counterparts.

To inspect the accuracy of the correlation on our plots (Figures 3.16, 3.17, 3.19 and 3.18) we fit a line using the equation $y = a + b * x$ and use Pearson's correlation coefficient or Pearson's r to analyse the fit. Pearson's correlation coefficient gives the quality of a least squares fitting with respect to our data-set (Pearson 1895). In general, Pearson's correlation coefficient between 0 and 1 indicate a positive correlation (specifically, a Pearson's r value of greater than 0.5 is a strong correlation, between 0.3 and 0.5 is moderate correlation and between 0 and 0.3 for weak correlation), 0 no correlation and between 0 and -1 for negative correlations.

| (x,y) | Pearson's r |
|---|---|
| Sample mass vs Radio Luminosity | 0.38 |
| Core mass vs Radio Luminosity | 0.07 |
| Core mass vs Sample mass | 0.43 |
| Luminosity-to-mass ratio vs Radio Luminosity | 0.14 |

Table 3.12 | **Correlation fits.** A summary of the values of Pearson's correlation coefficient for plots or Figures 3.16, 3.17, 3.19 and 3.18.

**Radio luminosity against sample masses**

We define 'sample mass' as the global mass of the YSO which were computed mostly from SCUBA 850 μm fluxes, 1.2 mm continuum data, 1.1 mm continuum data and based on $C^{18}O$(3–2) data (Beuther et al. 2002, Di Francesco et al. 2008, Ginsburg et al. 2013 and Maud et al. 2015). In Figure 3.16 below, we plot the radio luminosities of the entire CORE targets (except for W3 IRAS 4 which do not have any previously measured or estimated integrated flux hence its radio luminosity could not be computed) against their corresponding sample masses. A classification of the various targets as jets, jet candidate, jet lobes, HII region, HII region/YSO and radio point source (RPS) are also shown on plot. Also, the correlation fit (represented as

a black line) is shown on the plot.

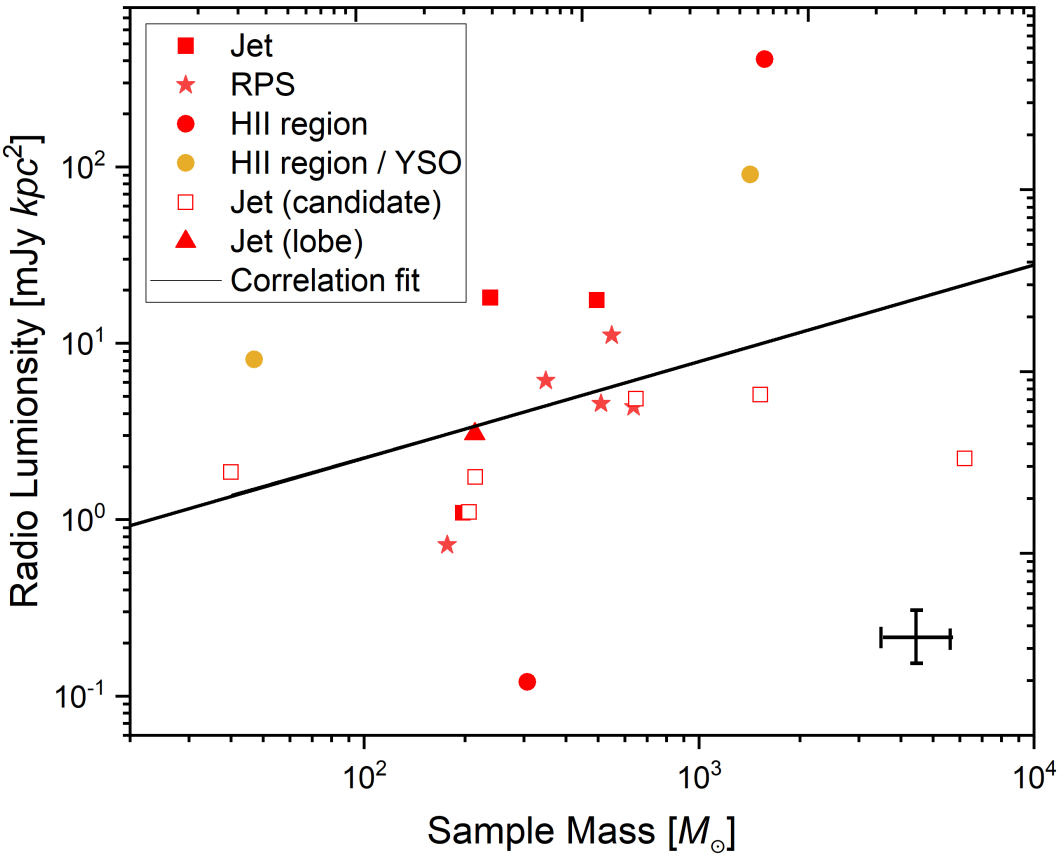


Figure 3.16 | **Radio luminosities against sample masses.** Radio luminosities of the entire CORE targets against the sample masses. The legend on the graph provides a brief description of our targets thus same as the classification used in Figure 3.15. See Table 3.14 for details of the classification. The correlation fit is represented as a black line on the plot. **Notes**: Masses are obtained from Beuther et al. (2018) thus, masses calculated mostly from SCUBA 850 μm fluxes, 1.2 mm continuum data, 1.1 mm continuum data and based on $C^{18}O(3-2)$ data (Beuther et al. 2002, Di Francesco et al. 2008, Ginsburg et al. 2013 and Maud et al. 2015). 1 (W3 IRAS 4) out of the 20 CORE targets do not have any previously measured or estimated integrated flux hence its radio luminosity could not be computed. Typical error bars are shown in the bottom right corner of plot.

### Radio luminosity against core masses

Similar to the above section, we compare the computed radio luminosities and core masses of our targets. The core masses are the masses associated with the cores of the detected YSOs at millimetre wavelength (Beuther et al. 2018). Note that these core masses are lower limit mass estimates (Beuther et al. 2018). In Figure 3.17 below, we plot the radio luminosities of the entire CORE targets (except for W3 IRAS 4 which do not have any previously measured or estimated integrated flux hence its radio luminosity could not be computed) against their corresponding core masses. A classification of the various targets as jets, jet candidate, jet lobes, HII region, HII region/YSO and radio point source (RPS) are also shown on plot. Also, the correlation fit (represented as a black line) is shown on the plot.

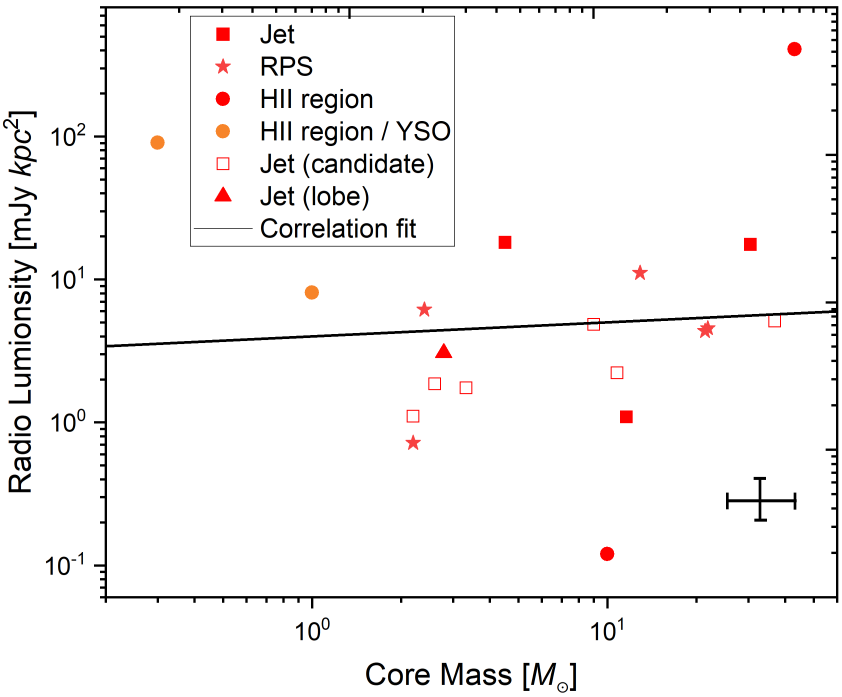


Figure 3.17 | **Radio luminosities against core masses.** Radio luminosities of the entire CORE sample against their core masses (these are the masses associated with the cores of the detected YSOs at millimetre wavelength obtained from Beuther et al. 2018). The legend on the graph provides a brief description of our targets thus same as the classification used in Figure 3.15. See Table 3.14 for details of the classification. The correlation fit is represented as a black line on the plot. **Notes**: Masses are obtained from Beuther et al. (2018) thus; masses calculated mostly from SCUBA 850 μm fluxes, 1.2 mm continuum data, 1.1mm continuum data and based on $C^{18}O(3-2)$ data (Beuther et al. 2002, Di Francesco et al. 2008, Ginsburg et al. 2013 and Maud et al. 2015). 1 (W3 IRAS 4) out of the 20 CORE targets does not have any previously measured or estimated integrated flux hence its radio luminosity could not be computed. Typical error bars are shown in the bottom right corner of plot.

For both Figures 3.16 and 3.17, we see an indication of a correlation (see Table 3.12 for correlation values) between both sample and core masses with radio luminosity. There is a stronger correlation for the radio luminosities against sample masses (with a Pearson's correlation coefficient value of 0.38) compared to that of the radio luminosities against core masses (with a Pearson's correlation coefficient value of 0.07). The strong correlation for the radio luminosities against sample mass indicate that large sample masses tend to be more radio luminous.

**Radio luminosity against parental core-luminosity-to-mass ratio**

A plot of the radio luminosity against parental core-luminosity-to-mass ratio can give us an indication of what luminosity-to-mass ratio is required for radio detection. This also provides an idea of the evolutionary stages of these young massive stars. In other words, the luminosity-to-mass ratios is an indicator of when radio emission begins in a YSO hence can give a clue about the evolution stages of YSOs, thus in an evolutionary succession (for massive star formation), jets (usually with low radio emission and hence low luminosity-to-mass ratios) emerge after the collapse of cores (less evolved) and accretion processes followed by newly formed high mass stars until an HII region is formed with high radio emission and luminosity-to-mass ratios (more evolved phase). In Figure 3.18 below, we plot the radio luminosities of the entire CORE targets (except for W3 IRAS 4 which do not have any previously measured or estimated integrated flux hence its radio luminosity could not be computed) against their computed parental core-luminosity-to-mass ratio. The targets are classified following the same scheme as described in Section 3.3 above. Also, the correlation fit (represented as a black line) is shown on the plot.

We notice a moderate correlation, thus with a Pearson's r of 0.14 (see Figure 3.18 and Table 3.12) between the radio luminosity and the parental core-luminosity-to-mass ratio. However, we spot an outlier, a source with a very low radio luminosity but a high luminosity-to-mass ratio. This source is G133.9476+01.0648 or W3($H_2O$), which is classified as an HII region (not bright at radio wavelengths, flux of $< 0.03$ mJy). See Figure 3.18 for details. The reason for the high luminosity-to-mass ratio is due to the fact that W3($H_2O$) is close to a really bright HII region W3 (OH) and the estimated luminosity is the combined luminosity for the entire field.

Furthermore, Figure 3.18 shows that the luminosity-to-mass ratio for most of our targets lie roughly between the range 50 to 1000 $L_\odot M_\odot^{-1}$. Therefore, for the entire CORE targets (whether a jet or an HII region) the minimum luminosity-to-mass ratio below which there are no radio

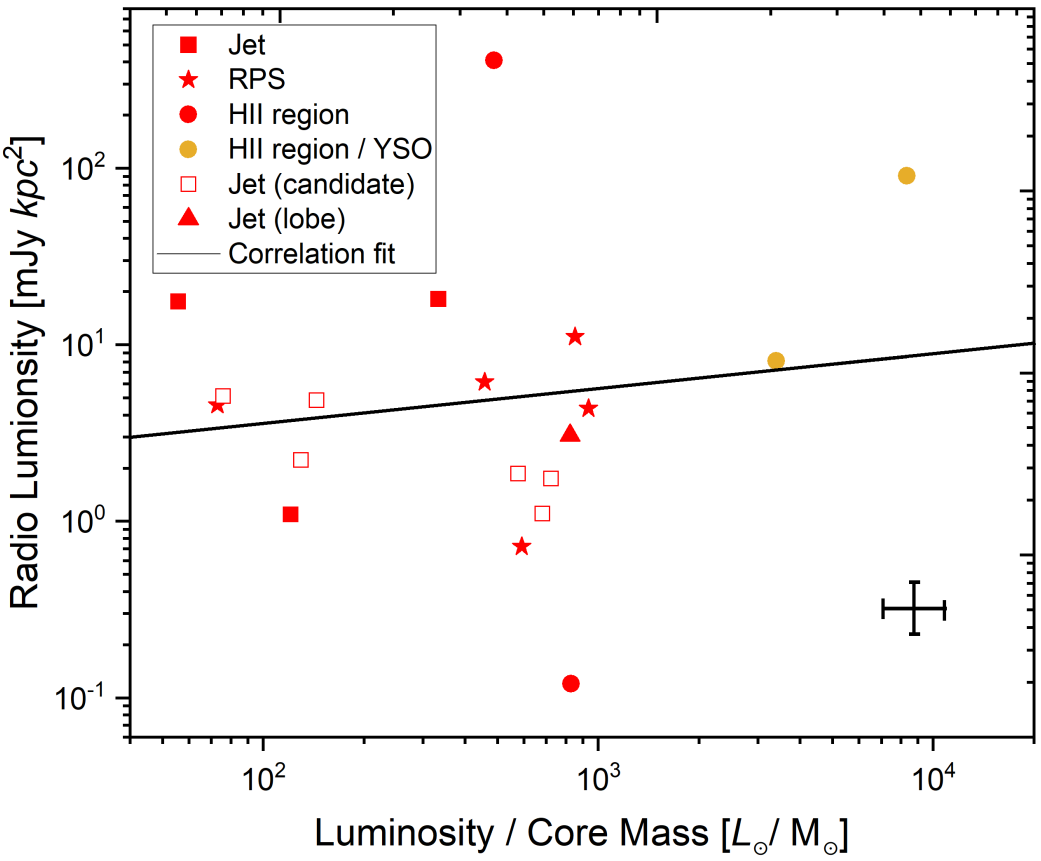


Figure 3.18 | **Radio luminosities against parental core-luminosity-to-mass ratio.** Radio luminosities of the entire CORE sample against parental core-luminosity-to-mass ratio (both parental core masses (masses associated with the cores of the detected YSOs) and luminosity are obtained from Beuther et al. (2018). The legend on the graph provides a brief description of our targets thus same as the classification used in Figure 3.15. See Table 3.14 for details of the classification. The correlation fit is represented as a black line on the plot. **Notes**: Masses are obtained from Beuther et al. (2018) thus, masses calculated mostly from SCUBA 850 μm fluxes, 1.2 mm continuum data, 1.1 mm continuum data and based on $C^{18}O(3-2)$ data (Beuther et al. 2002, Di Francesco et al. 2008, Ginsburg et al. 2013 and Maud et al. 2015). 1 (W3 IRAS 4) out of the 20 CORE targets do not have any previously measured or estimated integrated flux hence its radio luminosity could not be computed. Typical error bars are shown in the bottom right corner of plot.

detections (excluding G133.6945+01.2 which we do not find or measure any integrated flux value at radio wavelengths, hence radio luminosity could not be computed) is approximately 50 $L_\odot M_\odot^{-1}$. We also observe from Figure 3.18 that the YSOs classified as jets and/or jet candidates (less evolved phase of massive star formation) have core-luminosity-to-mass ratio between 50 to 190 $L_\odot/M_\odot$. While all the HII regions have core-luminosity-to-mass ratio greater than approximately 190 $L_\odot/M_\odot$ (since they are more evolved). Despite our relatively small sample

size, we see evidence of this evolutionary trait for the CORE targets as evident in our plot. This evolutionary trait has also been identified by Purser et al. (2021).

### 3.3.1 Sample masses against core masses

Both sample and core masses have been defined above (see Section 3.3 for details). Seen in Figure 3.19 is a plot of the sample masses against the core masses of the CORE sources. Also, the correlation fit (represented as a black line) is shown on the plot. In general, we observe from Figure 3.19 that there is some indication that larger global or sample masses tend to lead to large core masses (Seen by the best of fit line with as associated Pearson's r value of 0.43. See Table 3.12 for correlation values) for our targets. We notice a few outliers, a jet (see Table 3.14 for details about classification) towards the high end of the measured sample mass and a source (HII region) with a lower core mass but a significantly high sample mass. The jet outlier is G108.7575-00.986, seen in Figure 3.19 and is reported to be ejecting material hence the measured high sample mass could include some of this material and other ionized material in the vicinity of this YSO. Secondly, we know that the source with a lower core mass but a high sample mass is S87 IRS1 which is classified as an HII region/YSO. The measured high sample or global mass is probably an over estimation of the actual YSO mass or due to contribution from the HII region in the field or associated with this source.

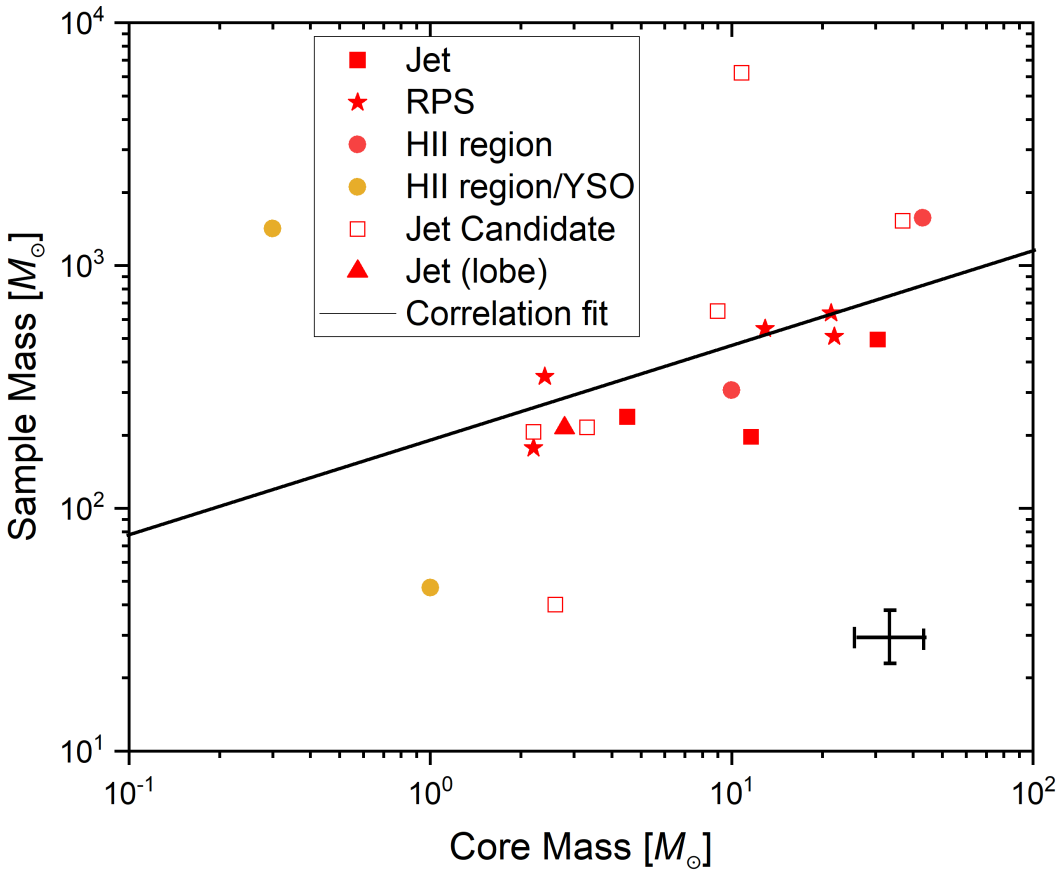


Figure 3.19 | **Trends between sample and core masses.** Here, we compare the sample masses against core masses with best line of fit indicated on the plot (black line). The legend on the graph provides a brief description of our targets thus same as the classification used in Figure 3.15 (see Table 3.14 for details). The correlation fit is represented as a black line on the plot. **Notes**: Core and sample masses for all our targets are obtained from Beuther et al. (2018). Typical error bars are shown in the bottom right corner of plot.

## 3.4 Millimetre analysis: 18A-104 targets

### Millimetre analysis of G133.6945+01.2

Comparing the detected HII region to the positions of the cores detected by Beuther et al. (2018) reveals that the HII region is below cores 6 and 5, as shown in our edited image (see Figure 3.20 below). Looking at the structures around the HII region as seen in the millimetre image, it is likely that the detected HII region is ionizing its environment and perhaps affecting cores 6 and 5. Given that Beuther et al. (2018) measured no mass for cores 5 and 6, it could suggest that these cores are just beginning to form.

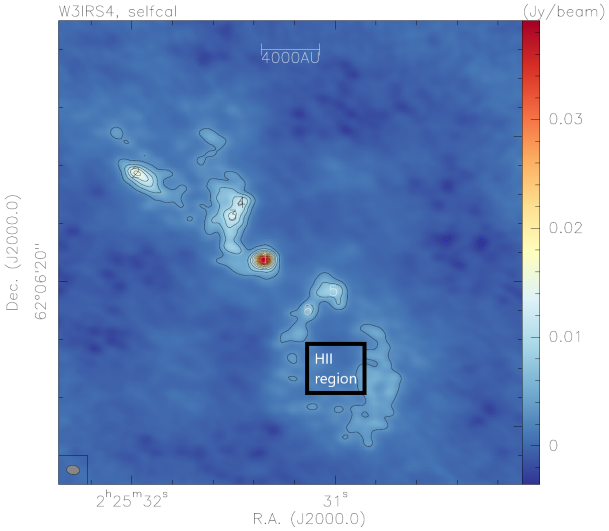


Figure 3.20 | **Millimetre image of G133.6945+01.2.** An edited millimetre image of G133.6945+01.2 showing 6 detected cores labelled 1 to 6. We use a black rectangle to indicate the approximate position of the detected HII region. Image taken from Beuther et al. (2018).

### G075.7822+00.3

Beuther et al. (2018) have shown the presence of 3 cores in this field (see Beuther et al. 2018 for details), the largest core has a mass of 12.9 $M_{\odot}$ whose position matches with that of the YSO or radio point source). The millimetre morphology is similar to that of a field with an outflow (detection of warm gas or clouds (69 K) in the field). Specifically, cores 2, 3 and 4 resemble outflow structures which are clearly associated with core 1 (the radio point source) which we did not detect.

**G078.8867+00.7**

Beuther et al. (2018), has shown the presence of up to 3 cores in this field (labelled, 1, 2 and 3, see Beuther et al. 2018 for details). They have masses of 21.4, 0.9 and 0.5 $M_{\odot}$ respectively. The YSO matches with the position of core 1. It is likely that core 2 is associated with the YSO, probably a core formed as a result of emission from the YSO.

**IRAS 21078+5211**

IRAS 21078+5211 is a very complex field as seen at millimetre wavelengths with the detection of 20 associated cores together with extended structures which provide a clear indication of fragmentation in this field (Beuther et al. 2018). See (Beuther et al. 2018) for details. Our YSO position matches with Beuther et al. (2018)'s core 1 which has a mass of 2.2 $M_{\odot}$. The millimetre image suggests that cores 1, 2 and 3 are related, probably the YSO (core 1) is influencing these close cores through the emission of radiation into its close environment. The entire field suggests a picture of an active HII region with a lot of activity in the field. This active HII region have been confirmed by other radio studies for example by Krasnov et al. (2018), where strong maser burst have been observed in the field.

**G109.8715+02.1**

Beuther et al. (2018) show that G109.8715+02.1 has a characteristic strong spectral line emission, pointing to the presence of hot molecular cores. These cores are visible in our radio image (see Figure 3.8).

In the 1.37 mm continuum image (see Beuther et al. 2018 for details) Beuther et al. (2018) detected 2 main cores separated by a distance of 2382 AU and masses of 2.6 (core 1 whose position correlates with that of our YSO) and 0.2 $M_{\odot}$ (core 2) respectively. Interestingly, in our radio image, we detect up to 5 main cores (shown in Figure 3.8). The millimetre morphology (field temperature of 119 K with a nonuniform structure around the YSO or radio point source) suggests that the YSO is probably embedded in a warm cloud or perhaps an HII region.

**NGC 7538S**

Di Francesco et al. (2008) have studied NGC 7538S at submillimetre wavelength using SCUBA and made an 850 μm map showing the star forming region where our source resides. Their

study show several structures in the field with intensities ranging from -0.1 to 3.2 Jy beam$^{-1}$. Another study by Feng et al. (2016) have detected 3 main cores, MM1, MM2 and MM3 (see Feng et al. 2016 for details) in this field. They suggested that our YSO is associated with source MM1 and reported a peak flux of 25.7 ±0.80 mJy beam$^{-1}$.

A recent millimetre study by Beuther et al. (2018) indicates that NGC 7538S is associated with up to 6 cores labelled 1 to 6 (see Beuther et al. 2018 for details). Our YSO position matches with core 1. This core has a mass of 4.5 $M_{\odot}$. The orientation of the other cores depicts that of an outflow morphology which resemble our radio image. It is possible that core 4 is as a result of the YSO in the field.

**NGC 7538IRS1**

Similar to NGC 7538S, NGC 7538IRS1 has been studied by Feng et al. (2016) and Beuther et al. (2018) at millimetre wavelengths. They both show that NGC 7538IRS1 has a single core (our source M, see Beuther et al. 2018 and Feng et al. 2016 for details). Beuther et al. (2018) records a mass of 43 $M_{\odot}$ for the detected millimetre core. This core is likely to be at the hot-core stage with a temperature of 82 K (Beuther et al. 2018).

To compare our radio detections to that of the millimetre studies, both do not show or detect our source N which is not surprising as it is about 4 arcseconds away (out of the field of view of the millimetre studies) from the compact source M. The morphology at both millimetre and radio wavelengths suggest that this YSO is compact. However, our radio image (Figure 3.11 and 3.12) suggests that perhaps there is an ongoing activity that is emitting some emission from this core, which can be attributed to source mmS in the millimetre image (see Feng et al. 2016 for details) by Feng et al. (2016).

**IRAS 23385+6053**

Molinari et al. (2002) resolved IRAS 23385+6053 into a cluster of YSOs at millimetre and centimetre wavelengths and suggested that the radio sources VLA 1 and 2 have a 20 cm (1 GHz) counterpart, NVSS 233828+605350 which has a characteristic flat radio spectrum.

A 1.4 mm study by Cesaroni et al. (2019) detected 6 cores in this field. These cores are labelled A1, A2, B, C, D and E (see Cesaroni et al. 2019 for details). They suggest the presence of an outflow which is being driven by a low-mass star in the field. Our YSO position is likely to be

either core A1 or A2 or both. A recent study by Beuther et al. (2018) detected 3 cores (see Beuther et al. 2018 for details) of which core 1 correlates with our YSO position. Beuther et al. (2018) reports a mass of 21.9 $M_{\odot}$ for this core. The morphology (2 cores to the east and west of the YSO and a disruption of material or gas in the YSO's immediate environment) of this field suggests the presence of an outflow activity which is not seen in our radio image, perhaps owing to the fact that this is a massive star forming region with cores that are still very young or at the early evolutionary stage (Molinari et al. 1998b, Molinari et al. 2008 and Cesaroni et al. 2019).

## 3.5 18A-104 targets: outflows and jets

Outflows and jets are common in protostars of varying masses. Snell et al. (1980) and Rodriguez et al. (1980) first found evidence of these outflows and jets in protostars. Protostars interact with their stellar environment, especially their parent molecular cloud through these protostellar outflows (Walawender et al. 2016). These outflows are driven at high speeds of order 100 $kms^{-1}$ as part of the process of accretion (Walawender et al. 2016). In general, stellar structures associated with magnetic fields and rotating and accreting matter eject materials in the form of collimated or bipolar outflows (Walawender et al. 2016 and Bally 2016). The driving mechanism behind outflows are not yet known with some suggesting that this may driven by jets (Reipurth and Bally 2001, Sanna et al. 2016 and Purser et al. 2021). Others (for example Guzmán et al. 2012) have also suggested that the momentum associated with some jets are too small to drive outflow especially in the case of large-scale outflows (Purser et al. 2021).

In this section, we discuss briefly the 18A-104 targets that have been observed with outflows and jets.

#### NGC 7538S outflow and jet

In our radio image (Figure 3.10) of NGC 7538S, there is a clear evidence of a bipolar outflow and jet activity. We measure the flux of each side of this bipolar outflow (one directed toward the north-east and the other to the south-west) as approximately 0.30 mJy. Millimetre images by Feng et al. (2016) and Beuther et al. (2018) vividly reveal a complex field which is probably due to the disruption in the environment of the YSO (our target) as a result of the outflow and jet activity detected in our radio image.

#### G109.8715+02.1 outflow and jet

Our radio images shows a busy field with proof of outflow and jet activity associated with source V (our YSO) presented in Figure 3.8. There is evidence of a possible jet activity as evidenced by our contour maps (Figures 3.9) where we see our target extended or lobe-like. To confirm an outflow activity in this field, Curiel et al. (2006) have also made detections of this outflow at 7 mm, 1.3 cm and 3.6 cm. Furthermore, the core of this outflow have been picked up at millimetre wavelength by Beuther et al. (2018).

### 3.5.1 Disc and jet or outflow orientation

#### G078.8867+00.7 disc

Millimetre observations indicate the presence of an outflow in G078.8867+00.7 (Beuther et al. 2018), but the disc properties are not clear. Recently, Olguin et al. (2020) obtained a disc mass of 6 $M_{\odot}$ and a radius of 2200 AU for AFGL 2591 through resolved multi-wavelength data and a radiative transfer model. They also found that this disc is inclined at an angle between $25^{o} - 35^{o}$ with respect to the line of sight. They suggested an edge-on disc orientation (which they attribute to changing position angles due to precession) in the outflow direction but a face-on inclination for the inner envelope of the outflow. Another study by Suri et al. (2021) on the disk found in G078.8867+00.7 have suggested the occurrence of a disk accretion where the disk themselves undergo fragmentation and form associated cores. All these results (including our radio observations of this source) do not provide a clear indication on the disc-outflow orientation.

#### IRAS 21078+5211 (G092.69+3.08) disc

Moscadelli et al. (2021) have detected a collimated bipolar molecular outflow in the south-west and north-east direction emerging from the most massive core (core 1) in this field (our YSO). They provide evidence (reported a gradient of amplitude of local standard of rest velocity ($V_{LSR}$) of about 14 $kms^{-1}$ over a distance of 500 AU) of an edge-on, rotating disk perpendicular to the radio jet. Our radio results do show 2 distinct regions which in no way provides information on the existence of a disc.

## 3.6 Summary: analysing the entire CORE sample

### 3.6.1 Radio properties of the CORE sample

19 of the CORE sources have associated radio detections either in this work or by others. For example by Wyrowski et al. (1999), Wilner et al. (1999), Gibb and Hoare (2007), Obonyo (2020) and Purser et al. (2021). Specifically, for our 8 targets (including NGC 7538IRS1 and NGC 7538S which were in Purser et al. (2021)'s field NGC 7538IRS9), we detected radio emission associated with all the YSOs, except for G133.6945+01.2 which we do not detect, though we detected an HII region in the field (see Figure 3.1).

Table 3.13 shows the entire CORE sample with their positions (Beuther et al. 2018), measured or estimated integrated flux values, observed wavelengths and references associated with their measured or estimated integrated flux values. For G133.6945+01.2 we do not find or measure any integrated flux values at radio wavelengths. These integrated fluxes shown in Table 3.13 below are those used to compute our radio luminosities (shown in Table A.2). Sources in bold are the 18A-104 targets (including those imaged from the Purser et al. 2021 data-set) and associated fluxes are measured using the Gaussian fit method in CASA. For all other sources, their corresponding integrated values are taken from published works (indicated as 'Ref' in the Table below). For source W3($H_2O$), its flux value has an upper limit of 3 sigma (Wilner et al. 1999).

| Target name | RA(J2000) | Dec(J2000) | Int. flux (mJy) | Freq. (GHz) | Ref. |
|---|---|---|---|---|---|
| **G133.6945+01.2** | 02:25:31.22 | +62:06:21.00 | - | - | - |
| G133.9476+01.0648 | 02:27:04.60 | +61:52:24.73 | $< 0.03$ | 8 | Wilner et al. (1999) |
| G138.2957+01.555 | 03:01:31.32 | +60:29:13.20 | 0.13 ±0.04 | 5.8 | Obonyo (2020) |
| G139.9091+00.197 | 03:07:24.52 | +58:30:48.30 | 0.60 ±0.02 | 5.8 | Purser et al. (2021) |
| S87 IRS1 | 19:46:20.14 | +24:35:29.00 | 18.67 ±1.96 | 5 | Purcell et al. (2013) |
| **G075.7822+00.3** | 20:21:44.03 | +37:26:37.70 | 0.77 ±0.05 | 6 | This work |
| S106 | 20:27:26.77 | +37:22:47.70 | 4.80 ±0.30 | 8.5 | Gibb and Hoare (2007) |
| **G078.8867+00.7** | 20:29:24.86 | +40:11:19.40 | 0.40 ±0.01 | 6 | This work |
| G084.9505-00.691 | 20:55:32.47 | +44:06:10.10 | 0.16 ±0.01 | 5.8 | Purser et al. (2021) |
| **IRAS 21078+5211** | 21:09:21.64 | +52:22:37.50 | 0.26 ±0.02 | 6 | This work |
| G094.6028-01.797 | 21:39:58.25 | +50:14:20.90 | 0.32 ±0.03 | 5.8 | Obonyo (2020) |
| G100.3779-03.578 | 22:16:10.35 | +52:21:34.70 | 0.09 ±0.01 | 5.8 | Purser et al. (2021) |
| **G109.8715+02.1** | 22:56:17.98 | +62:01:49.50 | 3.80 ±0.43 | 6 | This work |
| G108.7575-00.986 | 22:58:47.25 | +58:45:01.60 | 0.12 ±0.01 | 5.8 | Purser et al. (2021) |
| IRAS 23033+5951 | 23:05:25.00 | +60:08:15.49 | 0.95 ±0.13 | 5.8 | Obonyo (2020) |
| **NGC 7538S** | 23:13:44.86 | +61:26:48.10 | 2.49 ±0.20 | 6 | This work |
| **NGC 7538IRS1** | 23:13:45.36 | +61:28:10.55 | 56.0 ±3.90 | 6 | This work |
| NGC 7538IRS9 | 23:14:01.68 | +61:27:19.10 | 0.42 ±0.08 | 5.8 | Purser et al. (2021) |
| IRAS 23151+5912 | 23:17:21.01 | +59:28:47.49 | 0.16 ±0.01 | 5.8 | Purser et al. (2021) |
| **IRAS 23385+6053** | 23:40:54.40 | +61:10:28.20 | 0.19 ±0.02 | 6 | This work |

Table 3.13 | **CORE targets: measured fluxes.** All the 20 CORE sources with their measured or estimated integrated fluxes. Targets in bold are the 18A-104 sources (including those imaged from the Purser et al. 2021 data-set) and associated fluxes are measured using the Gaussian fit method. For G133.6945+01.2 we do not find or measure any integrated flux values at radio wavelengths. These fluxes are those used to compute our radio luminosities. **References** here show where these integrated flux values were taken from. NB: Error for flux value of W3($H_2O$) has an upper limit of 3 sigma.

### 3.6.2 Morphology of entire CORE sample

All these sources are young massive stars or stellar objects and forming regions with at least an $8M_{\odot}$ mass star present and are located at distances less than 6 kpc from the earth and also have luminosities greater than $10^4L_{\odot}$ (Beuther et al. 2018). In general, all the CORE sources are at the same evolutionary stage, luminous and high mass protostellar objects (HMPOs) or massive young stellar objects (MYSOs). Most of these targets have IR associations. Table 3.14 details the type of infrared classification associated with these young massive stars.

From the measured or estimated integrated fluxes values (see Table 3.13 for details), most of the 20 CORE sources have integrated fluxes between 0.03 to 4.80 mJy (exceptions are S87 IRS1 and NGC 7538IRS1 which have fluxes of 18.67 and 56.00 mJy respectively).

In terms of millimetre studies, all the 20 targets (except G133.6945+01.2) detected at radio wavelengths (by Obonyo 2020, Purser et al. 2021 and this work) have associated millimetre cores (Beuther et al. 2018). We explore this further in the Section below.

| Target name | Radio morphology | IR-bright | Reference |
|---|---|---|---|
| G133.6945+01.2* | RPS | ✓ | Lumsden et al. (2013) |
| G133.9476+01.0648 | HII region | ✗ | Lumsden et al. (2013) |
| G138.2957+01.555 | Jet | ✓ | Purser et al. (2021) |
| G139.9091+00.197 | RPS | ✓ | This work |
| S87 IRS1 | HII region/YSO | ✓ | Lumsden et al. (2013) |
| G075.7822+00.3* | RPS | ✗ | This work |
| S106 | HII region/YSO | ✓ | Lumsden et al. (2013) |
| G078.8867+00.7* | RPS | ✓ | Urquhart et al. (2009) |
| G084.9505-00.691 | Jet candidate | ✓ | Purser et al. (2021) |
| IRAS 21078+5211* | RPS | ✗ | Moscadelli et al. (2016) |
| G094.6028-01.797 | Jet candidate | ✓ | Purser et al. (2021) |
| G100.3779-03.578 | Jet candidate | ✓ | Purser et al. (2021) |
| G109.8715+02.1* | Jet candidate | ✗ | Curiel et al. (2006) |
| G108.7575-00.986 | Jet candidate | ✓ | Purser et al. (2021) |
| IRAS 23033+5951 | Jet | ✗ | Purser et al. (2021) |
| NGC 7538S* | Jet | ✗ | This work |
| NGC 7538IRS1* | HC HII region | ✓ | Lumsden et al. (2013) |
| NGC 7538IRS9 | Jet with lobe | ✓ | Purser et al. (2021) |
| IRAS 23151+5912 | Jet candidate | ✓ | Purser et al. (2021) |
| IRAS 23385+6053* | RPS | ✗ | This work |

Table 3.14 | **CORE targets: morphology classification.** Here, we classify the CORE sources according to their respective observed morphologies: radio point source (RPS), jets, jet candidates, lobes, jets with lobes, candidate jets with lobes and HII regions (Purser et al. 2021). These classifications are not just based on the radio flux but also on infrared characteristics and morphology as discussed by Purser et al. (2021). Objects classified as jet/jet candidate by Purser et al. (2021) are mostly radio point sources which have complimentary multi-wavelength data to confirm their jet/jet candidacy. Where RMS survey is by Lumsden et al. (2013). NB: Source classification as IR-bright or quiet sources with '*' are the 18A-104 targets and those imaged from the Purser et al. (2021) data-set. '✓' are targets classified as IR-bright and '✗' are those classified as IR-quiet. Reference: Beuther et al. (2018).

### 3.6.3 Summary: millimeter and infrared properties

All these sources have been studied at millimetre wavelengths, for example at 1.37 mm by Beuther et al. (2018) where fragmentation properties were studied. From these studies, the 20 targets all have associated cores, ranging from 1 to up-to 20 cores with evidence of fragmentation (Beuther et al. 2018). We have detected and matched 19 (except for G133.6945+01.2 which we do not detect) radio sources to 19 millimetre cores or sources. This could potentially give further incite into the fragmentation properties of the entire CORE sample.

Most of the CORE targets have been shown to harbor infrared sources or have infrared associations (we know this through the RMS survey, Lumsden et al. 2013). With respect to IR-brightness, the general knowledge is that IR-bright sources (or specifically, protostellar massive dense cores) would be detected at mid-infrared wavelengths and are mostly characterized by luminosities greater than $10^4 L_\odot$ while IR-quiet sources are those that are usually dense and made up of massive cloud fragments and are not detectable at mid-infrared wavelengths. That is, luminosities between $10^3$ to $10^4$ $L_\odot$ and sizes from 0.01 to 1 parsec (Motte et al. 2018, Ward-Thompson et al. 2006, Sridharan et al. 2005 and Beuther et al. 2007b). In the context of this work, we classify our sources as IR-bright or -quiet using the criteria set by Beuther et al. (2018) and satisfy Equation 1.1 in Chapter 1.

# Chapter 4

# Conclusion and future work

## 4.1 Conclusion

Results from our all targets serves as a complementary study to the CORE Large Programme on the NOEMA mm interferometer. We have provided high resolution (0.33 arcseconds) continuum maps of the radio emission from young stellar objects that are part of the CORE programme. Prior to this work, these targets have not been observed with JVLA. Our results together with the CORE study, provides high resolution information on a sample of 20 protostars with radio emission. We have detected cores and other structures related to these massive protostars and show connections with cores, lobes, jets and disks.

In the past, C-band observations of massive young stellar objects have revealed many new detections of the jet cores associated with the infrared source. In a lot of other cases, radio lobe and core components which are relatively faint have been observed and seen to be aligned and define the axis of the radio jet. In this work, we have detected for the first time some of these jet cores and radio lobes (for example in NGC 7538S, where the radio emission seem to be almost perpendicularly aligned to the millimetre emission).

### 4.1.1 Radio detections, jets and jet orientation

For 7 targets, including 2 targets imaged from fields in the Purser et al. (2021) data-set, we detected radio continuum emission (at 6 GHz with JVLA in its A configuration) from the associated YSOs. We do not detect any related radio continuum emission for our YSO in field G133.6945+01.2, though we detect radio emission from an HII region in the field.

For our sample, imaging revealed a jet morphology for NGC 7538S and G109.8715+02.1156. In general, out of the 20 CORE targets, 10 are considered as jets or jet candidates. The others are HII regions, radio point sources, compact sources or have cometry morphologies. Tables 3.14 and A.3 show these various classifications and the count of these different objects in the CORE sample.

One of the goals of this work is to investigate whether jets or outflows are always precisely perpendicular to their associated disc and or cores using results from this work and information in literature (radio, millimetre and infrared data) for the 18A-104 targets. In this work, we detect NGC 7538S as a jet with a jet orientation approximately perpendicular to the millimetre emission as clearly depicted in our radio image (see Figure 3.10). For our target G109.8715+0.2.1156 (labelled as source V in our radio image, see Figure 3.8 we do not see any clear jet orientation (only a lobe in the east-south direction) though another source II in the same field as source V seem to have 2 jet-like structures (presented in our contour image as shown in Figure 3.10) almost perpendicular to the detected millimetre emission.

## 4.2 Main conclusions

Our main conclusions can be summarized as follows:

(1) We have imaged 8 of the CORE targets that did not have any previous JVLA radio data prior to this work and detect radio emission in 7 of these young massive stars. The exception is G133.6945+01.2 where we did not detect the related YSO radio emission, though we detect radio emission from an HII region in the field.

(2) With respect to outflow or jet or lobes, 2 (G109.8715+02.1 and NGC 7538S) out of 7 targets that we detected clearly revealed structures which are indicative of an outflow or jet activities in their respective fields. In all, there are 10 jets in the CORE sample.

(3) In terms of jet orientation (at 6 GHz), 5 of the CORE targets show evidence of a perpendicular jet orientation to their respective observed millimetre emission. For example, our target NGC 7538S show a perpendicular orientation to the observed millimetre emission in the north-east and south-west direction.

(4) 19 CORE targets show a divergence (massive young stellar objects tend to have higher radio luminosities compared to their low-mass counterparts) from low-mass stars and HII regions in radio luminosity and bolometric luminosity parameter space. This indicates that young massive stars are likely to be formed through a scaled up version of their low-mass counterparts.

(5) For most of the CORE targets there is an observed trend of large global or sample masses leading to large core masses.

(6) Comparing previous radio results, our sources (18A-104 targets) G078.8867+00.7 and G109.8715+02.1 show an indication of variability. Additionally, other CORE targets such as S106 and G094.6028-01.797 have been shown to be variable sources from literature.

(7) We have provided a comparative study of the radio and millimetre characteristics of the 18A-104 targets, especially in terms of the detected cores. Our 8 targets all have associated millimetre cores. Similarly, the rest of the CORE targets (12 in all) at radio wavelength also have associated millimetre cores. Identification of these cores at radio wavelengths could support fragmentation studies at millimetre wavelength and help understand how fragmentation in young massive stars occur.

## 4.3 Future work

Simulations of jets found in these massive protostars will be key to understanding the various observed features of jets in this work. Also, a follow-up on the target that we did not detect any radio emission from would help confirm if this target is radio quiet because it is still in its natal envelope and hence not detectable at radio wavelengths.

Further sensitive millimetre observation and analysis will help understand the processes driving these cores and how they evolve.

Results from Hofner et al. (2002) suggest that young massive stars could be emitters of X-rays and can be detected even if these young massive stars are in high-density environments. An interesting study would be to observe the CORE targets and investigate the emission of these X-rays and understand how these X-ray emission affect their environments.

To probe the jets detected in this work further and understand the mechanism behind the emission of these jets would require high sensitivity survey like the Next Generation Very Large Array (ngVLA) and eMERLIN (at high spatial resolution).

Finally, a larger sample study (especially in the southern hemisphere with the Square Kilometre Array, SKA) of the radio emission from young massive stars would be very important in understanding the formation of these objects and how they influence their stellar environment. This will be essential in building a strong theoretical framework for the formation and evolution of these objects.

# References


Ahmadi, A., H. Beuther, J. C. Mottram, F. Bosco, H. Linz, T. Henning, J. M. Winters, R. Kuiper, R. Pudritz, Á. Sánchez-Monge, E. Keto, M. Beltran, S. Bontemps, R. Cesaroni, T. Csengeri, S. Feng, R. Galvan-Madrid, K. G. Johnston, P. Klaassen, S. Leurini, S. N. Longmore, S. Lumsden, L. T. Maud, K. M. Menten, L. Moscadelli, F. Motte, A. Palau, T. Peters, S. E. Ragan, P. Schilke, J. S. Urquhart, F. Wyrowski, and H. Zinnecker (2018). "Core Fragmentation and Toomre Stability Analysis of W3($H_2O$). A Case Study of the IRAM NOEMA Large Program CORE". In: *Astronomy and Astrophysics* 618, p. 46.

Andre, P., D. Ward-Thompson, and M. Barsony (2000). "From Prestellar Cores to Protostars: the Initial Conditions of Star Formation". In: *Protostars and Planets IV*. Ed. by V. Mannings, A. P. Boss, and S. S. Russell, p. 59.

Andre, P., D. Ward-Thompson, and M. Barsony (1993). "Submillimeter Continuum Observations of Rho Ophiuchi A: The Candidate Protostar VLA 1623 and Prestellar Clumps". In: *Astrophysical Journal* 406, p. 122.

Anglada, G. (1995). "Centimeter Continuum Emission from Outflow Sources". In: *Revista Mexicana de Astronomia y Astrofisica Conference Series*. Ed. by S. Lizano and J. M. Torrelles. Vol. 1. Revista Mexicana de Astronomia y Astrofisica Conference Series, p. 67.

Arce, H. G., D. Shepherd, F. Gueth, C. F. Lee, R. Bachiller, A. Rosen, and H. Beuther (2007). "Molecular Outflows in Low- and High-Mass Star-forming Regions". In: *Protostars and Planets V*. Ed. by B. Reipurth, D. Jewitt, and K. Keil, p. 245.

Bacmann, A., P. André, J. L. Puget, A. Abergel, S. Bontemps, and D. Ward-Thompson (2000). "An ISOCAM Absorption Survey of the Structure of Pre-stellar Cloud Cores". In: *Astronomy and Astrophysics* 361, p. 555.

Ballesteros-Paredes, J., R. S. Klessen, M. M. Mac Low, and E. Vazquez-Semadeni (2007). "Molecular Cloud Turbulence and Star Formation". In: *Protostars and Planets V*. Ed. by B. Reipurth, D. Jewitt, and K. Keil, p. 63.

Bally, J., B. Reipurth, and C. J. Davis (2007). "Observations of Jets and Outflows from Young Stars". In: *Protostars and Planets V*. Ed. by B. Reipurth, D. Jewitt, and K. Keil, p. 215.

Bally, J. (2016). "Protostellar Outflows". In: *Annual Review of Astronomy Astrophysics* 54, p. 491.

Bate, M. R. and I. A. Bonnell (2005). "The Origin of the Initial Mass Function and its Dependence on the Mean Jeans Mass in Molecular Clouds". In: *MNRAS* 356.4, p. 1201.

Bell, A. R. (1978). "The Acceleration of Cosmic Rays in Shock Fronts - II." In: *MNRAS* 182, p. 443.

Beuther, H., E. B. Churchwell, C. F. McKee, and J. C. Tan (2007a). "The Formation of Massive Stars". In: *Protostars and Planets V*. Ed. by B. Reipurth, D. Jewitt, and K. Keil, p. 165.

Beuther, H., J. C. Mottram, A. Ahmadi, F. Bosco, H. Linz, T. Henning, P. Klaassen, J. M. Winters, L. T. Maud, R. Kuiper, D. Semenov, C. Gieser, T. Peters, J. S. Urquhart, R. Pudritz, S. E. Ragan, S. Feng, E. Keto, S. Leurini, R. Cesaroni, M. Beltran, A. Palau, Á. Sánchez-Monge, R. Galvan-Madrid, Q. Zhang, P. Schilke, F. Wyrowski, K. G. Johnston, S. N. Longmore, S. Lumsden, M. Hoare, K. M. Menten, and T. Csengeri (2018). "Fragmentation and Disk Formation during High-mass Star Formation. IRAM NOEMA (Northern Extended Millimeter Array) Large Program CORE". In: *Astronomy and Astrophysics* 617, A100.

Beuther, H., P. Schilke, K. M. Menten, C. M. Walmsley, T. K. Sridharan, and F. Wyrowski (2002). "Massive Molecular Outflows". In: *Hot Star Workshop III: The Earliest Phases of Massive Star Birth*. Ed. by P. Crowther. Vol. 267. Astronomical Society of the Pacific Conference Series, p. 341.

Beuther, H., Q. Zhang, T. R. Hunter, T. K. Sridharan, and E. A. Bergin (2007b). "The $10^5$ $L_\odot$ High-mass Protostellar Object IRAS 23151+5912". In: *Astronomy and Astrophysics* 473.2, p. 493.

Bieging, J. H., D. C. Abbott, and E. B. Churchwell (1989). "A Survey of Radio Emission from Galactic OB Stars". In: *Astrophysical Journal* 340, p. 518.

Blandford, R. D. and D. G. Payne (1982). "Hydromagnetic Flows from Accretion Disks and the Production of Radio Jets." In: *MNRAS* 199, p. 883.

Blomme, R. (2011). "Radio Observations of Massive Stars". In: *Bulletin de la Societe Royale des Sciences de Liege* 80, p. 67.

Bonnell, I., C. Clarke, M. Bate, and J. Pringle (2001). "Accretion in Stellar Clusters and the Initial Mass Function". In: *MNRAS* 324.3, p. 573.

Bonnell, I. A., S. G. Vine, and M. R. Bate (2004). "Massive Star Formation: Nurture, not Nature". In: *Monthly Notices of the Royal Astronomical Society* 349.2, p. 735.

Bonnell, I. A. and M. R. Bate (2006). "Star Formation through Gravitational Collapse and Competitive Accretion". In: *MNRAS* 370.1, p. 488.

Bonnell, I. A., M. R. Bate, and H. Zinnecker (1998). "On the Formation of Massive Stars". In: *MNRAS* 298.1, p. 93.

Bosco, F., H. Beuther, A. Ahmadi, J. C. Mottram, R. Kuiper, H. Linz, L. Maud, J. M. Winters, T. Henning, S. Feng, T. Peters, D. Semenov, P. D. Klaassen, P. Schilke, J. S. Urquhart, M. T. Beltrán, S. L. Lumsden, S. Leurini, L. Moscadelli, R. Cesaroni, Á. Sánchez-Monge, A. Palau, R. Pudritz, F. Wyrowski, and S. Longmore (2019). "Fragmentation, Rotation, and Outflows in the High-mass Star-forming Region IRAS 23033+5951. A case Study of the IRAM NOEMA Large Program CORE". In: *Astronomy and Astrophysics* 629, A10.

Brandl, B., W. Brandner, F. Eisenhauer, A. F. J. Moffat, F. Palla, and H. Zinnecker (1999). "Low-mass Stars in the Massive HII Region NGC 3603 - Deep NIR Imaging with ANTU/ISAAC". In: *ESO Press Release, 10/1999*, p. 3.

Briggs, D. S. (1995). "High Fidelity Interferometric Imaging: Robust Weighting and NNLS Deconvolution". In: American Astronomical Society Meeting Abstracts 187, p. 112.

Brogan, C. L., T. R. Hunter, and E. B. Fomalont (2018). "Advanced Gain Calibration Techniques in Radio Interferometry". In: *ArXiv eprint*, p. 208.

Buehrke, T., R. Mundt, and T. P. Ray (1988). "A Detailed Study of HH 34 and its Associated Jet." In: *Astronomy and Astrophysics* 200, p. 99.

Burke, B. F. and F. Graham-Smith (2009). *An Introduction to Radio Astronomy*.

Burrows, A., M. Marley, W. B. Hubbard, J. I. Lunine, T. Guillot, D. Saumon, R. Freedman, D. Sudarsky, and C. Sharp (1997). "A Nongray Theory of Extrasolar Giant Planets and Brown Dwarfs". In: *Astrophysical Journal* 491.2, p. 856.

Caratti o Garatti, A., B. Stecklum, R. Garcia Lopez, J. Eislöffel, T. P. Ray, A. Sanna, R. Cesaroni, C. M. Walmsley, R. D. Oudmaijer, W. J. de Wit, L. Moscadelli, J. Greiner, A.

Krabbe, C. Fischer, R. Klein, and J. M. Ibañez (2017). "Disk-mediated Accretion Burst in a High-mass Young Stellar Object". In: *Nature Physics* 13.3, p. 276.

Carey, S. J., P. A. Feldman, R. O. Redman, M. P. Egan, J. M. MacLeod, and S. D. Price (2000). "Submillimeter Observations of Midcourse Space Experiment Galactic Infrared-Dark Clouds". In: *The Astrophysical Journal* 543.2, p. 157.

Carral, P., S. Kurtz, L. F. Rodrıguez, J. Martı, S. Lizano, and M. Osorio (1999). "VLA Continuum Observations of Suspected Massive Hot Cores". In: *RMXAA* 35, p. 97.

Carrasco-González, C., R. Galván-Madrid, G. Anglada, M. Osorio, P. D'Alessio, P. Hofner, L. F. Rodrıguez, H. Linz, and E. D. Araya (2012). "Resolving the Circumstellar Disk around the Massive Protostar Driving the HH 80-81 Jet". In: *The Astrophysical Journal* 752.2, p. L29.

Carrasco-González, C., L. F. Rodrıguez, G. Anglada, J. Martı, J. M. Torrelles, and M. Osorio (2013). "Discovery of Synchrotron Emission from a YSO Jet". In: *European Physical Journal Web of Conferences*. Vol. 61. European Physical Journal Web of Conferences, p. 3003.

Cesaroni, R., H. Beuther, A. Ahmadi, M. T. Beltrán, T. Csengeri, R. Galván-Madrid, C. Gieser, T. Henning, K. G. Johnston, P. D. Klaassen, R. Kuiper, S. Leurini, H. Linz, S. Longmore, S. L. Lumsden, L. T. Maud, L. Moscadelli, J. C. Mottram, A. Palau, T. Peters, R. E. Pudritz, Á. Sánchez-Monge, P. Schilke, D. Semenov, S. Suri, J. S. Urquhart, J. M. Winters, Q. Zhang, and H. Zinnecker (2019). "IRAS 23385+6053: An Embedded Massive Cluster in the Making". In: *Astronomy and Astrophysics* 627, A68.

Cesaroni, R., E. Churchwell, P. Hofner, C. M. Walmsley, and S. Kurtz (1994). "Hot Ammonia towards Compact HII Regions". In: *Astronomy and Astrophysics* 288, p. 903.

Chandler, C. J., J. E. Carlstrom, N. Z. Scoville, W. R. F. Dent, and T. R. Geballe (1993). "Infrared CO Emission from Young Stars: High-Resolution Spectroscopy". In: *The Astrophysical Journal* 412, p. L71.

Clarke, A. J., S. L. Lumsden, R. D. Oudmaijer, A. L. Busfield, M. G. Hoare, T. J. T. Moore, T. L. Sheret, and J. S. Urquhart (2006). "Evidence for Variable Outflows in the Young Stellar Object V645 Cygni". In: *Astronomy and Astrophysics* 457.1, p. 183.

Claussen, M. J., R. A. Gaume, K. J. Johnston, and T. L. Wilson (1994). "The W3 IRS 5 Cluster: Radio Continuum and Water Maser Observations". In: *The Astrophysical Journal* 424, p. L41.

Cohen, M. (1977). "The Nature of V645 Cygni = CRL 2789." In: *Astrophysical Journal* 215, p. 533.

Cohen, M. and L. Kuhi (1979). "Observational Studies of Star Formation: Conclusions." In: *The Astrophysical Journal* 227, p. L105.

Colley, D. (1980). "Radio Observations of W3 at 2.7 and 14.4GHz." In: *MNRAS* 193, p. 495.

Cowan, J. J. and C. Sneden (2006). "Heavy Element Synthesis in the Oldest Stars and the Early Universe". In: *Nature* 440.7088, p. 1151.

Crowther, P. A., S. M. Caballero-Nieves, K. A. Bostroem, J. Maız Apellániz, F. R. N. Schneider, N. R. Walborn, C. R. Angus, I. Brott, A. Bonanos, A. de Koter, S. E. de Mink, C. J. Evans, G. Gräfener, A. Herrero, I. D. Howarth, N. Langer, D. J. Lennon, J. Puls, H. Sana, and J. S. Vink (2016). "The R136 Star Cluster Dissected with Hubble Space Telescope/STIS. I. Far-ultraviolet Spectroscopic Census and the Origin of He II λ1640 in Young Star Clusters". In: *MNRAS* 458.1, p. 624.

Cunningham, A., M. R. Krumholz, R. I. Klein, and C. F. McKee (2009). "Protostellar Outflow Feedback in High Mass Star Formation". In: *American Astronomical Society Meeting Abstracts #214*. Vol. 214. American Astronomical Society Meeting Abstracts, p. 604.

Curiel, S., J. M. Girart, L. F. Rodrıguez, and J. Cantó (2003). "Very Large Array Observations of Proper Motions in YLW 15". In: *The Astrophysical Journal* 582.2, p. L109.

Curiel, S., P. T. P. Ho, N. A. Patel, J. M. Torrelles, L. F. Rodrıguez, M. A. Trinidad, J. Cantó, L. Hernández, J. F. Gómez, G. Garay, and G. Anglada (2006). "Large Proper Motions in the Jet of the High-Mass YSO Cepheus A HW2". In: *Astrophysical Journal* 638.2, p. 878.

Davies, B., M. G. Hoare, S. L. Lumsden, T. Hosokawa, R. D. Oudmaijer, J. S. Urquhart, J. C. Mottram, and J. Stead (2011). "The Red MSX Source Survey: Critical Tests of Accretion Models for the Formation of Massive Stars". In: *MNRAS* 416.2, p. 972.

Di Francesco, J., I. Evans Neal J., P. M. Harvey, L. G. Mundy, S. Guilloteau, and C. J. Chandler (1997). "Millimeter and Radio Interferometry of Herbig Ae/Be Stars". In: *Astrophysical Journal* 482.1, p. 433.

Di Francesco, J., D. Johnstone, H. Kirk, T. MacKenzie, and E. Ledwosinska (2008). "The SCUBA Legacy Catalogues: Submillimeter-Continuum Objects Detected by SCUBA". In: *The Astrophysical Journal Supplement* 175.1, p. 277.

Dreher, J. W. and W. J. Welch (1981). "Discovery of Shell Structure in the Ultracompact H II Region W3(OH)." In: *Astrophysical Journal* 245, p. 857.

Egan, M. P., R. F. Shipman, S. D. Price, S. J. Carey, F. O. Clark, and M. Cohen (1998). "A Population of Cold Cores in the Galactic Plane". In: *The Astrophysical Journal* 494.2, p. L199.

Eisner, J. A., G. H. Rieke, M. J. Rieke, K. M. Flaherty, J. M. Stone, T. J. Arnold, S. R. Cortes, E. Cox, C. Hawkins, A. Cole, S. Zajac, and A. L. Rudolph (2015). "Time-monitoring Observations of Brγ Emission from Young Stars". In: *MNRAS* 447.1, p. 202.

Feeney-Johansson, A., S. J. D. Purser, T. P. Ray, J. Eislöffel, M. Hoeft, A. Drabent, and R. E. Ainsworth (2019). "The First Detection of a Low-frequency Turnover in Nonthermal Emission from the Jet of a Young Star". In: *The Astrophysical Journal* 885.1, p. L7.

Feng, S., H. Beuther, D. Semenov, T. Henning, H. Linz, E. A. C. Mills, and R. Teague (2016). "Inferring the Evolutionary Stages of the Internal Structures of NGC 7538 S and IRS1 from Chemistry". In: *Astronomy and Astrophysics* 593, A46.

Fontani, F., R. Cesaroni, P. Caselli, and L. Olmi (2002). "The Structure of Molecular Clumps around High-mass Young Stellar Objects". In: *Astronomy and Astrophysics* 389, p. 603.

Frank, A., T. P. Ray, S. Cabrit, P. Hartigan, H. G. Arce, F. Bacciotti, J. Bally, M. Benisty, J. Eislöffel, M. Güdel, S. Lebedev, B. Nisini, and A. Raga (2014). "Jets and Outflows from Star to Cloud: Observations Confront Theory". In: *Protostars and Planets VI*. Ed. by H. Beuther, R. S. Klessen, C. P. Dullemond, and T. Henning, p. 451.

Garay, G. and S. Lizano (1999). "Massive Stars: Their Environment and Formation". In: *PASP* 111.763, p. 1049.

Gibb, A. G. and M. G. Hoare (2007). "A High-frequency Radio Continuum Study of Massive Young Stellar Objects". In: *MNRAS* 380.1, p. 246.

Ginsburg, A., J. Glenn, E. Rosolowsky, T. P. Ellsworth-Bowers, C. Battersby, M. Dunham, M. Merello, Y. Shirley, J. Bally, I. Evans Neal J., G. Stringfellow, and J. Aguirre (2013). "The Bolocam Galactic Plane Survey. IX. Data Release 2 and Outer Galaxy Extension". In: *The Astrophysical Journal Supplement* 208.2, p. 14.

Girart, J. M., M. T. Beltrán, Q. Zhang, R. Rao, and R. Estalella (2009). "Magnetic Fields in the Formation of Massive Stars". In: *Science* 324.5933, p. 1408.

Guzmán, A. E., G. Garay, K. J. Brooks, and M. A. Voronkov (2012). "Search for Ionized Jets toward High-mass Young Stellar Objects". In: *Astrophysical Journal* 753.1, p. 51.

Hachisuka, K., A. Brunthaler, K. M. Menten, M. J. Reid, H. Imai, Y. Hagiwara, M. Miyoshi, S. Horiuchi, and T. Sasao (2006). "Water Maser Motions in W3(OH) and a Determination of its Distance". In: *Astrophysical Journal* 645.1, p. 337.

Hamann, F. and S. E. Persson (1989). "High-Resolution Spectra of the Luminous Young Stellar Object V645 Cygni". In: *Astrophysical Journal* 339, p. 1078.

Harris, S. and C. G. Wynn-Williams (1976). "Fine Radio Structure in W3." In: *MNRAS* 174, p. 649.

Hartigan, P. and J. Morse (2007). "Collimation, Proper Motions, and Physical Conditions in the HH 30 Jet from Hubble Space Telescope Slitless Spectroscopy". In: *Astrophysical Journal* 660.1, p. 426.

Hasegawa, T. I. and G. F. Mitchell (1995). "CO J = 3–2 and HCO + J = 4–3 Observations of the GL 2591 Molecular Outflow". In: *Astrophysical Journal* 451, p. 225.

Hayashi, C. and T. Nakano (1963). "Evolution of Stars of Small Masses in the Pre-Main-Sequence Stages". In: *Progress of Theoretical Physics* 30.4, p. 460.

Herring, T. A., I. I. Shapiro, T. A. Clark, C. Ma, J. W. Ryan, B. R. Schupler, C. A. Knight, G. Lundqvist, D. B. Shaffer, N. R. Vandenberg, B. E. Corey, H. F. Hinteregger, A. E. E. Rogers, J. C. Webber, A. R. Whitney, G. Elgered, B. O. Ronnang, and J. L. Davis (1986). "Geodesy by Radio Interferometry: Evidence for Contemporary Plate Motion". In: *Journal of Geophysical Research* 91.B8, p. 8341.

Hoare, M. G. and T. B. Muxlow (1996). "MERLIN Observations of Luminous Young Stellar Objects". In: Astronomical Society of the Pacific Conference Series 93. Ed. by A. R. Taylor and J. M. Paredes, p. 47.

Hoare, M. G., C. R. Purcell, E. B. Churchwell, P. Diamond, W. D. Cotton, C. J. Chandler, S. Smethurst, S. E. Kurtz, L. G. Mundy, S. M. Dougherty, R. P. Fender, G. A. Fuller, J. M. Jackson, S. T. Garrington, T. R. Gledhill, P. F. Goldsmith, S. L. Lumsden, J. Martı, T. J. T. Moore, T. W. B. Muxlow, R. D. Oudmaijer, J. D. Pandian, J. M. Paredes, D. S. Shepherd, R. E. Spencer, M. A. Thompson, G. Umana, J. S. Urquhart, and A. A. Zijlstra (2012). "The Coordinated Radio and Infrared Survey for High-Mass Star Formation (The CORNISH Survey). I. Survey Design". In: *PASP* 124.919, p. 939.

Hoare, M. G., J. E. Drew, T. B. Muxlow, and R. J. Davis (1994). "Mapping the Radio Emission from Massive Young Stellar Objects". In: *The Astrophysical Journal* 421, p. L51.

Hofner, P., H. Delgado, B. Whitney, E. Churchwell, and H. Linz (2002). "X-Ray Detection of the Ionizing Stars in Ultracompact H II Regions". In: *The Astrophysical Journal* 579.2, p. L95.

Hogbom, J. A. and W. N. Brouw (1974). "The Synthesis Radio Telescope at Westerbork. Principles of Operation, Performance and Data Reduction". In: *Astronomy and Astrophysics* 33, p. 289.

Ilee, J. D., C. J. Cyganowski, P. Nazari, T. R. Hunter, C. L. Brogan, D. H. Forgan, and Q. Zhang (2016). "G11.92-0.61 MM1: A Keplerian Disc around a Massive Young Proto-O Star". In: *MNRAS* 462.4, p. 4386.

Johnston, K. G., T. P. Robitaille, H. Beuther, H. Linz, P. Boley, R. Kuiper, E. Keto, M. G. Hoare, and R. van Boekel (2015). "A Keplerian-like Disk around the Forming O-type Star AFGL 4176". In: *The Astrophysical Journal* 813.1, p. L19.

Johnstone, D., C. D. Wilson, G. Moriarty-Schieven, G. Joncas, G. Smith, E. Gregersen, and M. Fich (2000). "Large-Area Mapping at 850 Microns. II. Analysis of the Clump Distribution in the ρ Ophiuchi Molecular Cloud". In: *Astrophysical Journal* 545.1, p. 327.

Kahn, F. D. (1974). "Cocoons around Early-type Stars." In: *Astronomy and Astrophysics* 37, p. 149.

Kalcheva, I. E. (2018). "The Ultra-Compact H II Region Population of the Galaxy". PhD thesis. University of Leeds, UK.

Kameya, O., T. I. Hasegawa, N. Hirano, K. Takakubo, and M. Seki (1989). "High-Velocity Flows in the NGC 7538 Molecular Cloud". In: *Astrophysical Journal* 339, p. 222.

Kennicutt Robert C., J. (1998). "Star Formation in Galaxies Along the Hubble Sequence". In: *Annual Review of Astronomy  Astrophysics* 36, p. 189.

Kennicutt Robert C., J., P. Tamblyn, and C. E. Congdon (1994). "Past and Future Star Formation in Disk Galaxies". In: *Astrophysical Journal* 435, p. 22.

Keto, E. and K. Wood (2006). "Observations on the Formation of Massive Stars by Accretion". In: *Astrophysical Journal* 637.2, p. 850.

Klein, R. I., S. I. Inutsuka, P. Padoan, and K. Tomisaka (2007). "Current Advances in the Methodology and Computational Simulation of the Formation of Low-Mass Stars". In: *Protostars and Planets V*. Ed. by B. Reipurth, D. Jewitt, and K. Keil, p. 99.

Krasnov, V. V., E. E. Lekht, V. M. Minnebaev, M. I. Pashchenko, G. M. Rudnitskii, and A. M. Tolmachev (2018). "Flares of the $H_2O$ Maser Emission in the Young Stellar Object $GH_2O$ 092.67+03.07 (IRAS 21078+5211)". In: *Astronomy Reports* 62.3, p. 200.

Kraus, S., K.-H. Hofmann, K. M. Menten, D. Schertl, G. Weigelt, F. Wyrowski, A. Meilland, K. Perraut, R. Petrov, S. Robbe-Dubois, P. Schilke, and L. Testi (2010). "A Hot Compact Dust Disk around a Massive Young Stellar Object". In: *Nature* 466.7304, p. 339.

Kroupa, P. (2002). "The Initial Mass Function of Stars: Evidence for Uniformity in Variable Systems". In: *Science* 295.5552, p. 82.

Kroupa, P., C. A. Tout, and G. Gilmore (1993). "The Distribution of Low-Mass Stars in the Galactic Disc". In: *MNRAS* 262, p. 545.

Krumholz, M. R., R. I. Klein, C. F. McKee, S. S. R. Offner, and A. J. Cunningham (2009). "The Formation of Massive Star Systems by Accretion". In: *Science* 323.5915, p. 754.

Krumholz, M. R. and C. F. McKee (2005). "A General Theory of Turbulence-regulated Star Formation, from Spirals to Ultraluminous Infrared Galaxies". In: *Astrophysical Journal* 630.1, p. 250.

– (2008). "A Minimum Column Density of $1 g cm^{-2}$ for Massive Star Formation". In: *Nature* 451.7182, p. 1082.

Kuiper, R., H. Klahr, H. Beuther, and T. Henning (2011). "Three-dimensional Simulation of Massive Star Formation in the Disk Accretion Scenario". In: *Astrophysical Journal* 732.1, p. 20.

Kurtz, S., R. Cesaroni, E. Churchwell, P. Hofner, and C. M. Walmsley (2000). "Hot Molecular Cores and the Earliest Phases of High-Mass Star Formation". In: *Protostars and Planets IV*. Ed. by V. Mannings, A. P. Boss, and S. S. Russell, p. 299.

Kurtz, S., E. Churchwell, and D. O. S. Wood (1994). "Ultracompact H II Regions. II. New High-Resolution Radio Images". In: *The Astrophysical Journal Supplement* 91, p. 659.

Lada, C. J. (1987). "Star formation: From OB Associations to Protostars." In: *Star Forming Regions*. Ed. by M. Peimbert and J. Jugaku. Vol. 115, p. 1.

Lada, C. J. and E. A. Lada (2003). "Embedded Clusters in Molecular Clouds". In: *Annual Review of Astronomy  Astrophysics* 41, p. 57.

Ladd, E. F., J. R. Deane, D. B. Sanders, and C. G. Wynn-Williams (1993). "Luminous Radio-quiet Sources in W3(Main)". In: *Astrophysical Journal* 419, p. 186.

Larson, R. B. (1981). "Turbulence and Star Formation in Molecular Clouds." In: *MNRAS* 194, p. 809.

Larson, R. B. (1969). "Numerical Calculations of the Dynamics of Collapsing Proto-star". In: *MNRAS* 145, p. 271.

Lee, C.-F., Z.-Y. Li, P. T. P. Ho, N. Hirano, Q. Zhang, and H. Shang (2017). "Formation and Atmosphere of Complex Organic Molecules of the HH 212 Protostellar Disk". In: *Astrophysical Journal* 843.1, p. 27.

Lozovsky, M., R. Helled, I. Pascucci, C. Dorn, J. Venturini, and R. Feldmann (2021). "Why Do More Massive Stars Host Larger Planets?" In: *Astronomy and Astrophysics* 652, A110.

Luhman, K. L. (2012). "The Formation and Early Evolution of Low-Mass Stars and Brown Dwarfs". In: *Annual review of astronomy and astrophysics* 50.1, p. 65.

Lumsden, S. L., M. G. Hoare, J. S. Urquhart, R. D. Oudmaijer, B. Davies, J. C. Mottram, H. D. B. Cooper, and T. J. T. Moore (2013). "The Red MSX Source Survey: The Massive Young Stellar Population of Our Galaxy". In: *The Astrophysical Journal Supplement* 208.1, p. 11.

Maud, L. T., S. L. Lumsden, T. J. T. Moore, J. C. Mottram, J. S. Urquhart, and A. Cicchini (2015). "A Distance-limited Sample of Massive Star-forming Cores from the RMS". In: *MNRAS* 452.1, p. 637.

McCaughrean, M. J. (2001). "Binarity in the Orion Trapezium Cluster". In: *The Formation of Binary Stars*. Ed. by H. Zinnecker and R. Mathieu. Vol. 200, p. 169.

McKee, C. F. and E. C. Ostriker (2007a). "Theory of Star Formation". In: *Annual Review of Astronomy Astrophysics* 45.1, p. 565.

– (2007b). "Theory of Star Formation". In: *Annual Review of Astronomy Astrophysics* 45.1, p. 565.

McKee, C. F. and J. C. Tan (2002). "Massive Star Formation in 100,000 years from Turbulent and Pressurized Molecular Clouds". In: *Nature* 416.6876, p. 59.

– (2003). "The Formation of Massive Stars from Turbulent Cores". In: *Astrophysical Journal* 585.2, p. 850.

McMullin, J. P., B. Waters, D. Schiebel, W. Young, and K. Golap (2007). "CASA Architecture and Applications". In: *Astronomical Data Analysis Software and Systems XVI*. Ed. by R. A. Shaw, F. Hill, and D. J. Bell. Vol. 376. Astronomical Society of the Pacific Conference Series, p. 127.

Minier, V., M. G. Burton, T. Hill, M. R. Pestalozzi, C. R. Purcell, G. Garay, A. J. Walsh, and S. Longmore (2005). "Star-forming Protoclusters Associated with Methanol Masers". In: *Astronomy and Astrophysics* 429, p. 945.

Mitchell, G. F. and T. I. Hasegawa (1991). "An Extremely High Velocity CO Outflow from NGC 7538 IRS 9". In: *The Astrophysical Journal* 371, p. L33.

Molinari, S., J. Brand, R. Cesaroni, F. Palla, and G. G. C. Palumbo (1998a). "A Search for Precursors of Ultracompact H II regions in a Sample of Luminous IRAS Sources. II. VLA Observations". In: *Astronomy and Astrophysics* 336, p. 339.

Molinari, S., S. Pezzuto, R. Cesaroni, J. Brand, F. Faustini, and L. Testi (2008). "The Evolution of the Spectral Energy Distribution in Massive Young Stellar Objects". In: *Astronomy and Astrophysics* 481.2, p. 345.

Molinari, S., L. Testi, J. Brand, R. Cesaroni, and F. Palla (1998b). "IRAS 23385+6053: A Prototype Massive Class 0 Object". In: *The Astrophysical Journal* 505.1, p. L39.

Molinari, S., L. Testi, L. F. Rodrıguez, and Q. Zhang (2002). "The Formation of Massive Stars. I. High-Resolution Millimeter and Radio Studies of High-Mass Protostellar Candidates". In: *Astrophysical Journal* 570.2, p. 758.

Moscadelli, L., H. Beuther, A. Ahmadi, C. Gieser, F. Massi, R. Cesaroni, Á. Sánchez-Monge, F. Bacciotti, M. T. Beltrán, T. Csengeri, R. Galván-Madrid, T. Henning, P. D. Klaassen, R. Kuiper, S. Leurini, S. N. Longmore, L. T. Maud, T. Möller, A. Palau, T. Peters, R. E. Pudritz, A. Sanna, D. Semenov, J. S. Urquhart, J. M. Winters, and H. Zinnecker (2021). "Multi-scale View of Star Formation in IRAS 21078+5211: From Clump Fragmentation to Disk Wind". In: *Astronomy and Astrophysics* 647, A114.

Moscadelli, L., Á. Sánchez-Monge, C. Goddi, J. J. Li, A. Sanna, R. Cesaroni, M. Pestalozzi, S. Molinari, and M. J. Reid (2016). "Outflow Structure within 1000 AU of High-mass YSOs. I. First Results from a Combined Study of Maser and Radio Continuum Emission". In: *Astronomy and Astrophysics* 585, A71.

Moscadelli, L., A. Sanna, C. Goddi, V. Krishnan, F. Massi, and F. Bacciotti (2019). "Protostellar Outflows at the EarliesT Stages (POETS). III. $H_2O$ Masers Tracing Disk-winds and Jets near Luminous YSOs". In: *Astronomy and Astrophysics* 631, A74.

Motte, F., S. Bontemps, and F. Louvet (2018). "High-Mass Star and Massive Cluster Formation in the Milky Way". In: *Annual Review of Astronomy  Astrophysics* 56, p. 41.

Muench, A., K. Getman, L. Hillenbrand, and T. Preibisch (2008). "Star Formation in the Orion Nebula I: Stellar Content". In: 4. Ed. by B. Reipurth, p. 483.

Navarete, F., A. Damineli, C. L. Barbosa, and R. D. Blum (2015). "A Survey of Extended $H_2$ Emission from Massive YSOs". In: *MNRAS* 450.4, p. 4364.

Obonyo, W. O. (2020). "Non-Thermal Emission from Jets of Massive Protostars". PhD thesis. University of Leeds, UK.

Olguin, F. A., M. G. Hoare, K. G. Johnston, F. Motte, H. R. V. Chen, H. Beuther, J. C. Mottram, A. Ahmadi, C. Gieser, D. Semenov, T. Peters, A. Palau, P. D. Klaassen, R. Kuiper, Á. Sánchez-Monge, and T. Henning (2020). "Multiwavelength Modelling of the Circumstellar Environment of the Massive Protostar AFGL 2591 VLA 3". In: *MNRAS* 498.4, p. 4721.

Osorio, M., S. Lizano, and P. D'Alessio (1999). "Hot Molecular Cores and the Formation of Massive Stars". In: *Astrophysical Journal* 525.2, p. 808.

Padoan, P. and Å. Nordlund (2004). "The "Mysterious" Origin of Brown Dwarfs". In: *Astrophysical Journal* 617.1, p. 559.

– (2002). "The Stellar Initial Mass Function from Turbulent Fragmentation". In: *Astrophysical Journal* 576.2, p. 870.

Palau, A., A. Fuente, J. M. Girart, R. Estalella, P. T. P. Ho, Á. Sánchez-Monge, F. Fontani, G. Busquet, B. Commerçon, P. Hennebelle, J. Boissier, Q. Zhang, R. Cesaroni, and L. A. Zapata (2013). "Early Stages of Cluster Formation: Fragmentation of Massive Dense Cores Down to 1000 AU". In: *Astrophysical Journal* 762.2, p. 120.

Patel, N. A., S. Curiel, T. K. Sridharan, Q. Zhang, T. R. Hunter, P. T. P. Ho, J. M. Torrelles, J. M. Moran, J. F. Gómez, and G. Anglada (2005). "A Disk of Dust and Molecular Gas around a High-mass Protostar". In: *Nature* 437.7055, p. 109.

Pearson, K. (1895). "Note on Regression and Inheritance in the Case of Two Parents". In: *Proceedings of the Royal Society of London Series I* 58, p. 240.

Pearson, T. J. and A. C. S. Readhead (1984). "Image Formation by Self-Calibration in Radio Astronomy". In: *Annual Review of Astronomy  Astrophysics* 22, p. 97.

Pillai, T., J. Kauffmann, F. Wyrowski, J. Hatchell, A. G. Gibb, and M. A. Thompson (2011). "Probing the Initial Conditions of High-mass Star Formation. II. Fragmentation, Stability, and Chemistry towards High-mass Star-forming Regions G29.96-0.02 and G35.20-1.74". In: *Astronomy and Astrophysics* 530, A118.

Pudritz, R. E., R. Ouyed, C. Fendt, and A. Brandenburg (2007). "Disk Winds, Jets, and Outflows: Theoretical and Computational Foundations". In: *Protostars and Planets V*. Ed. by B. Reipurth, D. Jewitt, and K. Keil, p. 277.

Purcell, C. R., M. G. Hoare, W. D. Cotton, S. L. Lumsden, J. S. Urquhart, C. Chandler, E. B. Churchwell, P. Diamond, S. M. Dougherty, R. P. Fender, G. Fuller, S. T. Garrington, T. M. Gledhill, P. F. Goldsmith, L. Hindson, J. M. Jackson, S. E. Kurtz, J. Martı, T. J. T. Moore, L. G. Mundy, T. W. B. Muxlow, R. D. Oudmaijer, J. D. Pandian, J. M. Paredes, D. S. Shepherd, S. Smethurst, R. E. Spencer, M. A. Thompson, G. Umana, and A. A. Zijlstra (2013). "The Coordinated Radio and Infrared Survey for High-mass Star Formation. II. Source Catalog". In: *The Astrophysical Journal Supplement* 205.1, p. 1.

Purser, S. J. D., S. L. Lumsden, M. G. Hoare, and S. Kurtz (2021). "A Galactic Survey of Radio Jets from Massive Protostars". In: *MNRAS* 504.1, p. 338.

Purser, S. J. D., S. L. Lumsden, M. G. Hoare, J. S. Urquhart, N. Cunningham, C. R. Purcell, K. J. Brooks, G. Garay, A. E. Gúzman, and M. A. Voronkov (2016). "A Search for Ionized Jets towards Massive Young Stellar Objects". In: *MNRAS* 460.1, p. 1039.

Purser, S. J. D. (2017). "Ionised Jets Associated With Massive Young Stellar Objects". PhD thesis. University of Leeds, UK.

Ray, T. P., R. Poetzel, J. Solf, and R. Mundt (1990). "Optical Jets from the High-Luminosity Young Stars LkH Alpha and AFGL 4029". In: *The Astrophysical Journal* 357, p. L45.

Reid, M. J., A. L. Argon, C. R. Masson, K. M. Menten, and J. M. Moran (1995). "Synchrotron Emission from the $H_2O$ Maser Source in W3(OH)". In: *Astrophysical Journal* 443, p. 238.

Reipurth, B. and J. Bally (2001). "Herbig-Haro Flows: Probes of Early Stellar Evolution". In: *Annual Review of Astronomy  Astrophysics* 39, p. 403.

Rengarajan, T. N. and P. T. P. Ho (1996). "Search for Optically Thick H II Regions and Ionized Stellar Wind from Luminous Embedded Infrared Sources". In: *Astrophysical Journal* 465, p. 363.

Richer, J. S., D. S. Shepherd, S. Cabrit, R. Bachiller, and E. Churchwell (2000). "Molecular Outflows from Young Stellar Objects". In: *Protostars and Planets IV*. Ed. by V. Mannings, A. P. Boss, and S. S. Russell, p. 867.

Ridge, N. A. and T. J. T. Moore (2001). "A Single Distance Sample of Molecular Outflows from High-mass Young Stellar Objects". In: *Astronomy and Astrophysics* 378, p. 495.

Ridge, N. A., J. Di Francesco, H. Kirk, D. Li, A. A. Goodman, J. F. Alves, H. G. Arce, M. A. Borkin, P. Caselli, J. B. Foster, M. H. Heyer, D. Johnstone, D. A. Kosslyn, M. Lombardi, J. E. Pineda, S. L. Schnee, and M. Tafalla (2006). "The COMPLETE Survey of Star-Forming Regions: Phase I Data". In: *The Astronomical Journal* 131.6, p. 2921.

Rodriguez, L. F., P. T. P. Ho, and J. M. Moran (1980). "Anisotropic Mass Outflow in Cepheus A." In: *The Astrophysical Journal* 240, p. L149.

Roelfsema, P. R., W. M. Goss, and T. L. Wilson (1987). "Carbon Radio Recombination Line Observations of W 3." In: *Astronomy and Astrophysics* 174, p. 232.

Sánchez-Monge, Á., A. Palau, R. Estalella, M. T. Beltrán, and J. M. Girart (2008). "Survey of Intermediate/High Mass Star-forming Regions at Centimeter and Millimeter Wavelengths". In: *Astronomy and Astrophysics* 485.2, p. 497.

Sandell, G., W. M. Goss, and M. Wright (2005). "Protostars and Outflows in the NGC 7538 IRS 9 Cloud Core". In: *Astrophysical Journal* 621.2, p. 839.

Sanna, A., L. Moscadelli, R. Cesaroni, A. Caratti o Garatti, C. Goddi, and C. Carrasco-González (2016). "Momentum-driven Outflow Emission from an O-type YSO. Comparing the Radio Jet with the Molecular Outflow". In: *Astronomy and Astrophysics* 596, p. L2.

Sanna, A., L. Moscadelli, C. Goddi, V. Krishnan, and F. Massi (2018). "Protostellar Outflows at the EarliesT Stages (POETS). I. Radio Thermal Jets at High Resolution Nearby $H_2O$ Maser Sources". In: *Astronomy and Astrophysics* 619, A107.

Scalise E., J., L. F. Rodriguez, and E. Mendoza-Torres (1989). "Water-vapor Maser Emission from Bright, Unassociated IRAS Point Sources." In: *Astronomy and Astrophysics* 221, p. 105.

Shchekinov, Y. A. and A. M. Sobolev (2004). "Synchrotron Emission from Circumstellar Disks around Massive Stars". In: *Astronomy and Astrophysics* 418, p. 1045.

Shepherd, D. S. and E. Churchwell (1996). "Bipolar Molecular Outflows in Massive Star Formation Regions". In: *Astrophysical Journal* 472, p. 225.

Shepherd, D. (2005). "Massive star outflows". In: *Massive Star Birth: A Crossroads of Astrophysics*. Ed. by R. Cesaroni, M. Felli, E. Churchwell, and M. Walmsley. Vol. 227, p. 237.

Shu, F. H., F. C. Adams, and S. Lizano (1987). "Star formation in Molecular Clouds: Observation and Theory." In: *Annual Review of Astronomy  Astrophysics* 25, p. 23.

Sicilia-Aguilar, A., J. S. Kim, A. Sobolev, K. Getman, T. Henning, and M. Fang (2013). "The Low-mass Stellar Population in the Young Cluster Tr 37. Disk Evolution, Accretion, and Environment". In: *Astronomy and Astrophysics* 559, A3.

Snell, R. L., R. B. Loren, and R. L. Plambeck (1980). "Observations of CO in L 1551 : Evidence for Stellar Wind Driven Shocks." In: *The Astrophysical Journal* 239, p. L17.

Solomon, P. M., D. B. Sanders, and N. Z. Scoville (1979). "Giant Molecular Clouds in the Galaxy; Distribution, Mass, Size and Age". In: *The Large-Scale Characteristics of the Galaxy.* Ed. by W. B. Burton. Vol. 84, p. 35.

Sridharan, T. K., H. Beuther, M. Saito, F. Wyrowski, and P. Schilke (2005). "High-Mass Starless Cores". In: *The Astrophysical Journal* 634.1, p. L57.

Sridharan, T. K., H. Beuther, P. Schilke, K. M. Menten, and F. Wyrowski (2002). "High-Mass Protostellar Candidates. I. The Sample and Initial Results". In: *Astrophysical Journal* 566.2, p. 931.

Stahler, S. W., F. Palla, and P. T. P. Ho (2000). "The Formation of Massive Stars". In: *Protostars and Planets IV.* Ed. by V. Mannings, A. P. Boss, and S. S. Russell, p. 327.

Stahler, S. W. and F. Palla (2004). *The Formation of Stars.*

Suri, S., H. Beuther, C. Gieser, A. Ahmadi, Á. Sánchez-Monge, J. M. Winters, H. Linz, T. Henning, M. T. Beltrán, F. Bosco, R. Cesaroni, T. Csengeri, S. Feng, M. G. Hoare, K. G. Johnston, P. Klaassen, R. Kuiper, S. Leurini, S. Longmore, S. Lumsden, L. Maud, L. Moscadelli, T. Möller, A. Palau, T. Peters, R. E. Pudritz, S. E. Ragan, D. Semenov, P. Schilke, J. S. Urquhart, F. Wyrowski, and H. Zinnecker (2021). "Disk Fragmentation in High-Mass Star Formation. High-resolution Observations towards AFGL 2591-VLA 3". In: *Astronomy and Astrophysics* 655, A84.

Tan, J. C., M. T. Beltrán, P. Caselli, F. Fontani, A. Fuente, M. R. Krumholz, C. F. McKee, and A. Stolte (2014). "Massive Star Formation". In: *Protostars and Planets VI.* Ed. by H. Beuther, R. S. Klessen, C. P. Dullemond, and T. Henning, p. 149.

Thompson, A. R., J. M. Moran, and J. Swenson George W. (2017). *Interferometry and Synthesis in Radio Astronomy, 3rd Edition.*

Tieftrunk, A. R., R. A. Gaume, M. J. Claussen, T. L. Wilson, and K. J. Johnston (1997). "The H II/molecular Cloud Complex W3 Revisited: Imaging the Radio Continuum Sources using Multi-Configuration, Multi-frequency Observations with the VLA." In: *Astronomy and Astrophysics* 318, p. 931.

Tomisaka, K. (2002). "Collapse of Rotating Magnetized Molecular Cloud Cores and Mass Outflows". In: *Astrophysical Journal* 575.1, p. 306.

Torrelles, J. M., J. F. Gomez, L. F. Rodriguez, S. Curiel, P. T. P. Ho, and G. Garay (1996). "The Thermal Radio Jet of Cepheus A HW2 and the Water Maser Distribution at 0 -8pt. Scale (60 AU)". In: *The Astrophysical Journal* 457, p. L107.

Trinidad, M. A., S. Curiel, J. Cantó, P. D'Alessio, L. F. Rodrıguez, J. M. Torrelles, J. F. Gómez, N. Patel, and P. T. P. Ho (2003). "Observations of Water Masers and Radio Continuum Emission in AFGL 2591". In: *Astrophysical Journal* 589.1, p. 386.

Turner, J. L. and W. J. Welch (1984). "Discovery of a Young Stellar Object near the Water Masers in W3 (OH)." In: *The Astrophysical Journal* 287, p. L81.

Urquhart, J. S., A. L. Busfield, M. Hoare, S. Lumsden, A. Clarke, T. Moore, J. Mottram, and R. D. Oudmaijer (2007). "The RMS Survey: Radio Observations of Candidate Massive YSOs in the Southern Hemisphere". In: 237. Ed. by B. G. Elmegreen and J. Palous, p. 482.

Urquhart, J. S., M. G. Hoare, C. R. Purcell, S. L. Lumsden, R. D. Oudmaijer, T. J. T. Moore, A. L. Busfield, J. C. Mottram, and B. Davies (2009). "The RMS Survey. 6 cm Continuum VLA Observations Towards Candidate Massive YSOs in the Northern Hemisphere". In: *Astronomy and Astrophysics* 501.2, p. 539.

Van der Tak, F. F. S. (2004). "Hot Molecular Cores and High Mass Star Formation". In: *Star Formation at High Angular Resolution*. Ed. by M. G. Burton, R. Jayawardhana, and T. L. Bourke. Vol. 221, p. 59.

Velusamy, T., W. D. Langer, and K. A. Marsh (2007). "Highly Collimated Jets and Wide-Angle Outflows in HH 46/47: New Evidence from Spitzer Infrared Images". In: *The Astrophysical Journal* 668.2, p. L159.

Walawender, J., G. Wolf-Chase, M. Smutko, J. OLinger-Luscusk, and G. Moriarty-Schieven (2016). "Protostellar Outflows in L1340". In: *Astrophysical Journal* 832.2, p. 184.

Walsh, A. J., M. G. Burton, A. R. Hyland, and G. Robinson (1999). "VizieR Online Data Catalog: Ultracompact H II Regions Studies. II. (Walsh+, 1998)". In: *VizieR Online Data Catalog*, p. 640.

Walter, F. M., J. M. Alcala, R. Neuhauser, M. Sterzik, and S. J. Wolk (2000). "The Low-Mass Stellar Population of the Orion OB1 Association, and Implications for the Formation of Low-Mass Stars". In: ed. by V. Mannings, A. P. Boss, and S. S. Russell, p. 273.

Ward-Thompson, D., D. Nutter, S. Bontemps, A. Whitworth, and R. Attwood (2006). "SCUBA Observations of the Horsehead Nebula - What Did the Horse Swallow?" In: *MNRAS* 369.3, p. 1201.

Werner, M. W., E. E. Becklin, I. Gatley, G. Neugebauer, K. Sellgren, J. Thronson H. A., D. A. Harper, R. Loewenstein, and S. H. Moseley (1980). "High Angular Resolution Far-infrared Observations of the W3 Region". In: *Astrophysical Journal* 242, p. 601.

Wilking, B. A. (1989). "The Formation of Low-Mass Stars". In: *PASP* 101, p. 229.

Wilner, D. J., M. J. Reid, and K. M. Menten (1999). "The Synchrotron Jet from the $H_2O$ Maser Source in W3(OH)". In: *Astrophysical Journal* 513.2, p. 775.

Wolfire, M. G. and J. P. Cassinelli (1987). "Conditions for the Formation of Massive Stars". In: *Astrophysical Journal* 319, p. 850.

Wouterloot, J. G. A. and C. M. Walmsley (1986). "$H_2O$ Masers Associated with IRAS Sources in Regions of Star Formation." In: *Astronomy and Astrophysics* 168, p. 237.

Wynn-Williams, C. G., E. E. Becklin, and G. Neugebauer (1972). "Infra-red Sources in the H II Region W3." In: *MNRAS* 160, p. 1.

Wyrowski, F., P. Schilke, C. M. Walmsley, and K. M. Menten (1999). "Hot Gas and Dust in a Protostellar Cluster near W3(OH)". In: *The Astrophysical Journal* 514.1, p. L43.

Yorke, H. W. and C. Sonnhalter (2002). "On the Formation of Massive Stars". In: *Astrophysical Journal* 569.2, p. 846.

Zapata, L. A., C. Rodrıguez-Garza, L. F. Rodrıguez, J. M. Girart, and H.-R. Chen (2011). "Disks and Outflows in the Massive Protobinary System W3(OH)TW". In: *The Astrophysical Journal* 740.1, p. L19.

Zhang, Q., T. R. Hunter, J. Brand, T. K. Sridharan, R. Cesaroni, S. Molinari, J. Wang, and M. Kramer (2005). "Search for CO Outflows toward a Sample of 69 High-Mass Protostellar Candidates. II. Outflow Properties". In: *Astrophysical Journal* 625.2, p. 864.

Zhang, Q., T. R. Hunter, J. Brand, T. K. Sridharan, S. Molinari, M. A. Kramer, and R. Cesaroni (2001). "Search for CO Outflows toward a Sample of 69 High-Mass Protostellar Candidates: Frequency of Occurrence". In: *The Astrophysical Journal* 552.2, p. L167.

Zinnecker, H. and H. W. Yorke (2007). "Toward Understanding Massive Star Formation". In: *Annual Review of Astronomy  Astrophysics* 45.1, p. 481.

Zuckerman, B. and K. Y. Lo (1987). "$H_2O$ Maser Emission from Stars in the IRAS Point-source Catalog." In: *Astronomy and Astrophysics* 173, p. 263.

# Appendix A

# Target observables

## A.1 18A-104 target distances and luminosities

Table A.1 showing the distances to the target sources, positions and luminosity values.

| Sample name | RA (J2000) | Dec (J2000) | Distance (kpc) | Luminosity ($10^4 L_\odot$) |
|---|---|---|---|---|
| G133.6945+01.2* | 02:25:31.0 | +62.06.20.9 | 2.0 | 4.5 |
| W3 ($H_2O$) | 02:27:04.60 | +61:52:24.73 | 2.0 | 8.3 |
| G138.2957+01.555 | 03:01:31.32 | +60:29:13.20 | 2.9 | 1.4 |
| G139.9091+00.197 | 03:07:24.52 | +58:30:48.30 | 3.2 | 1.1 |
| S87 IRS1 | 19:46:20.14 | +24:35:29.00 | 2.2 | 2.5 |
| G075.7822+00.3* | 20:21:44.1 | +37.26.39.6 | 3.8 | 11.0 |
| S106 | 20:27:26.77 | +37:22:47.70 | 1.3 | 3.4 |
| G078.8867+00.7* | 20:29:24.9 | +40.11.19.4 | 3.3 | 20.0 |
| G084.9505-00.691 | 20:55:32.47 | +44:06:10.10 | 5.5 | 1.3 |
| IRAS 21078+5211* | 21:09:25.2 | +52.23.43.7 | 1.5 | 1.3 |
| G094.6028-01.797 | 21:39:58.25 | +50:14:20.90 | 4.0 | 2.8 |
| G100.3779-03.578 | 22:16:10.35 | +52:21:34.70 | 3.5 | 1.5 |
| G109.8715+02.1* | 22:56:18.0 | +62.01.49.7 | 0.7 | 1.5 |
| G108.7575-00.986 | 22:58:47.25 | +58:45:01.60 | 4.3 | 1.4 |
| IRAS 23033+5951 | 23:05:25.00 | +60:08:15.49 | 4.3 | 1.7 |
| NGC 7538S* | 23:13:44.86 | +61:26:48.10 | 2.7 | 1.5 |
| NGC 7538IRS1* | 23:13:45.36 | +61:28:10.55 | 2.7 | 21.0 |
| NGC 7538IRS9* | 23:14:01.68 | +61:27:19.10 | 2.7 | 2.3 |
| IRAS 23151+5912 | 23:17:21.01 | +59:28:47.49 | 3.3 | 2.4 |
| IRAS 23385+6053* | 23:40:54.5 | +61.10.27.9 | 4.9 | 1.6 |

Table A.1 | **CORE targets distance and luminosities.** Distances to the target sources and corresponding luminosities. '*' indicate our target sources and those targets imaged from Purser et al. (2021). Positions, distances and luminosity values were taken from Beuther et al. (2018).

## A.2 Computed radio luminosities

Table A.2 showing the computed radio distance luminosities and luminosity-to-mass ratio of the CORE targets.

| Target name | Radio luminosity (mJy kpc$^2$) | L/M $L_\odot$ |
|---|---|---|
| G133.6945+01.2 | - | - |
| W3 ($H_2O$) | 0.12 | 8300 |
| G138.2957+01.555 | 1.09 | 1206.90 |
| G139.9091+00.197 | 6.14 | 4583.33 |
| S87 IRS1 | 90.36 | 83333.33 |
| G075.7822+00.3 | 11.12 | 8527.13 |
| S106 | 8.11 | 34000.00 |
| G078.8867+00.7 | 4.36 | 9345.79 |
| G084.9505-00.691 | 4.84 | 1444.44 |
| IRAS 21078+5211 | 0.72 | 5909.09 |
| G094.6028-01.797 | 5.12 | 758.81 |
| G100.3779-03.578 | 1.10 | 6818.18 |
| G109.8715+02.1 | 1.86 | 5769.23 |
| G108.7575-00.986 | 2.22 | 1296.30 |
| IRAS 23033+5951 | 17.56 | 557.38 |
| NGC 7538S | 18.15 | 3333.33 |
| NGC 7538IRS1 | 408.24 | 4883.72 |
| NGC 7538IRS9 | 3.06 | 8243.73 |
| IRAS 23151+5912 | 1.74 | 7228.92 |
| IRAS 23385+6053 | 4.56 | 730.59 |

Table A.2 | **Calculated radio luminosity and L/M ratio values.** Here, we present the computed radio luminosity values using measured or estimated integrated flux (Table 3.13) together with Equation 3.1 and distance values shown in Table A.1. **Notes**: One (G133.6945+01.2) out of the twenty CORE targets does not have any previously measured or estimated integrated flux and associated core mass hence its radio luminosity and luminosity-to-mass ratio (L/M) could not be computed. Both parental core masses (masses associated with the cores of the detected YSOs) and luminosity are obtained from Beuther et al. (2018).

## A.3 Target classification and count

Table A.3 showing the various classifications and count of the CORE targets.

| Classification | Count |
|---|---|
| Jet | 3 |
| Jet with lobe | 1 |
| Jet candidate | 6 |
| HII region | 2 |
| HII region/YSO | 2 |
| RPS | 6 |

Table A.3 | **CORE targets classifications.** A summary of the classification and the related number of objects within the CORE sample. NB: RPS here means radio point source. References: Purser et al. (2021) and the RMS survey; Lumsden et al. (2013).